The Fabrication of Deep-Etched Distributed Bragg Reflectors in AlGaInP/GaAs Laser Structures

Gareth T. Edwards

PhD Thesis

School of Physics and Astronomy
Cardiff University

2007

ProQuest LLC
789 East Eisenhower Parkway
P.O. Box 1346
Ann Arbor, MI 48106-1346

Abstract

This thesis describes work undertaken to understand the physics of dry-etching AlGaInP/GaAs laser structures in Cl-based plasmas to develop a process that allows the fabrication of high-aspect-ratio, sub-micron features. The effects of the main process parameters on the etch rate, selectivity and post-etch surface roughness were studied to understand how the interactions between the semiconductor materials and the plasma gives rise to different sidewall geometries.

The behaviour of the two types of material in the presence of a Cl-based plasma was found to be very different due to the production of $InCl_3$ when etching the AlGaInP layers which is absent when etching GaAs. This product is involatile and rate limiting in Cl-rich plasmas. Effective removal of the inhibiting $InCl_3$ was shown to be necessary to selectively etch the AlGaInP layers anisotropically at a reasonably high etching rate. A narrow range of plasma conditions satisfied these requirements. These conditions provided the thermal- and ion-assisted desorption of the $InCl_3$ such that the removal rate matches the formation rate. In contrast, GaAs was shown to etch anisotropically under a much wider range of conditions as the mechanism for anisotropic etching does not require an inhibitor.

With an optimized set of etch parameters, etching of high-aspect-ratio, sub-micron features in AlGaInP/GaAs laser structures was demonstrated. Despite the difference in etch mechanisms of GaAs and AlGaInP and the use of a 2-step process, at the same Ar fraction vertical sidewall features were achieved in both materials when etching sub-micron gratings. Under conditions that provide smooth vertical sidewalls the etch rate was shown to be aspect-ratio dependent due to the depletion of neutral species at the base of the feature. A range of 1-D gratings were etched with lattice constants as short as 200 nm and aspect ratios as high as 20:1. To the best of my knowledge these are the deepest vertically etched structures on this scale in AlGaInP/GaAs.

Using this process, a range of devices including laser cavities defined by dry-etched facets and Distributed Bragg Reflectors and an integrated emitter/detector device were fabricated to demonstrate the quality of the etch process.

Acknowledgement

Firstly I must thank Peter Smowton and Dave Westwood. Without their input, guidance and support this thesis simply would not exist. I would also like to thank Peter Blood and everyone who has been part of the optoelectronics group for the duration of my project for many interesting and insightful discussions and a thoroughly rewarding experience.

Much of the work presented here was done with the help and assistance of a few people who deserve mentioning. As the work was mostly fabrication and was therefore carried out in the cleanroom I was often grateful for the help given to me by (among others) Angela Sobiesierski, Chris Dunscombe, John Thomson, Karen Barnett, Hugh Lang and Ian Robinson. I'd also like to thank Huw Summers, Dan Matthews and Deepal Naidu for sharing my frustrations with the Raith50 lithography system and Paul Fry of Sheffield University for kindly agreeing to allow me access to their system in times of need. Outside of the cleanroom I'd like to thank Adrian George, Stella Elliot and Ian Sandall for useful discussions about characterisation and instruction on the use of some of the experimental apparatus. I'd also like Henje Simmonds for assistance taking AFM scans and Glyn Summers and Rob Tucker for technical support.

Thanks to everyone I've shared an office with over the years and especially to Lois, Helen, Dave, Dan etc. for the fun social aspect to the PhD...

Finally, I'd like to thank my parents and all my friends and family - particularly Natalie who has lived with this project - who have taken an interest in my work and endured me talking endlessly about it.

Relevant Publications

Selective etching of AlGaInP laser structures in a BCl_3/Cl_2 inductively coupled plasma, G. T. Edwards, D. I. Westwood and P. M. Smowton, Semiconductor Science and Technology, 21(4), pp.513-519, (2006).

Fabrication of high-aspect-ratio, sub-micron gratings in AlGaInP/GaAs laser structures using a $BCl_3/Cl_2/Ar$ inductively coupled plasma, G. T. Edwards, A Sobiesierski, D. I. Westwood and P. M. Smowton, Semiconductor Science and Technology, 22(9), pp.1010-1015 (2007).

Dry Etching of Anisotropic Microstructures for Distributed Bragg Reflectors in AlGaInP/GaAs Laser Structures, G. T. Edwards, P. M. Smowton and D. I. Westwood, IEEE Journal of Selected Topics in Quantum Electronics Vol. 14, No 4, (Jul/Aug 2008).

Contents

1. Introduction

1.1. Aims and motivation

Dry etching techniques are widely used to fabricate semiconductor devices because of the anisotropic nature of the etch mechanisms which allows smaller feature size, due to the potential to fabricate features with vertical sidewalls. This in turn allows integration of devices on a much larger scale than could be achieved using chemical, wet etching.

In optoelectronic materials the ability to etch vertical sidewalls opens up a range of opportunities for device integration. High quality mirrors for laser facets can be etched, light can be guided along ridge waveguides, and even controlled by so-called photonic band-gaps if the device is correctly structured. The advantages of such control for laser devices are numerous. Photonic bandgap structures can allow strong confinement of the optical field and can be used for waveguiding and controlling the emission from the device aperture. Near-perfect reflection can also be obtained for photon energies within the forbidden bandgap allowing the fabrication of very high quality (low mirror loss) laser mirrors which in turn reduces the threshold gain requirement.

Laser structures that contain GaInP quantum well active regions are of interest due to their suitability for operation in the 600-690 nm range of the visible spectrum and in particular their large scale application to optical storage (DVD) devices [1]. While the results of the fabrication studies presented here can often be applied to other material systems of interest (especially InP-based quantum dot structures extending the emission wavelength to ~740 nm for use in photodynamic therapy and biophotonics and, for example, InGaAs/AlGaAs/GaAs for 1.3-1.55 μm emission used in telecommunications) the focus of this project was AlGaInP/GaAs.

The purpose of this work was to investigate the behaviour of the AlGaInP/GaAs material system in the presence of an inductively coupled plasma, to determine the effects of the controllable reactor variables on the plasma and consequently on the etching characteristics of the material and, through this understanding, develop a process capable of fabricating high quality laser devices and test structures. The

ultimate aim of this project was to develop the ability to deep-etch high-aspect-ratio, sub-micron features in AlGaInP to allow fabrication of ridge waveguides, mirrors and photonic structures for any desirable in-plane device architecture.

Semiconductor optoelectronics is also an ideal technology for bio-photonics and semiconductor lasers and photo-diodes have been widely used in bio-sensing and analysis systems. With a suitable dry etching technology, there is the potential for monolithic integration within the optically-active crystal; embedding living systems (cells) within an integrated semiconductor device consisting of light emitters, optical elements and detectors. It is also possible to incorporate micro-fluidic channels to manipulate biological materials [2,3] for applications such as Flow Cytometry and Fluorescence Activated Cell Sorting (FACS) [4,5].

1.2. Thesis structure

This work described in this thesis was carried out in two distinct stages; firstly to develop a process suitable for fabricating devices that contain photonic structures and secondly to design, fabricate and characterise devices. The structure of this thesis reflects this staged approach to the project.

Firstly Chapter 2 provides a brief introduction to laser theory and the basic architecture and properties of photonic bandgap structures are described to set in context how the use of photonic bandgap structures can improve the performance of semiconductor lasers with reference to a Transfer Matrix Method (TMM) model, a simple but useful method of modelling the reflectance spectra of 1-D dielectric stacks. Finally, a brief review of the reported application of such structures for a variety of materials is presented.

Chapter 3 sets out the importance of dry etching for semiconductor device fabrication. The basic principles of plasma generation and the mechanisms of plasma etching are described. Many of the artefacts of plasma etching that make anisotropic etching of high-aspect-ratio, sub-micron features difficult are presented along with some description of the requirements of a suitable etch process. Finally, the operating

principles of inductively coupled plasma (ICP) reactors are described with a discussion of the possible effects of each of the main process variables.

In Chapter 4 the experimental setup used to study the behaviour of the material in the presence of a plasma and ultimately the equipment used to fabricate photonic structures is described.

Chapter 5 contains the bulk of the results presented. Details of the development study undertaken to determine a process that etches selectively and anisotropically suitable for etching sub-micron, high-aspect-ratio features in GaAs and AlGaInP. The chapter culminates with an optimised process for etching distributed Bragg reflectors in AlGaInP/GaAs laser structures.

After development of a suitable etch process attention shifts to the fabrication and characterisation of working laser devices, which serves to further demonstrate the quality of the etch process. Chapter 6 describes this work. Details of the experimental set up used for the standard laser characterisation techniques used are given along with the results of the characterisation.

Finally, a summary of the work is given in Chapter 7 along with some suggestions of future developments and applications of the techniques presented.

2. Photonic microstructures in laser devices

2.1. Introduction

This chapter will describe the basics of laser physics and semiconductor laser design leading to a discussion of how photonic structures may be incorporated into a device to modify or enhance its operation. The design of simple one-dimensional (1-D) photonic structures will be discussed with reference to a transmission matrix model; this thesis is mainly restricted to 1-D photonic structures because in principle they only reflect and transmit light whereas 2-D structures show additional in-plane diffraction which is undesirable for laser reflectors [6]. This chapter only describes background material relevant to subsequent chapters; for further reading consult books such as those by Coldren and Corzine [7], Sands [8], Casey and Panish [9] and Agrawal and Dutta [10].

2.2. Basic laser theory

The laser is an active optical resonator that contains a light-amplifying medium with a noise source from spontaneous emission and some form of optical feedback. In the simplest case, the cavity is formed by two mirrors, at least one of which is partially reflecting to allow extraction of laser light. Within the cavity is an active material with which the light field interacts. Photons can be absorbed to promote electrons to higher energy levels as depicted in Figure 2.1(a). Electrons in higher energy states can relax to lower states with the emission of a photon either spontaneously as in Figure 2.1(b) or, as shown in Figure 2.1(c), the emission can be stimulated by interaction with another incident photon.

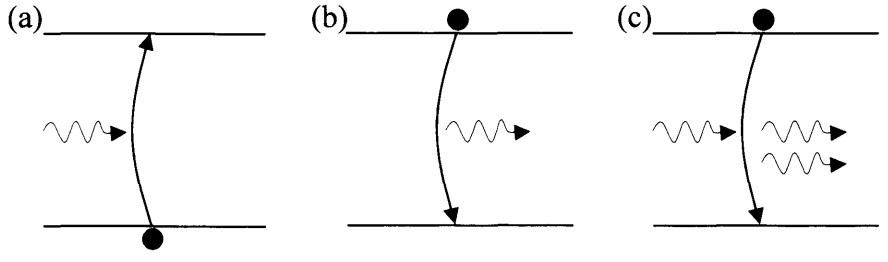

Figure 2.1 – Schematic depiction of (a) photon absorption, (b) spontaneous emission and (c) stimulated emission

Considering the simple 2-level system of Figure 2.1, electrons can be pumped optically or electrically so that the electron population in the higher energy level exceeds that in the lower level. This condition is called population inversion. For material in this state the stimulated emission rate will be greater than the absorption rate producing a net gain of photons in the propagating light field. The gain exhibited by such a material occurs over a specific range of photon energies, the gain spectrum, which is dependent on the band structure of the material, the energy levels of quantum confined states and the degree of pumping.

2.2.1. Resonant cavity modes

The laser cavity will support resonant modes of the optical field where the cavity length, L_c, is an integer multiple of half-wavelengths such that

$$\frac{m\lambda}{2} = nL_c$$

Equation 2.1

where m is an integer and n is the refractive index of the gain material. The modal spacing, shown schematically in Figure 2.2, can be determined by differentiating m with respect to λ to give

$$\Delta\lambda = \frac{\lambda^2}{2nL_c}$$

Equation 2.2

For the laser to emit light it must have a gain spectrum that overlaps at least one of these cavity modes. This is also shown schematically in Figure 2.2. Every mode will have an associated loss from various scattering mechanisms while the active region of the laser may contribute either gain or absorption depending upon the photon energy and degree of pumping.

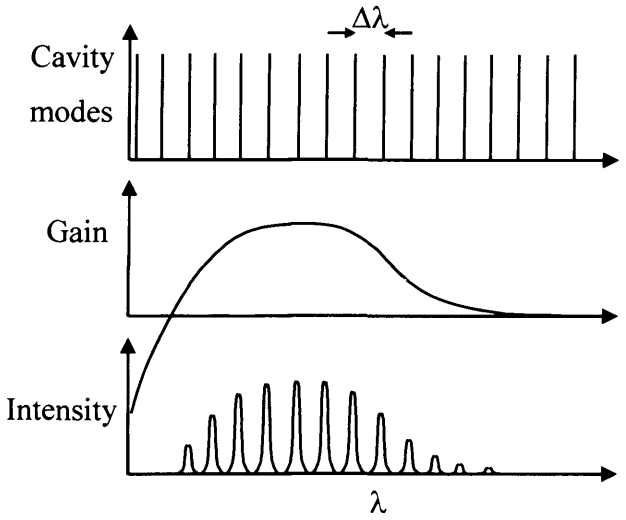

Figure 2.2 – Schematic representation of the mode spacing, gain spectrum and resulting emission spectrum from a laser cavity

2.2.2. Threshold condition

Considering a simple cavity configuration with partially reflecting mirrors with reflectance, *R*, at either end of a cavity of length, L_c, containing a medium with gain, G. Light within the cavity travels back and forth being amplified by the gain medium and as it does so some photons are lost due to internal loss processes, α_i (scattering in the cavity due to imperfections in the waveguide) and through the mirrors, α_m.

Threshold modal gain, Gth, is the amount of gain required to match the cavity losses. At threshold we can consider the case described by Figure 2.3.

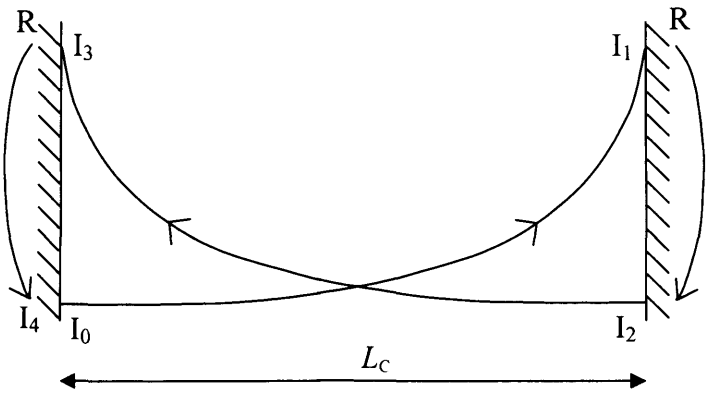

Figure 2.3 – Schematic illustration of light intensity during one round trip in a laser cavity.

The intensity of light travelling in a mode along the cavity is given by

$$I(x) = I_0 \exp[(G - \alpha_i)x]$$

Equation 2.3

From Figure 2.3 we can then determine the intensities at various stages of a single round trip.

$$I_1 = I_0 \exp[(G - \alpha_i)L_C]$$

Equation 2.4

$$I_2 = RI_1$$

$$I_3 = I_2 \exp[(G - \alpha_i)L_C]$$

$$I_4 = RI_3$$

$$\therefore I_4 = R^2 I_0 \exp[2(G - \alpha_i)L_C]$$

At threshold the intensity is constant for each successive round trip such that

$$I_4 = I_0$$

$$\therefore R^2 \exp[2(G_{th} - \alpha_i)L_C] = 1$$

Equation 2.5

or

$$(G - \alpha_i) = \frac{1}{2L_C}\ln(R^{-2}) = \frac{1}{L_C}\ln(R^{-1})$$

Equation 2.6

$$\therefore G_{th} = \alpha_i + \frac{1}{L_C}\ln(R^{-1})$$

Equation 2.7

We know from Equation 2.7 that the mirror loss can be reduced by distributing it over a longer length cavity. It can also be seen that the mirror loss can be reduced by making the mirrors more highly reflecting. This will in turn reduce the gain required to reach the threshold condition provided that the additional loss (absorption) incurred by including the mirrors, which are passive, is not greater.

2.3. Semiconductor lasers

2.3.1. Introduction to semiconductor lasers

Semiconductor lasers have the same fundamental requirements as gas and solid-state lasers, however, there are differences in the way they are pumped and how population inversion is achieved. The principle of operation of a semiconductor laser is very similar to that of a light-emitting diode. A p-n junction provides the active medium where electrons and holes are separated under zero bias (Figure 2.4(a)). When the device is forward biased electrons and holes may recombine at the junction (Figure 2.4(b)).

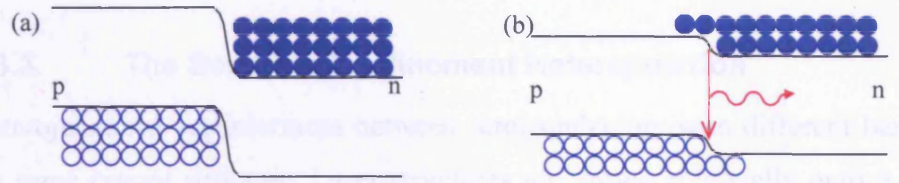

Figure 2.4 – Schematic illustration of a p-n junction (a) under zero bias (b) under forward bias.

In edge-emitting laser diodes optical feedback is most commonly provided by cleaving the wafer along a crystal plane perpendicular to the epitaxial growth. A schematic illustration of typical device geometry is shown in Figure 2.5. This type of semiconductor laser is the focus of this thesis.

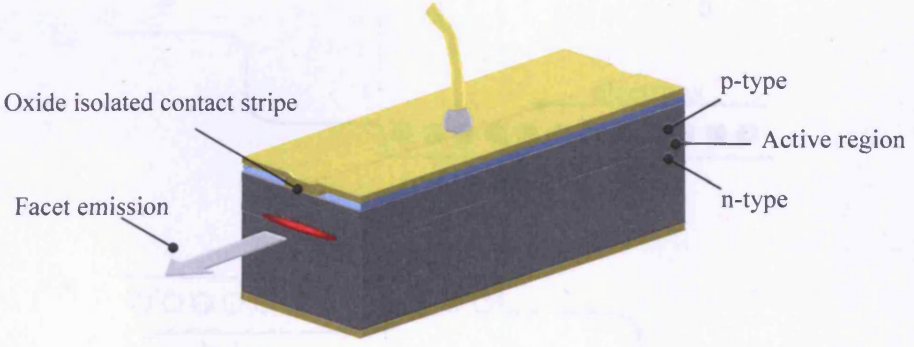

Figure 2.5 – Schematic illustration of an oxide isolated stripe laser.

2.3.2. Threshold current density, J_{th}

An important measure when characterising a laser device is threshold current – the current required to achieve lasing – which is related to the threshold gain. When the modal gain matches the modal loss the threshold carrier density in the active region is reached and the gain pins. At drive currents above threshold all extra carriers injected into the active region will recombine by stimulated emission and contribute to the laser

output. For an ideal device at threshold, the current that flows is the current required to sustain spontaneous emission with no stimulated emission. Therefore the threshold current density for an ideal laser is given by [11]

$$J_{th} = J_{th}^{spon} = eR_{spon} = e\int r_{spon}\left(\varepsilon_{c,v}^{th}, E\right)dE$$

Equation 2.8

Where $\varepsilon_{c,v}^{th}$ are the threshold Fermi levels and the integral is over all energies. R_{spon} is the total spontaneous emission rate and r_{spon} is the spontaneous emission rate at photon energy E.

2.3.3. The Separate Confinement Heterojunction

Heterojunctions are interfaces between semiconductors with different bandgaps within the same crystal structure. Laser structures are grown epitaxially onto a single crystal substrate. A Double Heterojunction (DH) consists of a narrow bandgap layer sandwiched between wider bandgap layers doped to form a p-n junction. The central layer, the active region, is where carrier populations are inverted and optical gain occurs.

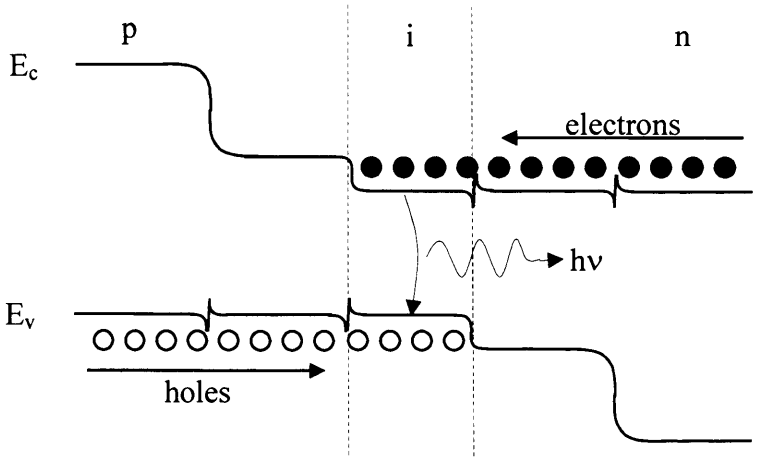

Figure 2.6 – Schematic illustration of the conduction and valence bands of a double heterostructure (DH) under forward bias.

This DH configuration of growth layers has two beneficial features. Firstly, when forward biased, as depicted in Figure 2.6, movement of electrons and holes is restricted by potential barriers such that they are only in the same place within the undoped central region of the device. This reduces the rate of recombination at photon energies

other than desired. Secondly the differences in refractive index (RI) of the various growth layers, which varies with bandgap such that a narrower bandgap material has a higher RI. This is depicted in Figure 2.7. The result is a slab waveguide that helps to confine the optical field to the same location as the active region. This increases the coupling between the light field and the electronic states within the active region. The amount by which the optical mode and the electronic states overlap is called the confinement factor, Γ.

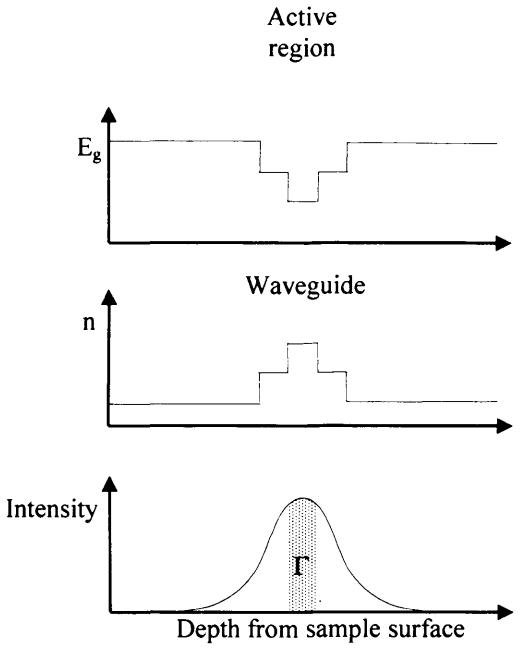

Figure 2.7 – Schematic illustration of the spatial variation of bandgap, refractive index and optical intensity of the separate confinement heterostructure.

A development of the DH laser structure is the separate confinement heterostructure (SCH) which has additional layers (quantum wells, wires or dots) that provide electronic confinement independent from the waveguide and so allow the thicknesses of the active region and the waveguide to be varied independently. A schematic illustration of the energy levels of a SCH under forward bias is shown in Figure 2.8. All devices considered in this thesis are quantum well SCH laser structures. In these devices pumping is achieved by direct electrical injection of carriers across a p-n junction under forward bias. Population inversion occurs when the conduction band electron population exceeds the valence band population.

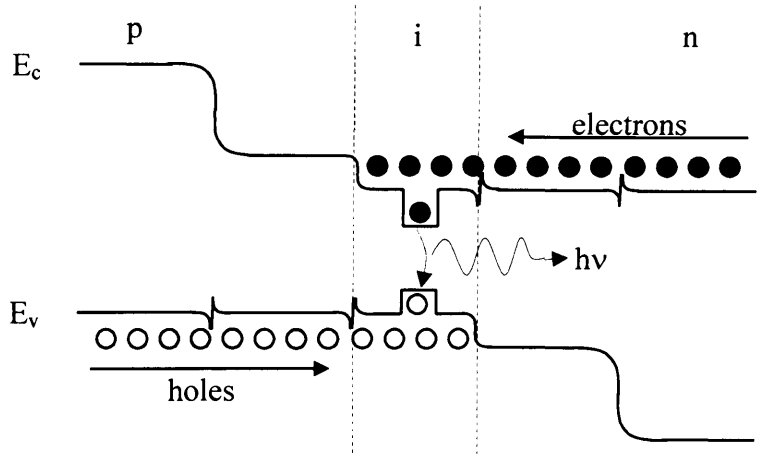

Figure 2.8 – Schematic illustration of the conduction and valence bands of a separate confinement heterostructure (SCH) under forward bias.

Under low bias, emission from the device is dominated by spontaneous emission. When highly forward biased the active region will exhibit gain over a spectral band with a width, peak magnitude and peak wavelength dependent on the quasi-Fermi level separation. The cavity mode closest to the peak wavelength of the gain spectrum where the gain matches the cavity loss will lase. Therefore by controlling the gain spectrum, cavity losses and cavity length it should be possible to engineer the lasing wavelength.

2.4. Controlling light with photonic bandgaps

The use of photonic crystals in active optoelectronic devices has recently seen much research activity. Photonic crystals are periodic structures composed of materials with different dielectric constant where the length scale of the periodicity is of the same order as the wavelength of light. The periodicity gives rise to a photonic band structure analogous to the electronic band structure in semiconductors [12] where photons of frequencies that lie within an incidence angle dependent bandgap can not propagate through the structure. This is caused by destructive interference of waves scattered from the interfaces which results in complete or near-complete reflection of photons of a range of energies. The optical properties of such structures offer attractive means to control optical modes in LEDs and laser diodes [13].

The simplest example of a photonic bandgap structure has a dielectric constant that is periodic in one dimension only. This is more commonly referred to as a Distributed

Bragg Reflector (DBR). This structure will only prohibit light propagation in the direction of periodicity while light propagating in orthogonal directions will propagate freely. If the periodicity is extended to the 2nd and 3rd dimension the bandgap will be extended accordingly, however, this thesis is mainly restricted to one-dimensional photonic structures because in principle they only reflect and transmit light whereas 2-D structures show additional in-plane diffraction which may be undesirable for laser reflectors [6]. Near-perfect reflection can be achieved in one dimension by stacking alternate layers of low-loss dielectric materials that have high and low refractive index. The dimensions of the elements that make up a DBR stack are determined by satisfying the Bragg condition for coherent reflection,

$$2a\cos\theta = mn\lambda$$

Equation 2.9

where a is the thickness (period) of the repeating unit cell, θ is the angle of incidence, n is the refractive index, λ is the wavelength of light and m, an integer, is the order. The simplest solution to satisfy this condition is to have a structure built up from quarter wave elements. The Bragg condition for a quarter-wave stack is satisfied at $\theta = 0°$; these mirrors perfectly reflect light at normal or near-normal incidence creating a stop band of frequencies around λ. Frequencies outside the stop band or waves incident at an angle will be, at least partially, transmitted. The fabrication processes involved in the manufacture of DBRs in vertical cavity surface emitting lasers (VCSELs) allow for layer thicknesses to be deposited with typical accuracies of a few percent [14]. This makes it relatively simple to make each layer of the stack equal to a quarter-wavelength. However, for DBRs incorporated into edge-emitters, or indeed any etched photonic bandgap structure, the control of the feature size is nowhere near as accurate. Therefore, it is often necessary (and perhaps desirable) to simply satisfy the Bragg condition for the whole repeating unit without placing a restriction on the dimensions of each of the constituent elements individually. This then requires that the period of the grating is

$$a = \frac{m\lambda}{2n_{eff}}$$

Equation 2.10

where n_{eff} is the effective refractive index of the unit cell which depends on the coupling with the optical mode, or practically, the depth of the air-gaps.

2.5. Incorporation of photonic structures into lasers

The main benefit that has been exploited by incorporating photonic structures in edge emitting semiconductor lasers stems from the high reflectance of the structures. Laser threshold occurs when the modal gain first matches the cavity losses. To a laser cavity a partially reflecting mirror, while necessary for extracting a useful light beam, is actually a source of loss. Conventional edge emitting semiconductor laser cavities are often fabricated by simply cleaving the device along a crystal plane, resulting in mirrors that reflect roughly 30-40% of the light incident on the facets. If one or both of the mirrors that form the cavity can be made more reflective then this loss can be reduced, leading to a lower threshold gain requirement which in turn allows shorter cavity lengths. Shorter devices obviously allow a greater chip density on the wafer. Parasitic capacitance which scales with surface area is also reduced and the longitudinal mode spacing is increased allowing better mode selectivity. In edge-emitting distributed feedback (DFB) or distributed Bragg reflector (DBR) lasers a Bragg reflector is placed in the optical path to allow lasing from shorter cavities, which in turn can allow some control of the laser wavelength. However, the construction of DFB and most designs of DBR (where the index variation is caused by a corrugation of the region close to the active layers) feedback elements are such that only a small fraction of the propagating mode sees the Bragg action. Consequently, while providing better mode selectivity, the overall mirror reflectivity remains low leading to high distributed mirror losses for short cavity devices. To increase the reflectance of a DBR the grating period can be formed by etching an air gap into the semiconductor material using dry etching techniques. The high step in refractive index between air and semiconductor should allow for high reflectance over a broad wavelength range with a small number (typically 3-5) of periods [15]. If the etched slot is deep enough that it penetrates completely through the active region and lower cladding layer then essentially the entire optical mode sees the Bragg action. Sections 2.7.1 and 2.7.2 discuss the progress made in realising such structures.

2.6. Design of DBRs for laser device mirrors

2.6.1. Calculation of DBR reflectance

For light arriving at the interface between two dielectrics at normal incidence the electric field amplitude reflection and transmission coefficients are given by the Fresnel equations

$$r = \frac{n_1 - n_2}{n_1 + n_2}$$

Equation 2.11

$$t = \frac{2n_2}{n_1 + n_2}$$

Equation 2.12

For the interface between an AlGaInP waveguide core and air this yields a value of the power reflection coefficient, $R \approx 0.3$. (For a complete derivation of the Fresnel equations see, for example, *Optics* by Hecht [16].)

Calculation of the reflectance from a stack of reflecting interfaces that are separated by sub-wavelength distances can be done using the Transfer Matrix Model (TMM) which is a standard technique for solving wave propagation problems [14] that gives calculates the values of the electric and magnetic fields, E and H, at the interface between two dissimilar dielectrics in matrix form. The solution for a multi-layer stack can be determined simply by multiplying the individual matrices. A full derivation of the equations is given in Appendix I. According to the model the amplitude reflection and transmission coefficients are given by

$$t = \frac{2N_S}{m_{11}N_S + m_{12}N_0N_S + m_{21} + m_{12}N_0}$$

Equation 2.13

and

$$r = \frac{m_{11}N_S + m_{12}N_0N_S - m_{21} - m_{22}N_0}{m_{11}N_S + m_{12}N_0N_S + m_{21} + m_{22}N_0}$$

Equation 2.14

respectively.

The intensity reflection coefficients (reflectance) is given by

$$R = |r|^2$$

Equation 2.15

The equations were coded in *Matlab* and used throughout this project to model the reflectance spectra of ideal 1-D photonic structures. When using the model it is important to bear in mind the assumptions that all layers are homogeneous and isotropic and the refractive index varies periodically in the z-direction only with infinite extent in the other dimensions. In practical terms for real device structures it means that etched structures are assumed to be etched completely through the growth layers such that the whole optical mode *sees* the interface. Diffraction and scattering effects are not taken into account.

2.6.2. DBR reflectance calculations

Calculations of the reflectance spectra of any given reflector design were performed using the Transfer Matrix Model. These calculations were then used to model the structures based on the dimensions of the etched structures ascertained by SEM measurements. Although initially it was hoped that the model would be a useful design tool it quickly became clear that its most useful application was in understanding the results of the characterisation experiments. This is because what is drawn in the lithography software is seldom what is patterned on the sample! With adequate assessment of the actual etched features the model is used to calculate the expected reflectance spectrum.

The refractive index of the semiconductor portions of the grating were taken to be 3.25 based on calculations using the Modified Single Effective Oscillator (MSEO) model [17]. The compositional dependence of $(Al_xGa_{1-x})_{0.51}In_{0.49}P$ is plotted in Figure 2.9. Estimates of the effective index of the air portions were calculated by measuring the etch depth and assuming a Gaussian shaped optical mode centered on the active region with a full-width, half-maximum of 0.2 μm. The refractive index as a function of etch depth for a typical laser structure is plotted in Figure 2.10.

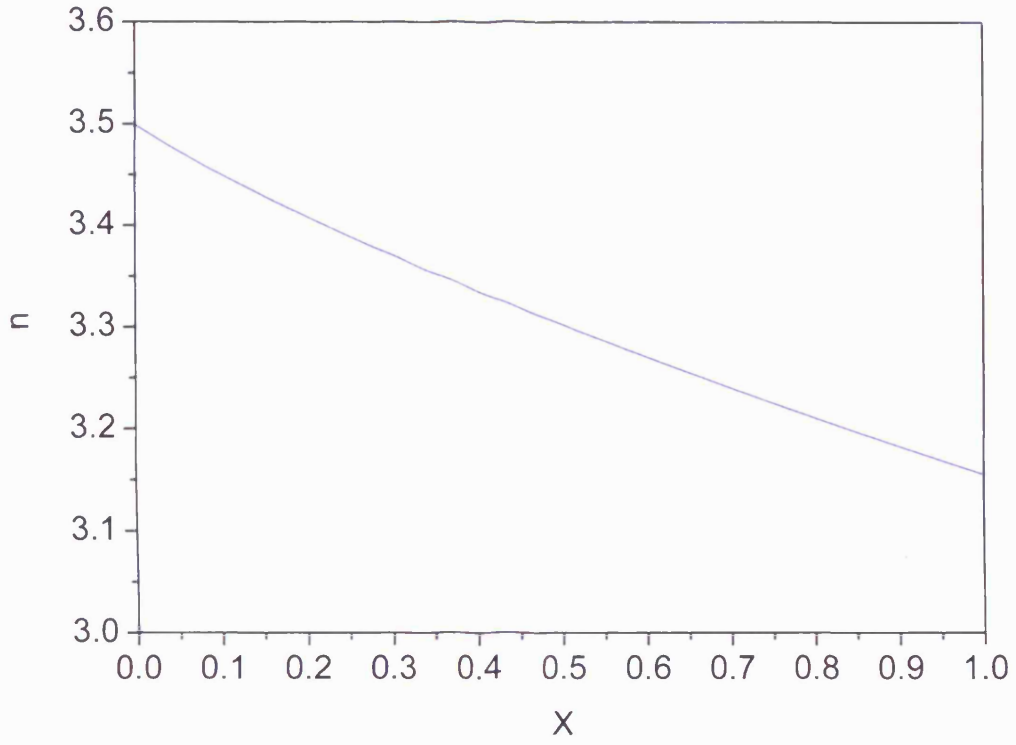

Figure 2.9 – Refractive index as a function of composition of $(Al_xGa_{1-x})_{0.51}In_{0.49}P$

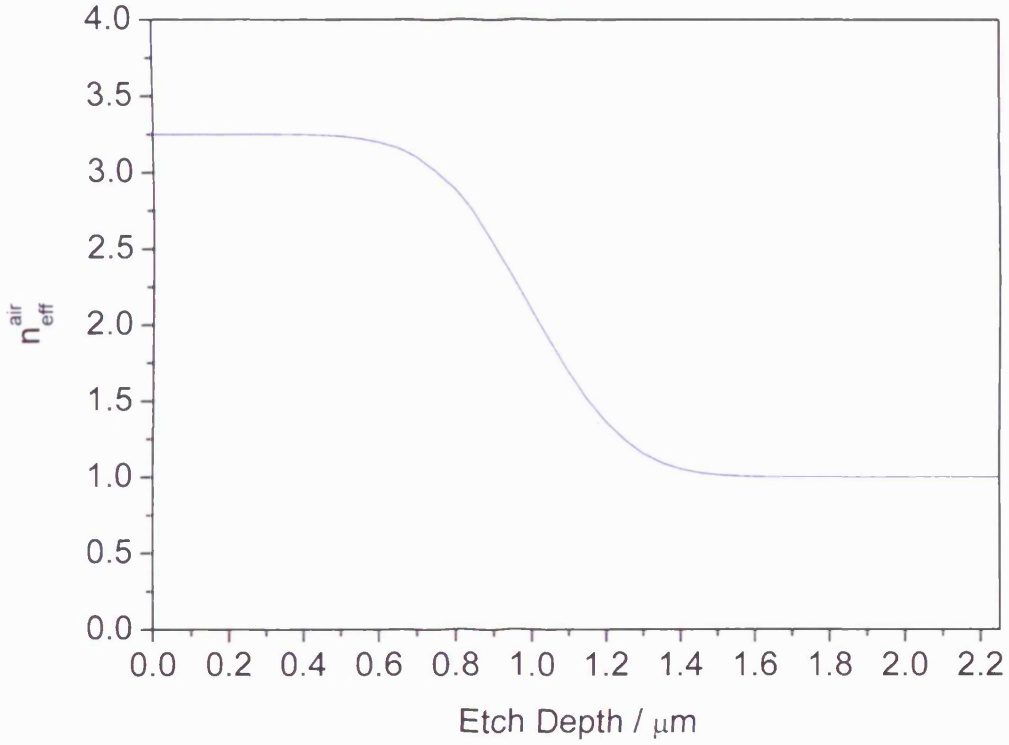

Figure 2.10 – Refractive index for the low index portion of the DBR plotted as a function of etch depth.

Despite the simplicity of the model and the assumptions it is based on, it provides quite instructive information on the effect of the period (order), number of grating periods and effective index (related to the etch depth) on the reflection properties of DBRs.

Figure 2.11 shows reflectance spectra calculated for gratings with a range of periods corresponding to 1st to 7th order gratings, all with 4 periods. We can see that, as expected, the stop band is wider for lower order gratings. For any given order the completeness/width of the stop band increases as the number of periods is increased for low numbers of periods (Figure 2.12). A complete stop band is achieved with 3-4 periods for ideal gratings (n_{air} = 1). For gratings that aren't etched completely through the laser structure such that the air portion has an effective index greater than 1 (Figure 2.13) the number of periods needed to get a complete stop band is higher.

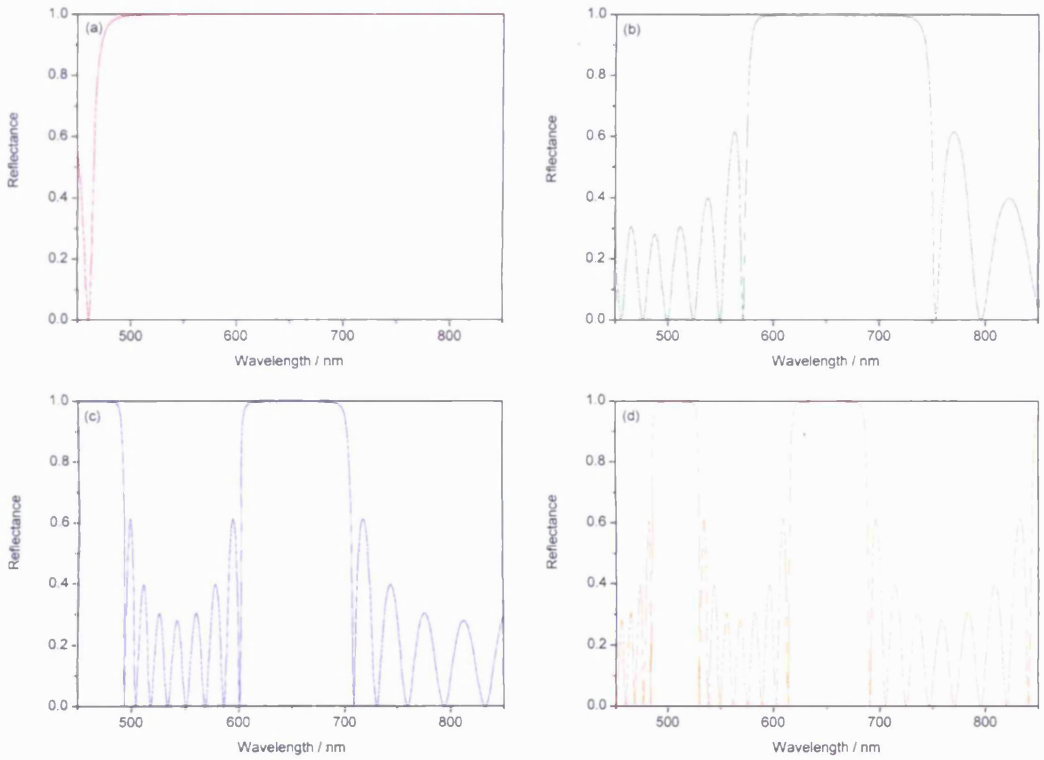

Figure 2.11 – Calculated reflectance spectra for a range of ideal AlGaInP air-semiconductor $^{n\lambda}/_{4}$ DBRs where n = (a) 1 (red line), (b) 3 (green line), (c) 5 (blue line) and (d) 7 (orange line).

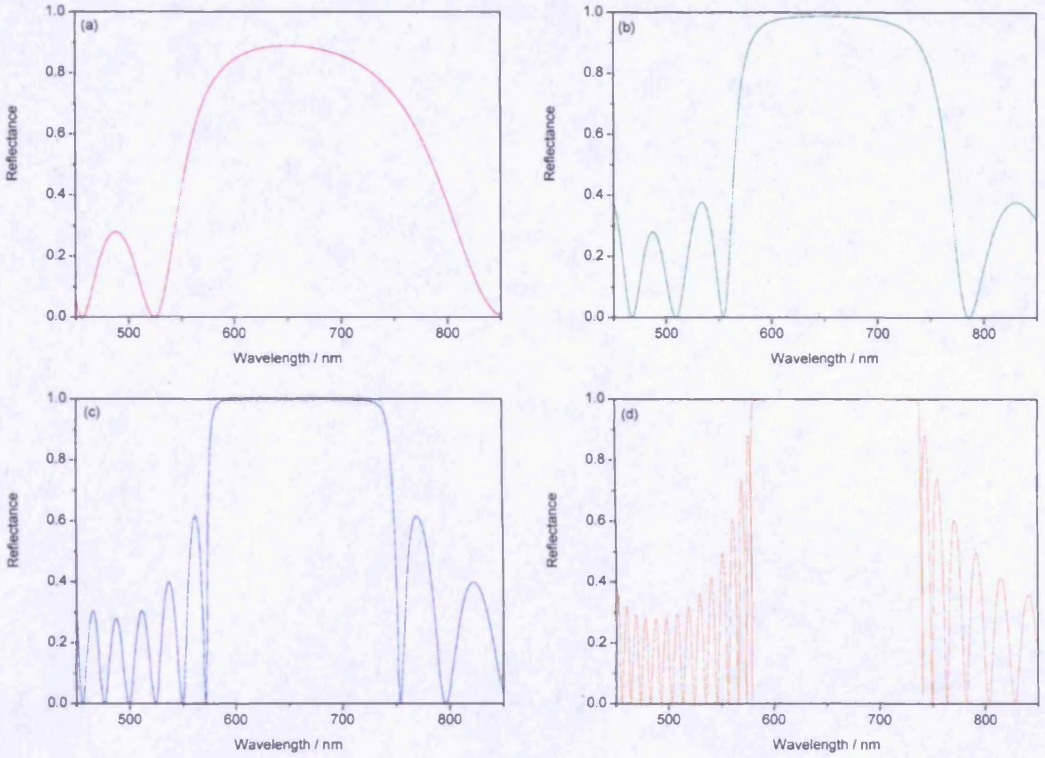

Figure 2.12 - Calculated reflectance spectra for AlGaInP air-semiconductor $^{3\lambda}/_{4}$ DBRs with (a) 1 period (red line), (b) 2 periods (green line), (c) 4 periods (blue line) and (d) 10 periods (orange line).

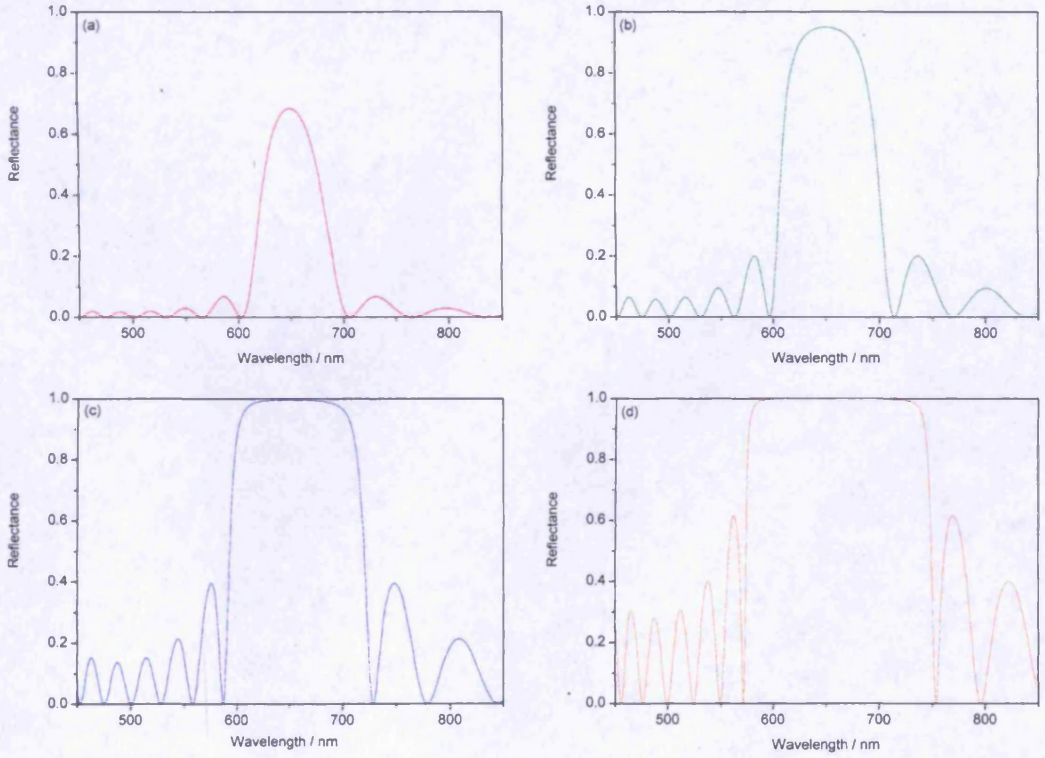

Figure 2.13 - Calculated reflectance spectra for AlGaInP air-semiconductor $^{3\lambda}/_{4}$ DBRs with varying refractive index of the etched slot, n_{eff}^{air} (etch depth) - (a) 2.5 (red line), (b) 2 (green line), (c) 1.5 (blue line) and (d) 1 (orange line).

2.6.3. Effect of the DBR on threshold gain

We know from Equation 2.7 that the mirror loss can be reduced by increasing the mirror reflectance. This will in turn reduce the gain required to reach the threshold condition provided that the additional loss (absorption) incurred by including the passive mirrors is not greater.

Considering only absorption (and not scatter or diffusion losses) in the passive sections the threshold condition can be re-written as

$$G_{th} = \alpha_i + \frac{1}{L_C}\ln\left(R^{-1}\right) + \frac{1}{L_C}A(2Nx)$$

Equation 2.16

Where A is the absorption, N is the number of periods in the grating and x is the thickness of the semiconductor portion of one grating period. The factor 2 takes account of there being a mirror at each end of the cavity. We can therefore calculate the threshold gain as a function of the number of grating periods. This is plotted in Figure 2.14 for a 3rd order DBR device with a typical absorption of 100 cm^{-1} and a cavity length of 300 μm.

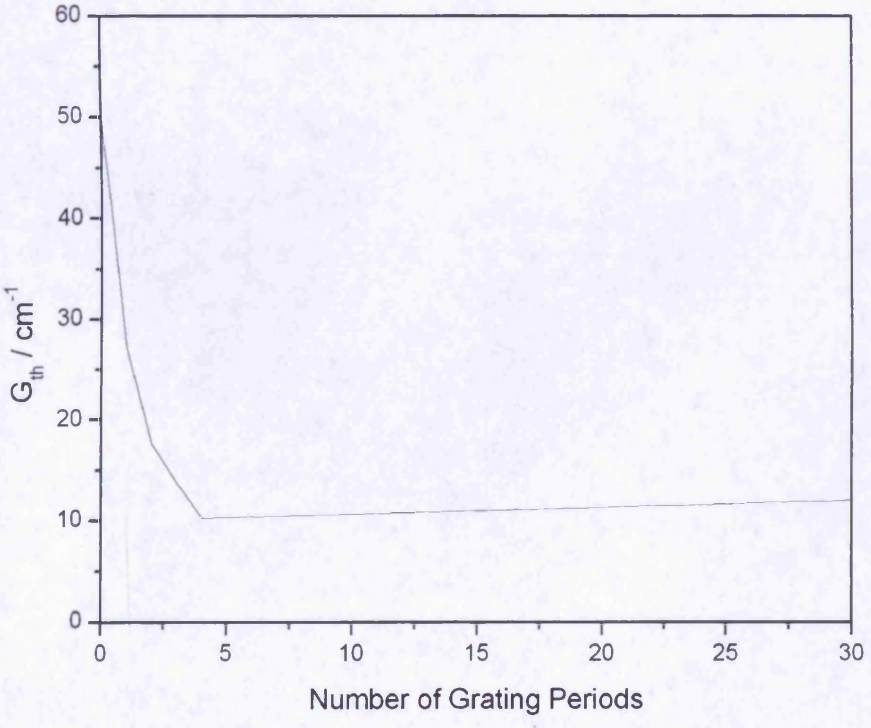

Figure 2.14 – Calculation of threshold gain as a function of the number of periods of a deep-etched 3rd order DBR laser.

As R and A are both spectrally dependent it is possible to calculate a spectral dependence. However, from this simple calculation it is clear that for an (ideal) air-semiconductor grating there should be considerable advantage in having a DBR with up to ~4 periods. Above this we see a small decrease in benefit as the minor increase in mirror reflectance is outweighed by the increased absorption. It should be noted, however, that the detrimental effect of having *too many* periods is minor compared to the effect of having *too few*.

2.7. Applications of DBRs in semiconductor lasers

2.7.1. Long wavelength GaInAs/AlGaAs/GaAs and GaInAsP/InP lasers

Most of the attention regarding research into photonic structures in active optoelectronic devices and indeed in passive waveguides has been focussed on the 1.3 - 1.55 μm infrared region. This is largely due to the importance of such components in telecommunications networks (a similarly large effort has been devoted to other aspects of device physics for devices operating at these wavelengths) and partly due the lower levels of difficulty and more mature technologies for fabricating such devices. The use of deep etched air-semiconductor photonic structures in devices emitting at infrared wavelengths based on InGaAs/AlGaAs/GaAs and GaInAsP/InP/GaAs with deep etched distributed Bragg reflectors (DBR) have been reported by various authors. The first report of such a device was by Baba et al. [18] in 1996 who reported both GaInAs/AlGaAs and GaInAsP/InP devices incorporating 3rd order DBR reflectors to allow lasing with cavity lengths less than 30 μm which could not be achieved with cleaved facets. This was followed closely by a publication by Thomas et al. [19] that also reported fabrication of DBRs in both these materials in the 3rd, 5th and 7th order but provided no device measurements. Yuan et al. subsequently reported a 5th order GaInAs/AlGaAs device with an effective DBR reflectance of 60 % which showed a broadened far-field emission pattern compared to a cleaved device. This was attributed to diffraction and scattering within the DBR [20]. Höfling of the Reithmaier group published several reports of 3rd order devices in the GaInAs/AlGaAs system with cavity lengths as short as 20 μm and DBR reflectance as high as 75 %. The also showed an improvement in threshold current performance up to 2 DBR periods then no further improvement [21,22]. Over the following few years the Krauss group published reports

of 3rd order GaInAs/AlGaAs DBR devices that included descriptions of methods used to determine the reflectance of the etched reflectors at the lasing wavelength. Threshold current was shown to be greatly reuced for devices containing DBR when compared to cleaved devices and short cavity lengths incapable of lasing with cleaved facets were demonstrated to reach threshold [23,24]. Rennon et al. of the Reithmaier group reported the fabrication of a 12 μm long device that used a 1st order DBR [25]. This device exhibited quasi-single mode operation due to the large longitudinal mode spacing (8.2 nm). There have also been reports of 2-dimensional photonic crystals being used as laser mirrors [26,27] and cavity waveguides [28] in these material systems. Generally, the increased reflectance of DBRs has been shown to reduce threshold current and allow much shorter cavity length lasers.

2.7.2. Photonic structures in AlGaInP/GaAs laser devices

Devices based on the AlGaInP/GaAs material system are widely used due to their suitability for operation in the 600-690 nm range of the visible spectrum [1]. However, little progress has been made in processing small feature size, high aspect ratio structures for applications such as photonic bandgap structures in these devices. Devices that utilise photonic behaviour have been mainly restricted to distributed feedback (DFB) lasers [29,30,31,32,33,34] and DBR lasers that use a periodic shallow etched grating embedded close to the active region [35,36,37]. The etched features are typically only <50 nm deep and provide a relatively weak variation in the refractive index seen by the optical field. This means that for there to be a high level of reflection the DBR must extend over many periods. The fabrication technique used also requires a re-growth step to planarise, maintain electrical contact and prevent the light above the DBR from being unguided; this greatly complicates the fabrication. Finally, Chen et al. [38] recently showed a 2-D photonic crystal slab dry-etched into a multiple quantum well structures but the features were still only etched to a depth of ~240 nm.

The lack of reports of devices containing deep-etched photonic crystals is largely due to the challenges posed by the nanometre scale of the features required; a first-order photonic crystal would require a lattice constant of ~200 nm. To etch such features an AlGaInP etch process is needed that is highly selective over the mask and has a very high degree of anisotropy. Lithography limitations dictate that masks are thin (<150nm)

which makes it necessary for an etch process to be highly selective in favour of the semiconductor in order to etch to the required depth of >2μm.

Selective dry-etching of In-containing compounds in Cl_2-based plasmas has proved challenging due to the formation of $InCl_3$, an etch product that is relatively involatile and significantly limits the etch rate [39]. The removal rate of this product and therefore the etch rate of In-containing compounds has been shown to be highly dependent on temperature [39,40] and/or additive gases such as Ar and N_2 [41,42,43,44,45,46]. At temperatures above 150°C there is a significant increase in etch rate due to thermally-assisted desorption of $InCl_3$ and in Reactive Ion Etching (RIE) systems with Cl_2 or BCl_3 chemistries it has been necessary to use sample temperatures >150 °C while etching [47,48]. In RIE and Electron Cyclotron Resonance (ECR) systems significant increases in room temperature etch rate of In-containing materials by the addition of neutral additive gases have also been reported. Thomas et al. reported InP etch rates of up to 3.81 μm min^{-1} at 25 °C using an ECR source by adding neutral Ar to the plasma suggesting that $InCl_3$ can be removed by ion-assisted desorption [41]. Hong et al. reported etch rates above 1 μm min^{-1} when etching GaInP, AlInP and AlGaP in RIE and ECR plasmas using Cl_2 or BCl_3 with Ar or N_2 additives [42,43,44,45] and room temperature etch rates of up to 0.2 μm min^{-1} in a planar ICP reactor with the same materials and chemistries [46].

All reports indicate that there *can be* an enhancement of the etch rate of In-containing semiconductors in Cl-based chemistries, due to ion-assisted desorption, by adding neutral gases to the chemistry either as an alternative or in addition to etching at high temperature. However, they do not discuss how these variables affect the masking material being considered so there is no indication of how selectivity varies with the process variables.

2.8. Summary

Deep etched Distributed Bragg Reflectors have been incorporated into laser diodes in various material systems and have been shown to allow lower threshold currents due to the decreased mirror loss. However, there has been little progress incorporating such structures into AlGaInP/GaAs structures. The fabrication and characterisation of deep-

etched photonic structures in AlGaInP/GaAs laser devices is the focus of this work. The widespread use of the material system combined with the lack of a suitable fabrication process for producing deep-etched in-plane photonic structures means that there is a real need to develop a process for reliably making smooth (compared to the length scale of the light), high-aspect-ratio, nanometre-scale features. The effects of both temperature and the addition of Ar, in addition to a range of other controllable reactor variables, on etch rate and selectivity are investigated to determine a process suitable for fabricating sub-micron, high-aspect-ratio structures.

3. Introduction to plasma etching for fabricating photonic crystals

3.1. Introduction

This chapter will introduce plasma etching and explain why it is used to fabricate high-aspect-ratio features. Basic plasma physics will be introduced by considering the reactive ion etching (RIE) reactor geometry. This will lead to discussion of the main etch mechanisms, the definition of selectivity and its importance and the need for careful mask choice. Problems commonly associated with dry etching that can cause loss of anisotropy will also be explained in the context of the main etch mechanisms. Finally, inductively coupled plasma (ICP) sources will be discussed along with the effects of the main process variables available on typical ICP reactors.

3.2. The need to dry etch photonic crystals

Photonic structures in semiconductor lasers need to have high aspect ratios (~20:1) for feature dimensions of ~100 nm in order to etch well below the active region into the lower cladding layer, typically >2 μm. This is to provide a strong overlap between the optical mode and the periodic structure and to prevent the optical mode being pushed into the lower half of the waveguide (which results in a reduced overlap with the active region – a lower confinement factor) by different effective refractive indices above and below the active region.

In addition to high aspect ratio, it is important that etched features are vertical as they are reflecting surfaces and any deviation from vertical will introduce loss as some of the reflected light is not coupled back into the optical cavity. We define the measure of the verticality of etched film by the degree of anisotropy A_f as

$$A_f = 1 - \left[\frac{R_h}{R_v}\right]$$

Equation 3.1

where R_h and R_v are the horizontal and vertical etch rates respectively.

Wet chemical etching has the advantage that it can be highly selective in which material it etches. However, the disadvantage of purely chemical etching is that it usually has no preferential direction and results in an isotropic etch, as depicted in Figure 3.1a. Therefore for applications that require features to have an anisotropic etch profile (Figure 3.1b), particularly those that also require high aspect ratios, an alternative method of etching must be used.

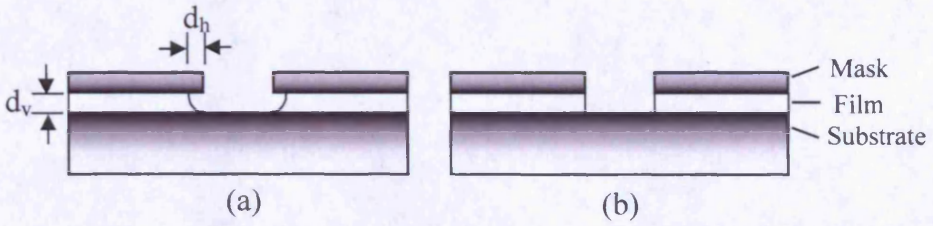

Figure 3.1 – Sidewall profiles of (a) isotropic and (b) anisotropic etching.

3.3. Basic plasma physics

Dry etching techniques that utilise plasmas are now well established for anisotropic etching of semiconductors, metals and dielectrics. In its simplest form, a plasma reactor for this purpose consists of a pair of electrodes that are driven at radio frequency. This is shown schematically in Figure 3.2. A process gas flows into the reactor where it experiences the electric field between the electrodes. A small fraction of the gas is ionised creating a plasma state. For this simple reactor geometry, typically only one per 10^5-10^6 atoms is ionised [49]. The exact composition of the plasma depends on many factors including the process gas, chamber configuration, process parameters, and chamber history. Typically the plasma will consist of a mix of neutral gas, radicals, positive ions, electrons and photons.

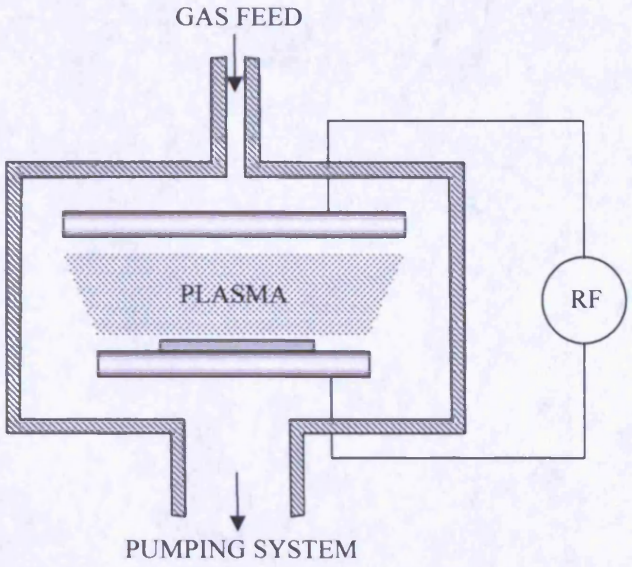

Figure 3.2 – Basic reactor configuration for Reactive Ion Etching (RIE).

3.3.1. Production of species

Inelastic electron-neutral collisions provide the source of ions and radical species which are continuously lost by recombination and reaction processes respectively. The main formation and loss processes are highlighted by considering the simple example of a Cl_2 plasma.

(a) ion and electron formation

$$e + Cl_2 \rightarrow Cl_2^+ + 2e$$

Equation 3.2

(b) atom and radical formation

$$e + Cl_2 \rightarrow e + Cl + Cl$$

Equation 3.3

(c) heat and light generation

$$e + Cl_2 \rightarrow e + Cl_2^*, \text{ and}$$

Equation 3.4

$$Cl_2^* \rightarrow Cl_2 + h\nu$$

Equation 3.5

Or

$$e + Cl \rightarrow e + Cl^*, \text{ and}$$

Equation 3.6

$$Cl^* \rightarrow Cl + h\nu$$

Equation 3.7

where Cl_2^* and Cl^* are excited states of Cl_2 and Cl respectively. For more complicated systems ($BCl_3/Cl_2/Ar$) there is the formation of ions and radicals of the parent molecules as well as the production of ions and radicals from dissociated species (e.g. BCl_2 and BCl). There is also characteristic emission of light from relaxation of the excited states of these species.

3.3.2. Sheath potential

The plasma can not be sustained until the charge density reaches a critical value (typically $10^9 - 10^{10}$ particles cm^{-3}) otherwise rapid diffusion of charge to the chamber walls extinguishes the discharge [50]. Although formally there are equal numbers of positive and negative charge carriers, diffusion of charge to the walls of the chamber and recombination on boundary surfaces depletes charge in this *sheath* region. As electrons are lighter and have more energy they diffuse faster than positive ions resulting in an excess positive charge and a high plasma potential relative to the electrodes. At such charge densities the main body of the plasma has reasonably high conductivity. Consequently large electric fields can not exist without high current flow. As charges near the electrodes are quickly removed, charge density in this region is much lower than in the bulk of the plasma allowing high fields. Therefore most of the potential difference between the plasma and the electrodes is dropped across the sheath.

It is the ions that are responsible for allowing the etched features in a dry etched process to have anisotropic profiles. This is because they are accelerated by the voltage drop across the sheath and strike the sample and so are highly directional. Section 3.4 describes in more detail the mechanisms responsible for etching in plasmas.

3.3.3. Formation of DC bias

As already mentioned, most of the voltage applied to sustain the plasma is dropped across the thin sheath layer formed at the interface with the chamber wall. For parallel plate electrodes of equal area, the time averaged potential distribution between the electrodes is symmetrical. However, when the sustaining field is an RF alternating voltage capacitively coupled via non-symmetric electrodes (as in most RIE systems the surface area of grounded electrode is much larger than that of the driven electrode) an additional DC self-bias is induced [51].

The presence of a blocking capacitor (see Figure 3.3) introduces the constraint that no net current can flow during one RF cycle. Therefore, for the plasma to achieve zero charge flow there must be different sheath potentials at each electrode. Consequently, the driven electrode charges up negatively until enough electrons are repelled for this constraint to be met resulting in a large negative bias, the DC self bias, being developed between the powered electrode and the plasma. This DC bias increases with the ratio of electrode areas and is used to enhance the sheath potential adjacent to, and therefore the ion energy striking, the smaller electrode.

3.3.4. Measurement of plasma potentials

The relationships between the various potentials in a plasma reactor are shown schematically in Figure 3.3. RF and DC voltages are measured between the driven electrode and earth. The DC component of the overall voltage can be separated from the RF component with a choke. The sheath voltage, which is responsible for accelerating ions into the sample surface, is not easily measured. In practice the DC bias is usually used to gauge plasma potential.

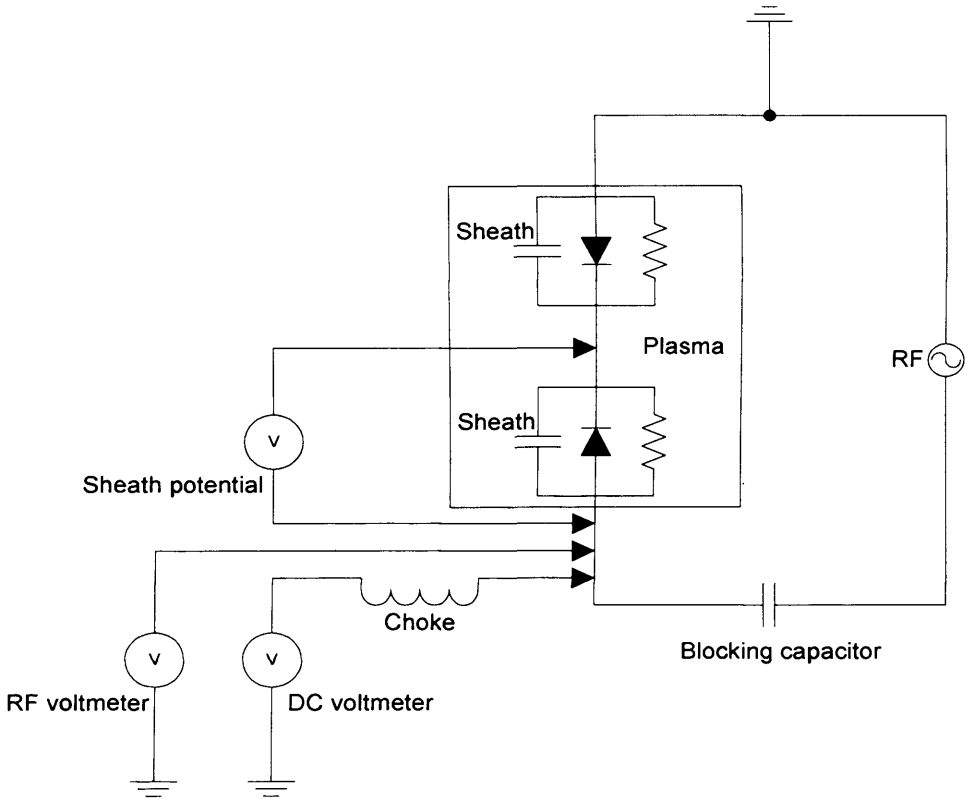

Figure 3.3 – Schematic diagram defining how sheath potential, RF potential and DC bias are measured.

3.4. Mechanisms of plasma etching

We can describe most plasma etch processes by four main categories of removal mechanism shown schematically in Figure 3.4. In any dry etch process a combination of some or all of these mechanisms can be used to describe the overall material removal. By controlling the significance of each mechanism to the overall etch process it should be possible to control the characteristics of resulting etched feature.

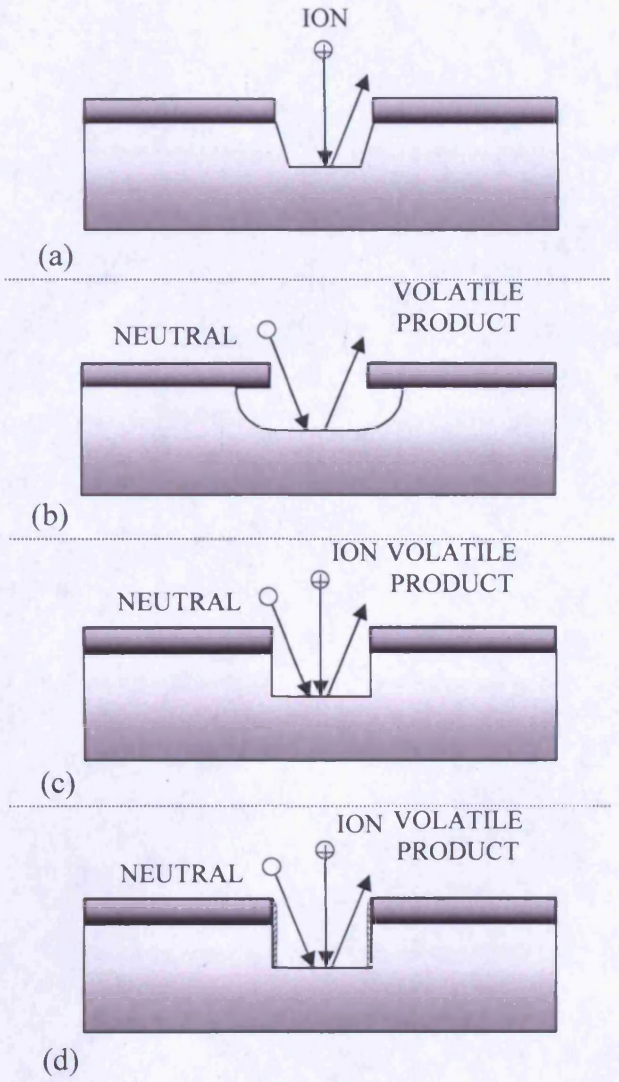

Figure 3.4 – The four main etch mechanisms in a plasma process. (a) Physical sputtering, (b) Pure chemical etching, (c) Ion-assisted chemical etching, (d) Inhibitor driven anisotropic etching.

3.4.1. Sputtering

Sputtering is a purely physical process where positive ions are accelerated across the sheath into the surface of the material being etched. This is depicted in Figure 3.4a. The energy and momentum of the ions is transferred to atoms in the sample that in turn

collide with neighbouring atoms. Most of these atoms are trapped within the sample but some atoms close to the surface can be ejected. When the chamber pressure is low enough, the mean free path is long enough for the sputtered atoms to be completely removed from the sample. If the mean free path is too short collisions with the gas molecules in the plasma will cause some of the ejected material to be re-deposited on the sample surface. This mechanism requires high energies to break inter-atomic bonds. As the ion energy required to remove atoms from any material is much larger than the difference in bond strength between different materials it is the least selective of the four categories. Typically, sputtering rates are low and the damage induced throughout the bulk of the sample by such high energy collisions is significant. Sputtering can also form unwanted features around etched structures (see section 3.7).

3.4.2. Chemical etching

Figure 3.4b shows the effect of chemical etching. Unlike sputtering, chemical etching is not a mechanism that is used in isolation in a plasma process. A purely chemical etch does not require any extra energy from the impact of ions on the sample surface and etching will often occur without the presence of the plasma. This makes chemical etching inherently more selective than physical sputtering as reactions will only occur with materials with which it is chemically favourable. In addition to the reaction it is necessary to form products that have high vapour pressures (volatile) to facilitate removal. Material loss from the surface is then evaporative allowing etching at higher pressures where sputtered material would be re-deposited. Volatility of reaction products is essential in any etch process where there is an element of chemical etching as involatile products will accumulate on the surface. The resulting layer will passivate the surface preventing further reaction. Chemical etching is usually isotropic (however not always) making it unsuitable for etching fine features in thick films due to the large undercut that arises.

3.4.3. Ion-assisted chemical etching

Figure 3.4c shows how ion-assisted chemical etching from neutral gas-solid reactions occur due to the highly directional energetic ions impacting the sample surface to free surface atoms that would otherwise be unable to react. The result can be an etch rate that exceeds the sum of the separate chemical and sputter removal rates. The

microscopic details of the effect impacting ions have on the surface varies for different surface/etchant combinations. The introduction of defects or dislocations into the lattice, the formation of dangling bonds on the surface and partial dissociation of surface atoms are possible causes but the important feature of the mechanism is that the energy and momentum given up to the surface modifies it in a way that renders it more reactive. Since the ions accelerated across the sheath potential strike the surface vertically, ion-assisted etching is highly directional; however, the mechanism can be selective as the removal process is still chemical in origin. Damage is still induced by this process but not to the same extent as a pure sputtering etch process.

3.4.4. Inhibitor driven anisotropic etching

For anisotropic etching, an ideal ion-assisted process would be one where the etch rate without the presence of the ion flux is zero; in practice this is often not the case. Inhibitor driven anisotropy (Figure 3.4d) occurs when the sample surface is covered by a passivating layer that prevents contact between reactive neutrals and vertical sidewalls of features. Horizontal surfaces are allowed to be etched as ion bombardment either prevents the formation of or removes the inhibitor film. This mechanism requires reactive neutral etchant species, an ion flux normally incident to the surface and an inhibitor film forming species. Unlike anisotropy achieved in ion-assisted chemical etching, in this method of anisotropic etching the chemical reactions are spontaneous and ion bombardment serves only to remove the inhibitor film.

3.4.5. Summary of etch mechanisms

When developing a dry etch process it is important to understand the removal mechanisms and how they are related to variations in process parameters. By recognising features characteristic of one etch mechanism, it is possible to adjust the etch conditions to strike the right balance between chemical and physical disruption of the sample surface and in doing so control the profile of the etched feature.

3.5. Limitation of etch rate

To understand the factors that can limit the rate at which material is removed from a surface by chemical reactions with an active gaseous species (albeit ion-assisted) it is

instructive to consider the steps that occur during etching. This is discussed in detail by Coburn et al [52]. The first necessary step is the chemisorption of the gas species on to the surface. For molecular gases this may involve dissociation of the gas molecule. This is illustrated by Equation 3.8 for the simple case of etching Ga in a Cl_2 plasma. Even where chemisorption is non-dissociative the energy present in the plasma will often cause the adsorbed molecule to dissociate. Sample temperature, chamber pressure, ion energy and ion flux all influence the ability of gas species to dissociate and adsorb.

$$Cl_{2(gas)} \rightarrow Cl_{2(ads)} \rightarrow 2Cl_{(ads)}$$

Equation 3.8

The second step is the formation of a volatile reaction product illustrated by Equation 3.9. This formation is usually limited by the unwillingness of material to react in the absence of ion bombardment. Careful choice of gas chemistry is clearly important to enable reactions to occur. Increasing ion energy and flux may also increase the reaction rate.

$$Ga + 3Cl_{(ads)} \rightarrow GaCl_{3(ads)}$$

Equation 3.9

The final step is desorption of the reaction product into the gas phase to be removed by the vacuum system. This is illustrated by Equation 3.10. When the reaction product is involatile and reluctant to desorb the reaction will stop when the product reaches a critical thickness determined by the mobility of the relevant species through the film. This thickness can often be controlled by altering the plasma environment.

$$GaCl_{3(ads)} \rightarrow GaCl_{3(gas)}$$

Equation 3.10

If any of these steps does not occur the surface will not be etched and in any etch process one of these steps will be rate limiting. To increase the etch rate it is therefore important to know which step is rate limiting.

3.6. Etch masks

3.6.1. Selectivity

Selectivity is a measure of relative etching rates. It may be relative to different material layers to be etched to the same pattern, to the material in the layer immediately below that being etched (substrate), or to the mask. For this work the latter definition is the most relevant and will be used from now on. Selectivity is an important measure when designing an etch process, especially for sub-micron features, as it determines the mask thickness requirements.

The resistance of the mask to the effects of the plasma is increasingly important as feature size reduces. If linewidth (the width at the top of the feature) tolerances are low, the minimum required mask thickness is simply the thickness of the film to be etched divided by the selectivity. The minimum selectivity should take into account non-uniformities in etch rate (a result of non-uniform plasma conditions), film thickness and mask thickness as these may all add to the selectivity required.

3.6.2. Minimum selectivity requirement

The following is based on an analysis of minimum selectivity requirement by Mogab [53]. Considering the situation depicted in Figure 3.5 where a film of thickness d_f is etched through in a time t given by

$$t_{tot} = \frac{d_f}{R_f} \times U$$

Equation 3.11

where R_f is the etch rate of the film and U is a uniformity factor and $U \geq 1$ to take into account non-uniformities in etch rate and film thickness across the sample. Further consideration of the uniformity factor is unnecessary for this discussion.

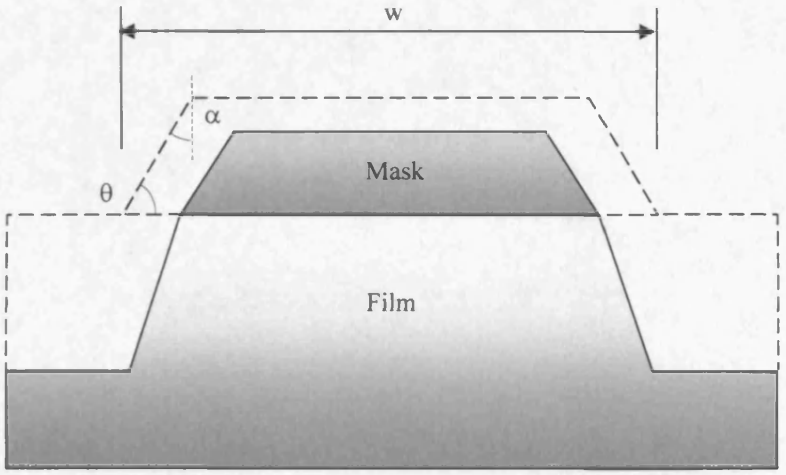

Figure 3.5 – Schematic illustration of the effect of an angled mask edge. The mask edge, exposed to the etching effects of the plasma, has a horizontal component to its etch rate.

There are always vertical and horizontal mask etching components regardless of mask geometry and dependent on plasma conditions. However, where a patterned mask is angled as in Figure 3.5, such that the sidewall of the mask is exposed to vertically moving ions the plasma, there is an additional horizontal component to the etching of the mask material. The width of the mask, w, will therefore reduce over the course of the etch by

$$\Delta = 2t_{tot}\left(R_h + R_v \tan\alpha\right) = 2t_{tot}\left(R_h + R_v \cot\theta\right)$$

Equation 3.12

where R_h and R_v are the horizontal and vertical etch rates of vertical sidewalls respectively. This can be written as

$$\Delta = 2d_f \frac{R_v}{R_f} U\left[\cot\theta + \frac{R_h}{R_v}\right]$$

Equation 3.13

The ratio of R_f to R_v is the selectivity. Therefore by rearranging we get

$$S_m^f = \frac{2d_f}{\Delta} U\left[\cot\theta + \frac{R_h}{R_v}\right]$$

Equation 3.14

Equation 3.13 shows that even for a process that provides anisotropic etching of the film, there is a loss in linewidth resulting from horizontal mask erosion. To reduce this linewidth loss, and for minimum selectivity requirements according to Equation 3.14,

the mask angle must be close to 90° and the horizontal component of the mask etch rate must be minimised.

The selectivity is defined as the factor thicker than the film the mask must be, therefore we can rewrite this equation in the form:

$$S_m^f d_m = \frac{2d_f U}{\Delta}\left[\cot\theta + \frac{R_h}{R_v}\right]$$

Equation 3.15

$$\therefore d_m = \frac{2d_f}{S_m^f \Delta} U\left[\cot\theta + \frac{R_h}{R_v}\right]$$

Equation 3.16

Equation 3.16 indicates that for anisotropic etching the mask thickness should be twice that required by the simple ratio of etch rates. In the case where there is no inherent mask angle and the $R_h=0$, this equation reduces to

$$d_m = \frac{2d_f U}{S_m^f}$$

Equation 3.17

3.6.3. Mask properties

From the criteria for minimum selectivity we can infer the properties desirable in a mask material. Obviously, the lower the vertical etch rate of the mask material is the higher the selectivity will be allowing a thinner mask. It is important that the mask is very highly resistant to chemical etching (and for that matter ion-assisted chemical etching) in the process gases being used as this will cause horizontal etching of the mask. Finally, it is important that the mask be fabricated in a way that allows its sidewall angle to be as close to vertical as possible.

3.6.4. Mask definition

There are two main ways of patterning a mask on the surface of the wafer. Either the pattern can be etched into the mask in a prior etch step (with a resist mask) or the mask material can be evaporated onto a patterned layer of resist and the unwanted portions

can be removed with a lift-off process. Each of these techniques have been used successfully but have associated challenges which need to be considered when designing the etch process.

If etching the mask, the same selectivity criteria regarding mask erosion apply to the resist. Any deviation from vertical sidewalls will be transferred to the final etch mask and compounded when etching the film. Consequently, the lithography must allow vertical resist profiles and a process must be developed which selectively etches the mask over the resist to yield anisotropic etched features.

Lift-off processes can result in jagged or angled sidewall features if the lithography does not permit the material to be removed without tearing. Various techniques for improving lift-off profiles have been employed. These include multi-level resists, the use of a hardening agent etc. For sub-micron structures there is the added difficulty of getting the solvent under the evaporated film due to the small feature sizes. However, if the mask thickness is significantly thinner than the resist layer and the resist features are vertical or exhibit an overhang (such that no mask material is deposited on the sidewall) it is possible to perform a lift-off that provides good pattern transfer.

3.7. Effects influencing edge profile

The following effects have been observed when plasma etching. They cause problems for the resulting etch profile, which becomes increasingly important as feature size reduces into the sub-micron scale. To minimise these effects it is important to understand their causes and recognise the associated features when developing the etch process.

3.7.1. Faceting

This effect, which may influence the selectivity requirement, is a result of the physical sputtering of the mask material during the etch. The sputter yield, which is the number of substrate atoms removed per incident ion, is highly dependent on the angle at which the ions hit the surface. For many mask materials the maximum sputter yield occurs at angles greater than 0° [54]. At this *facet angle* the quicker etch rate causes a planar surface to develop and propagate as shown in Figure 3.6b. As the etch continues the

plane enlarges. This will only cause a problem if, as in Figure 3.6c the plane meets the substrate. At this point the substrate, which is now exposed to the plasma, begins to etch. This leads to non-vertical sidewall profiles as shown by Figure 3.6d. It is, therefore, of paramount importance to select a mask material that either has a suitable facet angle or has a high enough selectivity (according to the conditions stated in the previous section) to prevent loss of anisotropy.

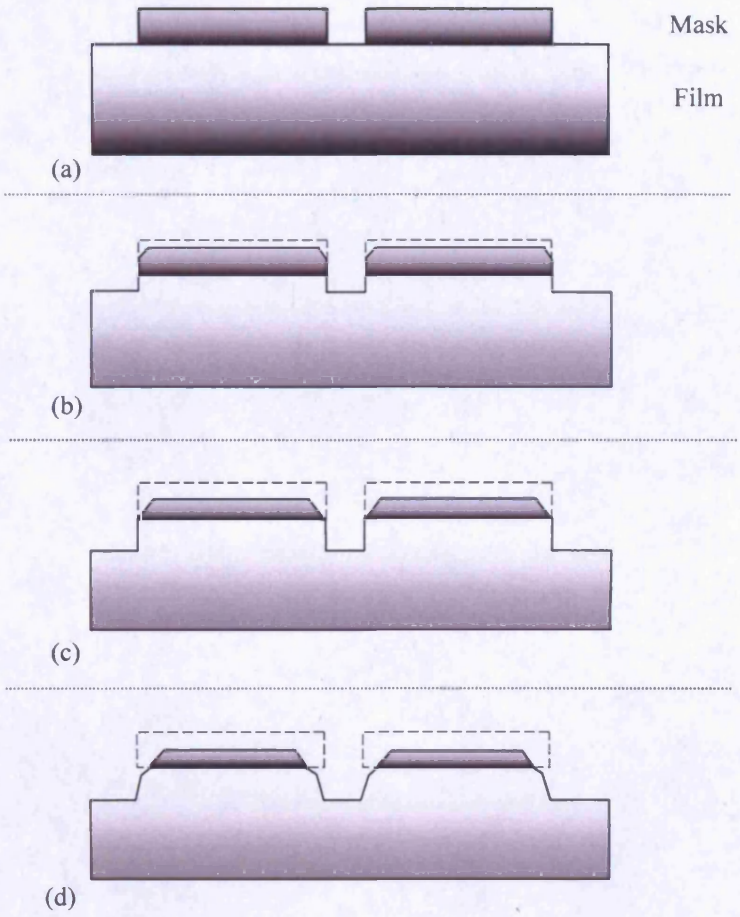

Figure 3.6 – Schematic illustration of the effect of faceting.

3.7.2. Trenching

Figure 3.7 depicts an effect called trenching, which can occur next to steps in the profile of the sample surface. Ions near the step that either have a non-normal incidence or are incident on an angled sidewall can be reflected; this results in an enhanced ion flux in these regions which in turn causes an increase in etch rate.

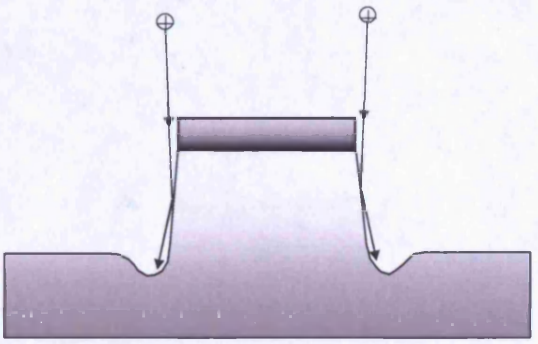

Figure 3.7 – Schematic illustration of the effect of trenching.

3.7.3. Back-scattering

Backscattering is the return of sputtered material back to the surface. This can result from three effects: collisions with particles in the plasma that reflect emitted material back to the surface, re-sputtering of emitted material that has condensed on another surface and electrostatic attraction of emitted positive ions.

3.7.4. Re-deposition

Re-deposition of material that has been removed from the surface can limit the etch rate of the sample as well as change the sidewall characteristics of etched features. Re-deposition is the result of forming involatile etch products. This is common when etching III-V materials in halogen environments. The group III halides are known to be involatile relative to most of the other etch products. Where there is insufficient thermal energy they have a tendency to remain on the surface limiting the etch rate significantly. At elevated temperatures where there is sufficient energy for desorption from the surface they can re-deposit on the sidewalls of etched features where the ion flux is low.

3.8. Effects influencing uniformity in sub-micron, high density, high aspect-ratio plasma etching

It is well know that etch rate typically decreases with feature size for dimensions below a few microns. This effect has been observed in a wide variety of materials including III-V semiconductors [55]. The effects have been described by various authors with some confusion and misuse of terminology. For the purposes of this thesis two effects

are described in simple terms. For further reading Gottscho et al. provide a good overview of the subject [56].

3.8.1. Aspect Ratio Dependent Etching (ARDE)

ARDE, also known as RIE-lag, describes the common observation that narrower features have lower etch rates than wider ones. Initially this effect was thought to be dependent on absolute feature size but was shown by Chin et al. to be dependent on aspect-ratio; as the aspect-ratio increases the etch rate decreases [57].

ARDE has implications for measured etch rates. As an etch progresses the aspect-ratio of the etched features increases accordingly and therefore etch rates of high-aspect-ratio features are time-dependent. Therefore for a rigorous distinction between aspect-ratio dependent etch rates and absolute-feature-size dependent etch rates the etch rate must be measured while varying both linewidth and etch time [56].

3.8.2. Microloading

Microloading is an effect that is often mistakenly used to describe ARDE [56,59] where the etch rate is dependent on pattern density, independent of absolute feature size. Areas of the sample with higher pattern density generally have a lower etch rate than less dense areas [58,59]. The physical origin of microloading is the same as that of the well known loading effect (sometime referred to as macroloading) [60]. Under conditions where the etching reaction is limited by transport of the neutral reactant to the surface (rather than surface-reaction-rate limited) the etch rate is limited by the depletion of reactants [56]. In macroloading this may be caused by consumption from a larger wafer or greater number of wafers in a batch process whereas microloading depletes reactants in areas of higher pattern density causing a local reduction in the etch rate.

3.9. Inductively coupled plasmas (ICP)

Capacitively driven RF plasmas, such as the RIE configuration shown in Figure 3.2, are limited in the sense that the ion-bombarding flux and ion energy cannot be varied independently (in the same way that there is not independent control of voltage and current in a pn junction diode). For a moderate ion flux and process gas dissociation the driven electrode sheath potential is high. This can result in unwanted damage to samples

and loss of linewidth control. Moreover, the combination of low ion flux and high ion energy results in a relatively narrow process window for many applications [61].

To improve control over the linewidth, etch rate, and selectivity of an etch process it is desirable to be able to independently control average ion energy and ion flux. To need to satisfy these requirements has led to the development of low pressure, high density plasma sources. An inductively coupled plasma (ICP) is one such variety of source. The RF power in an ICP reactor configuration is coupled to the plasma across a dielectric wall rather than directly via an electrode. This non-capacitive coupling is the key to achieving low voltages across plasma sheaths at electrode and chamber walls while maintaining high ion densities. Real ICP systems in fact are generally ICP-RIE configuration. To control ion energy with relative independence from ion density, the electrode on which the sample is placed (the RIE part) can be independently driven and couples capacitively to the plasma.

The plasma in an inductive discharge is created by the application of RF power to a non-resonant inductive coil. ICP sources have the advantages over other high-density sources of relative simplicity in design. No DC magnetic fields are required as in the case of Electron Cyclotron Resonators (ECR) or helical resonators. Also, RF frequencies rather than microwave powers are used. In contrast to ECRs and helicons, ICP discharges are limited to ion densities of $\sim 10^{13}$ cm^{-3}, however, typical ion densities of $10^{11} - 10^{12}$ cm^{-3} are ~10 times higher than for capacitive discharges [61].

Figure 3.8 shows a schematic representation of a cylindrical ICP source (such as the Plasmalab ICP380). A truly inductively coupled discharge has no capacitive coupling between the coil and the plasma, however, this capacitive coupling can occur if the changing bias in the coil induces a bias on the chamber walls. To reduce this coupling, an electro-static shield is placed between the coil and the plasma. The shield must allow propagation of electromagnetic waves from the coil for efficient coupling of the inductive field. A conducting metal cylinder with uniform slots cut parallel to its axis forms the shield and allows transmission of RF fields with electric field vectors perpendicular to the slots while fields with electric field vectors parallel to the slots are not transmitted. A more detailed description of the reactor used for this work is given in chapter 4.

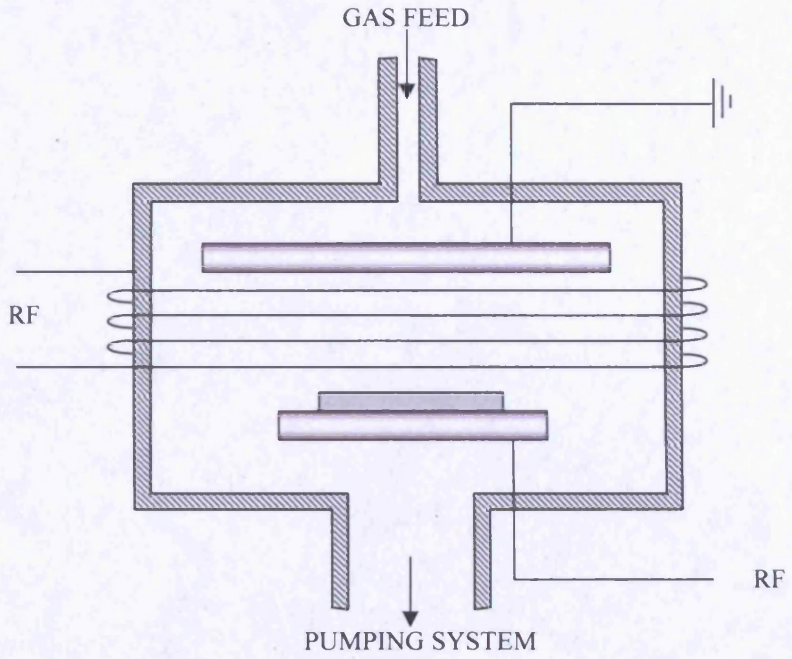

Figure 3.8 – Basic configuration of an inductively coupled plasma (ICP) reactor.

3.10. Effect of the main process parameters

In a typical modern ICP reactor there are six main process parameters that can be changed in order to modify the plasma characteristics and consequently the etch results. These are the process gas chemistry, RIE power, ICP power, stage temperature, chamber pressure and gas flow rate.

3.10.1. Gas chemistry

The need to form volatile reaction products has already been discussed in Section 3.5. Obviously the process gas has to react readily with atoms in the surface to be etched and then desorb such that the etch rate is reasonably high. However, it is not always possible to achieve the desired etch with a simple chemistry and often additive gases need to be included to enhance the effect of one or more etch mechanisms. This is particularly true when etching compound materials where the rates of formation and desorption of the reaction products are different for each of the constituent atoms.

The addition of inert gases such as Ar, He and N_2 is common when plasma etching III-V semiconductors. The purpose of such additives depends on application but can be to reduce etch rate (by diluting the etchant), increase the etch rate (by aiding removal of

involatile products), improve anisotropy (by providing non-reactive ion bombardment), improve plasma stability and to improve heat transfer.

The addition of inhibitor-forming gases is also common when etching III-V semiconductors. For example BCl_x radicals from BCl_3 have been shown to induce inhibitor-type anisotropy in Al or III-V compounds such as GaAs [62,63]. BCl_3 also acts as a native oxide etchant to aid removal of the oxide films that form (e.g. Al_2O_3) as a result of air or water molecules being present in the chamber [64,65,66].

3.10.2. RIE power

An increase in RIE power results in an increase in ion density due to the effect on ionisation interactions within the plasma. The DC bias increases because of the increased number of electrons reaching the powered electrode. The increased DC bias results in an increase in average energy of ions reaching the powered electrode and therefore impacting the sample surface.

The resulting increase in ion flux and energy has consequences for sputtering and ion-assisted chemical etching mechanisms. Etch rates due to both mechanisms typically increase with increased RIE power.

3.10.3. ICP power

An increase in ICP power increases the density of ions in the plasma without a corresponding increase in DC bias. The ICP coil couples to the plasma electromagnetically causing charged particles to exhibit cyclotron motion. Consequently, the distance travelled by the ions and electrons before being lost at the chamber wall increases causing an increased rate of collisions and ionisation events. This produces large numbers of ions, electrons and radicals. Increasing ion density in this way offers independent control of ion flux and ion energy.

3.10.4. Temperature

Temperature has important consequences for the plasma chemistry. For clarity it is important to distinguish between sample and gas temperatures. However for low

pressure discharges (such as ICPs) the distance from the surface over which the gas and surface temperatures are similar is much thicker than the mean-free path such that gas species are already at the sample temperature when they reach its surface. This is useful as, unlike the sample temperature, the gas temperature is not easily controlled.

The rate constants for chemical reactions vary with temperature with an Arrhenius dependence as in Equation 3.18.

$$k(T) = A(T)e^{-E_A/RT}$$

Equation 3.18

Where $A(T)$ is a weakly temperature dependent pre-exponential and E_A is the activation energy, the energy required by reactants to come together and combine. Consequently, for chemical etching the etch rate and selectivity are usually temperature dependent.
The morphology of etched surfaces can also be strongly dependent on temperature. In several systems temperature has an effect on post-etch surface roughness. Etching of III-V semiconductors in Cl_2 plasmas usually produces smoother surfaces at higher temperatures. The reason for this may be the increased volatility of etch products at elevated temperature or convergence of etch rates along different crystallographic planes, which also leads to a more isotropic feature profile as temperature is increased.

3.10.5. Chamber pressure

Chamber pressure affects the major phenomena that are responsible for plasma etching. The mean free path of species, sheath potential and therefore the energy of ions striking the sample and the ion to neutral ratio are all affected. When chamber pressure is decreased to below 0.1 Torr, the sheath potential increases sharply with a corresponding increase in DC bias. The mean free path is inversely proportional to pressure so as sheath potential increases the energy of ions bombarding the sample increases. Sputtering and ion-assisted chemical etching rates increase with increased ion bombardment and so lower pressures can promote etching by these mechanisms. This should allow control of whether etching is predominantly physical or chemical.

3.10.6. Gas flow rate

Control of the flow rate of each of the constituent gases entering the chamber gives some control over the precise nature of the etch chemistry (as discussed in section 3.10.1). Total gas flow rate usually has little effect on etch rate, profile and resulting surface morphology provided (a) it is high enough that reactive species aren't depleted to the point that formation of volatile products becomes rate limiting and (b) that it is not so high that the gas residence time is too low to allow reactions to take place. Gas flow rate would affect chamber pressure and therefore the density of reactive species but most modern plasma systems use adaptive pressure controllers to maintain a set pressure regardless of gas flow.

3.11. Summary

Plasmas provide a useful way of achieving the anisotropic etch profiles needed to fabricate small-linewidth, high-aspect-ratio features. This is due to the highly directional nature of the ion bombardment they provide and the importance of this ion bombardment to the overall etching mechanism if the etch chemistry is carefully chosen. Selectivity and durability of the etch mask to both vertical (physical) and horizontal (chemical) etching is of critical importance when fabricating these features. Understanding of the effects that process parameters have on etch rate, selectivity, surface morphology and feature profile is vital if control of the degree of anisotropy is required.

4. ICP etching experimental details

4.1. Introduction

This chapter will discuss the experimental details of the plasma etching studies carried out for optimising a process to fabricate photonic crystals. Information of the Plasmalab system 100 with ICP 380 and its associated services will be given. This will include details of the chamber geometry and design, RF power supplies, available process gases, vacuum system and the PC2000 control software. The measurement and characterisation techniques used will be described including the use of the laser interferometer system for measuring etch rate. Details of sample handling and in particular the mounting of samples in the chamber will also be discussed here.

4.2. Inductively Coupled Plasma-Reactive Ion Etching (ICP-RIE)

4.2.1. Plasmalab 100 with ICP 380 chamber design

All dry etching work was performed in an Oxford Instruments Plasma Technology Plasmalab system 100 with an ICP380 inductively coupled plasma (ICP) source. This system consists of a 205mm diameter anodized aluminium driven electrode, providing the capacitively coupled RIE plasma power, and a 380mm diameter cylindrical inductor situated above and centred on the lower electrode, forming the ICP source. The inner wall of the chamber is alumina and the chamber roof is an aluminium plate through which the process gas line runs. There are also two viewing ports, one on the side of the chamber and one on the roof, for viewing the chamber interior by eye and with a camera/interferometer respectively. The basic configuration is shown in Figure 4.1. There is also a quartz wafer clamp mechanism set to hold 100 mm wafers and a liquid nitrogen (LN_2) cooling circuit that are not shown in Figure 4.1 for clarity.

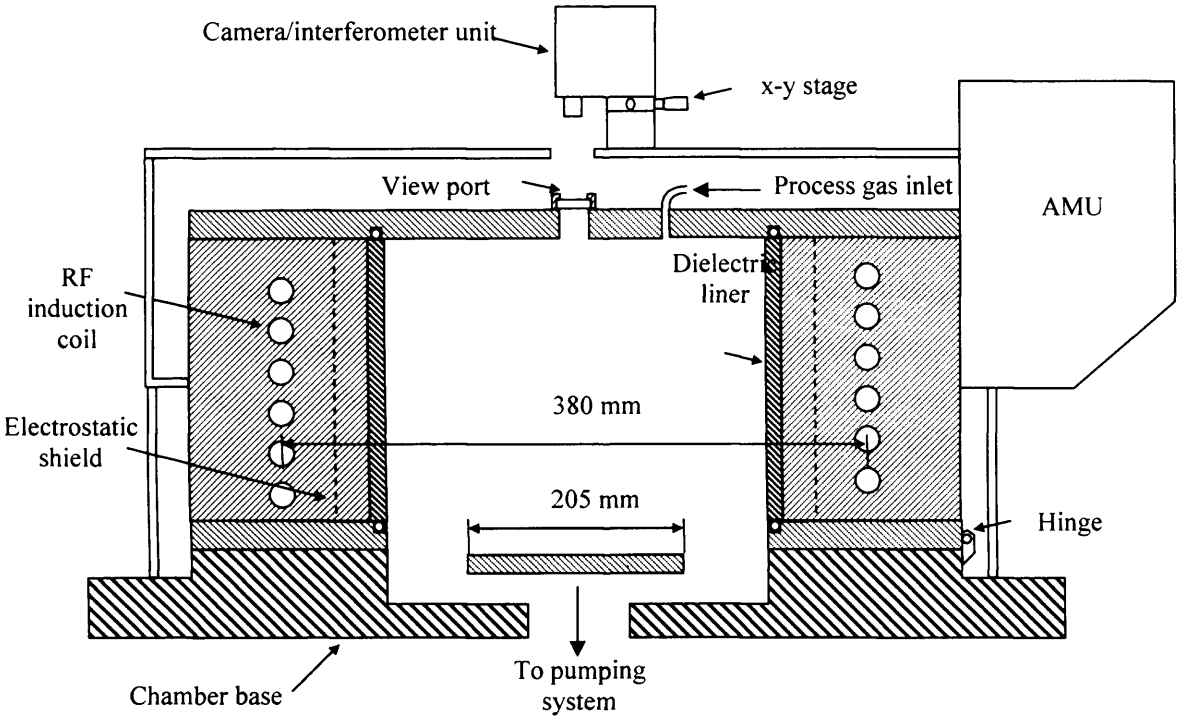

Figure 4.1 – Schematic diagram of the Plasmalab System 100 with ICP 380.

4.2.2. Wafer handling – the automatic load lock

The system has an automatic load lock that enables loading and unloading of wafers of 75 - 200 mm diameter to be done under vacuum. However for the work described here the robot arm was set up to hold 100 mm wafers as the wafer clamp used was configured for this sample size. The operation of the load lock robot arm and the wafer clamp mechanism is controlled by the PC2000 software.

4.2.3. PC2000 control software

Most system operations are controlled by the Oxford Instruments Plasma Technology PC2000 control software. This includes control of the pumping systems, the automatic load lock, and the main process variables. Inputs from the laser interferometry system are also utilised by the control software to allow automatic etch depth measurement and end-point determination.

All process parameters are measured at user defined time intervals during etch processes. The sampling rate is system limited to a maximum of 1 s^{-1}. The values of all parameters are compared with the set-point levels and if any value falls outside of its

internally preset tolerance the etch process is halted. The process data is also stored in a process log file for post-etch analysis.

There are two main control screens for operation of the system. The pumping screen allows the user to control the pumping system and wafer loading robot arm. A screen print of the pumping screen is shown in Figure 4.2. The chamber screen allows the user to input and control process and chamber parameters and view the laser interferometry data during the etch. A screen print of the main chamber screen is shown in Figure 4.3.

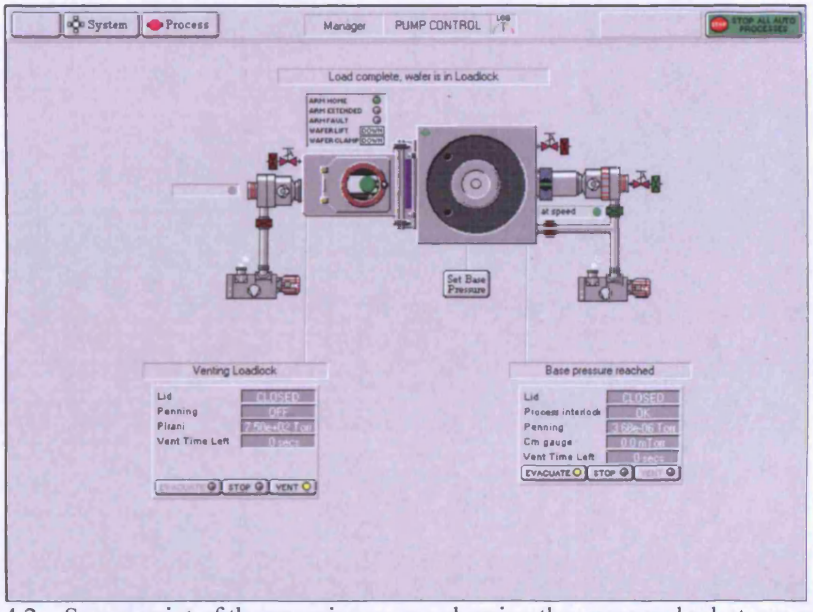

Figure 4.2 – Screen print of the pumping screen showing the pump and robot arm mimics.

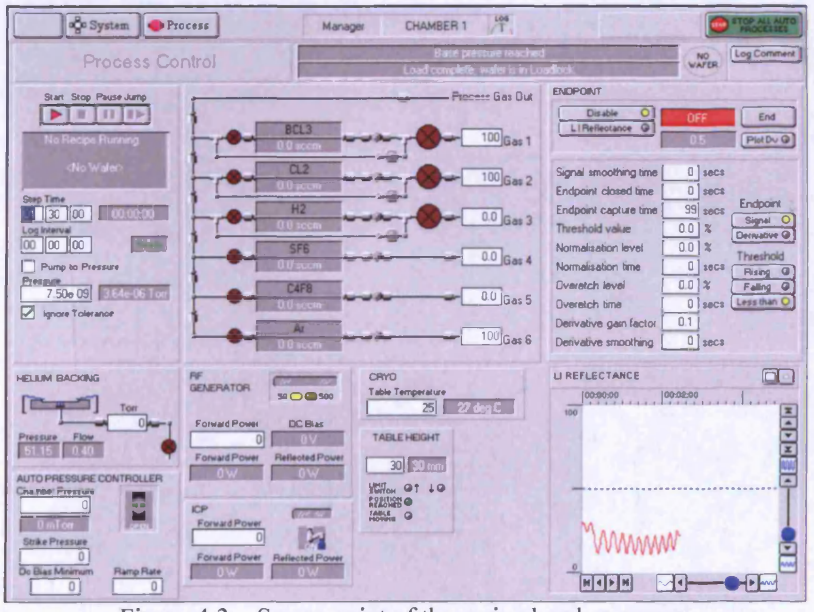

Figure 4.3 – Screen print of the main chamber screen.

4.2.4. Power supply

The RIE RF generator produces a 13.56 MHz output which is fed via an impedance matching circuit to the 205 mm diameter lower electrode at powers up to 500 W.

The inductively coupled plasma source is a 380 mm diameter coil powered by a 1.7 – 2.1 MHz generator that can deliver up to 5 kW. RF power can either be fixed at the centre frequency or allowed to sweep in frequency. In swept mode the frequency will fix when reflected power falls below an internally preset value.

The power supply units can be operated in such a way as to regulate either forward power or load power. When regulating forward power, the power output by the supply unit is fixed at the set power regardless of the amount of power reflected by any impedence mis-match. However, when regulating load power, the power is increased (by the amount reflected) to match the power coupling to the plasma with the set power, taking into account reflected power. This mode of operation ensures repeatability and is used for all etching processes described.

4.2.5. Automatic RF matching units

The Plasmalab system 100 is equipped with an automatic matching unit (AMU) for each of the power supplies. These consist of an RF tuning network with automatic impedance matching. Power to the RIE driven electrode and ICP coil is supplied via 50 Ω coaxial connectors. The matching units each contain two motor driven capacitors and a directional detection circuit which adjusts the capacitance of the capacitors to match the impedance of the RF circuit with 50 Ω. The basic layout of the matching circuit is shown in Figure 4.4.

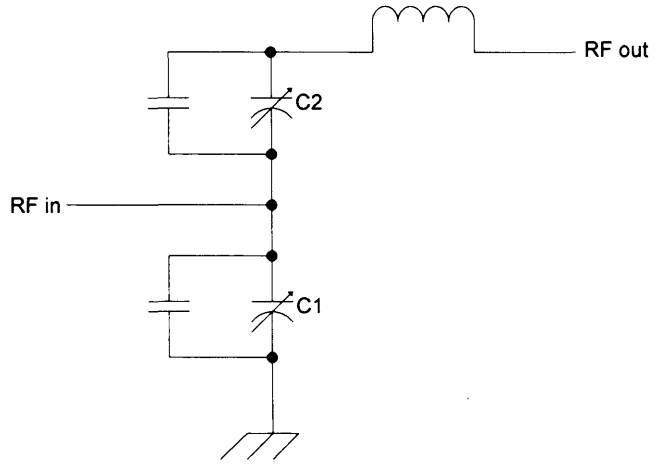

Figure 4.4 – RF matching circuit diagram

4.2.6. Pumping system

Figure 4.5 shows the layout of the pumping system for the Plasmalab system 100. The main process chamber is pumped by an Alcatel ATP 1300MT Maglev turbo-molecular pump via an adaptive pressure controller (APC). The turbo-molecular pump is backed via a heated isolation valve by an Alcatel 2063 C2 rotary vane pump. Base pressure is measured with an active Penning gauge that is disabled at pressures above 10 mTorr. Process pressure is measured by a temperature compensated capacitance manometer (CM) gauge to a maximum pressure of 100 mTorr. Chamber pressure is also monitored by a vacuum switch which closes at pressures below 4×10^{-5} Torr to allow process gases to flow and RF sources to operate.

The load lock is pumped by an Alcatel ATP 80 turbo-molecular pump backed by an Alcatel 2015 C2 rotary vane pump. Pressure is measured by a Pirani gauge at low vacuum and a Penning gauge at high vacuum.

System Leak-up rates were measured subsequent to opening the chamber to be ~4.2 mTorr min^{-1}. Typically, the main chamber base pressure was $<3.6 \times 10^{-6}$ Torr. Load lock pressure was allowed to get below 4×10^{-5} Torr (the pressure that below which processes are allowed to run) before wafers were transferred.

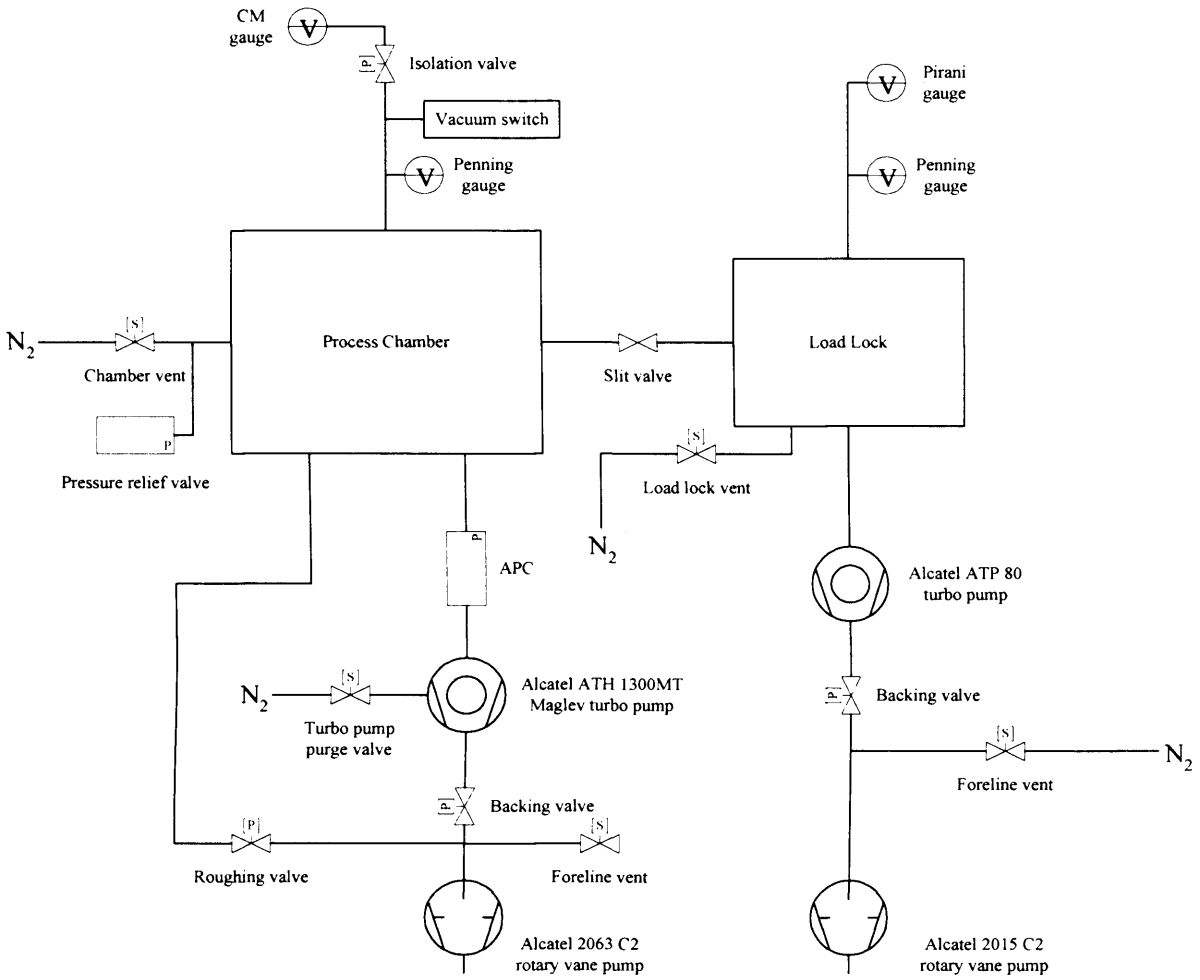

Figure 4.5 – Pumping system layout for the Plasmalab 100 system.

4.2.7. Adaptive pressure control

Automatic control of process chamber pressure was achieved using a VAT PM5 adaptive pressure controller (APC) which measures the main chamber pressure with a capacitance manometer and adjusts the bore of a controlled gate valve on the pumping side of the main chamber. For a standard process with a total gas flow of 40 sccm the minimum achievable chamber pressure is ~4 mTorr and the maximum achievable chamber pressure that can be maintained is 100 mTorr.

4.2.8. Process gas handling

Gases are supplied to the process chamber via a gas pod which can feed a mixture of process gases with flow rates specified for each constituent gas at the PC2000 software controller. The pod is a steel case with a removable cover with an extraction collar on the top of the case for safe removal of any leaking gas by the laboratory extraction

system. The gas pod can support six gas lines, however, one of the lines carries one of two gases. The gases available for plasma processes are listed in Table 4.1.

Gas Line	Process Gases
1	BCl_3
2	Cl_2
3	H_2
4	SF_6
5	C_4F_8
6	O_2/Ar

Table 4.1 – Process gases available for use in the Plasmalab 100 system.

Outputs from the gas lines are fed into a common mixing manifold that is connected to the process chamber gas inlet line. There are pneumatically operated shut-off valves in each gas line and a separate interlock shut-off that prevents the opening of any of the gas line shut-off valves when the pod is open. The gas pod receives signals from the system controller to control the valves and mass flow controllers (MFC) in each gas line.

There are two types of line carrying gas to the pod for toxic and non-toxic process gases. In the non-toxic gas line, gas flows through a 2 μm filter, then through the MFC. The MFC controls the flow of gas as entered into the PC2000 software. The gas then flows through the pneumatically controlled shut-off valve into the common manifold where it mixes with other process gases before flowing to the process chamber. This is shown schematically in Figure 4.6.

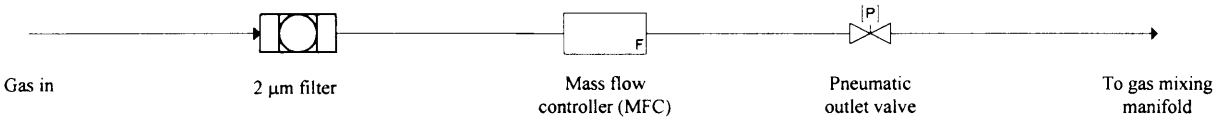

Figure 4.6 – Schematic diagram of the non-toxic gas line

In the toxic gas line, shown in Figure 4.7, there is an additional bypass line to allow evacuation of toxic gases by pumping down the process chamber. With the bypass valve closed and inlet and output valves open, gas flows through a 2 μm filter and the MFC and into the mixing manifold as in the non-toxic line. However, with the bypass valve open the gas flows directly into the manifold bypassing the MFC.

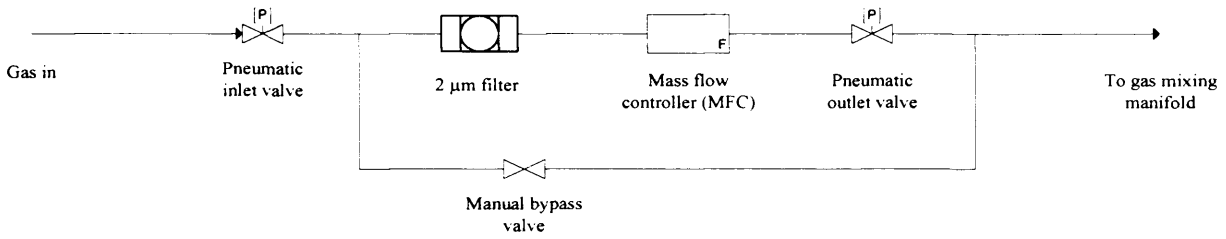

Figure 4.7 – Schematic diagram of the toxic gas line

4.2.9. Stage temperature control

The sample stage can be heated or chilled to temperatures in the range <-100 °C to 400 °C. Heating is provided by an electrical heater and cooling is achieved by LN_2 flow. The stage temperature is measured with a thermocouple and controlled with a PID controller which gives appropriate signals to the heater unit and a solenoid that turns the LN_2 flow on and off.

4.2.10. Helium backing flow

The purpose of He backing is to keep the wafer temperature close to that of the temperature-controlled stage. This achieved by feeding He, which is inert and has high thermal conductivity (142.2 $mWm^{-1}K^{-1}$ at 273 K [67]) through a small hole in the driven electrode underneath the wafer, where it flows radially to the periphery of the wafer. A schematic diagram of the stage and wafer clamp assembly is given in Figure 4.8. The supply of He is pressure controlled between 0 – 20 Torr by adjusting the gas flow. Gas flow in the He line is measured with a flow meter. Typically, a pressure of 10 Torr requires a gas flow of 12 -15 sccm.

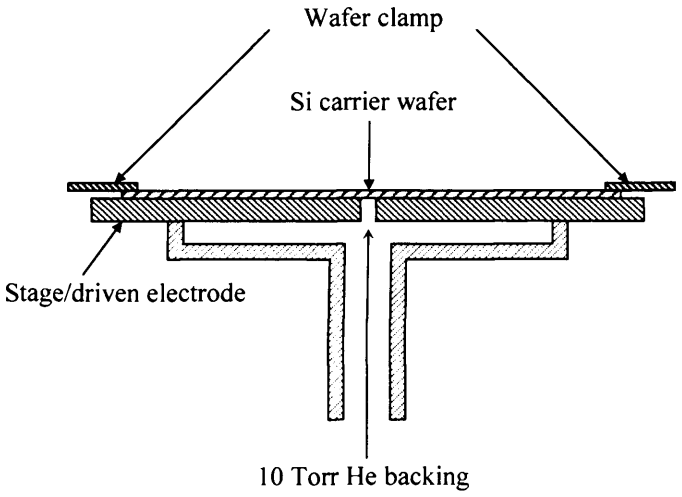

Figure 4.8 – Schematic diagram of the stage/wafer clamp assembly showing how the He backing gas flows from under the centre of the carrier wafer and radially out into the chamber.

If the wafer is clamped correctly to the stage, the chamber pressure will rise slightly (a few mTorr) with a backing pressure of 10 Torr. If the wafer is clamped too tightly, the gas flow will be choked reducing the effectiveness of the backing flow. This is evident by a slow pressure decay when the He flow is turned off. If the wafer in not sufficiently clamped the gas flow will rise to match the required pressure causing an excessive rise in chamber pressure and a high load on the turbo-molecular pump.

4.2.11. Chamber preparation

Most processing carried out in the chamber is chlorine based and generally the main process chamber was kept under constant vacuum as samples were loaded via the load lock. Therefore no regular chamber preparation or conditioning was required. However, when other processes (e.g. C_4F_8 etching of SiO_2 or Si_3N_4) were carried out the chamber was cleaned with a 30 minute O_2 plasma (1000 W ICP power and 100 W RIE power) to remove any residual polymer build up on the chamber interior. In the case of significant usage of different etch chemistries or after the process chamber had been opened for maintenance purposes, test runs were carried out on samples with known etch rates for comparison. At no time was there significant discrepancy between measured and expected etch rates indicating that the chamber conditions did not change.

4.3. Material details

The purpose of these studies was to develop a process to fabricate devices in laser material that contain photonic structures. Given the facilities available in the Cardiff cleanroom SiO_2 and Ni were the main candidates for the mask material. For the etch study results described in Chapter 5 laser structures rather than bulk samples of the component compounds were etched. The layered structure of a laser sample lends itself to the technique used to measure etch rates (described in Section 4.5.2). Using this technique it is possible to measure the etch rate of each layer within the structure; this would be labour intensive and costly if conventional etch rate measurements (Section 4.5.1) on bulk samples were carried out. Also, the aim of this work is to define a process for etching laser structures so using them for the etch studies allows the challenges involved to become apparent sooner.

Two similar laser structure wafers were used in these studies, one for the work to define the conditions for selective etching (EPIQ9502287#F2) and one for the work to assess the effect of plasma chemistry on the sidewall profile and surface morphology (EPIQ9503287#F2). The basic structure of both samples is illustrated in Figure 4.9. Both samples are grown on GaAs substrates and topped with a ~10nm $Ga_{0.51}In_{0.49}P$ interface layer and a ~0.5 μm GaAs cap layer both of which were removed from the samples to expose the top cladding layer before making etch rate measurements. EPIQ9502287#F2 consists of a ~0.24 μm $(Al_{0.3}Ga_{0.7})_{0.51}In_{0.49}P$ waveguide core within ~1μm $(Al_{0.7}Ga_{0.3})_{0.51}In_{0.49}P$ cladding layers. The waveguide contains two ~6.8 nm $Ga_{0.41}In_{0.59}P$ quantum wells. The layer structure is ~2.4 μm thick in total. EPIQ9503287#F2 consists of a ~0.25μm $(Al_{0.3}Ga_{0.7})_{0.51}In_{0.49}P$ waveguide core within ~1 μm $(Al_{0.7}Ga_{0.3})_{0.51}In_{0.49}P$ cladding layers. The waveguide contains two ~5 nm $Ga_{0.41}In_{0.59}P$ quantum wells. The layer structure is ~2.7 μm thick in total.

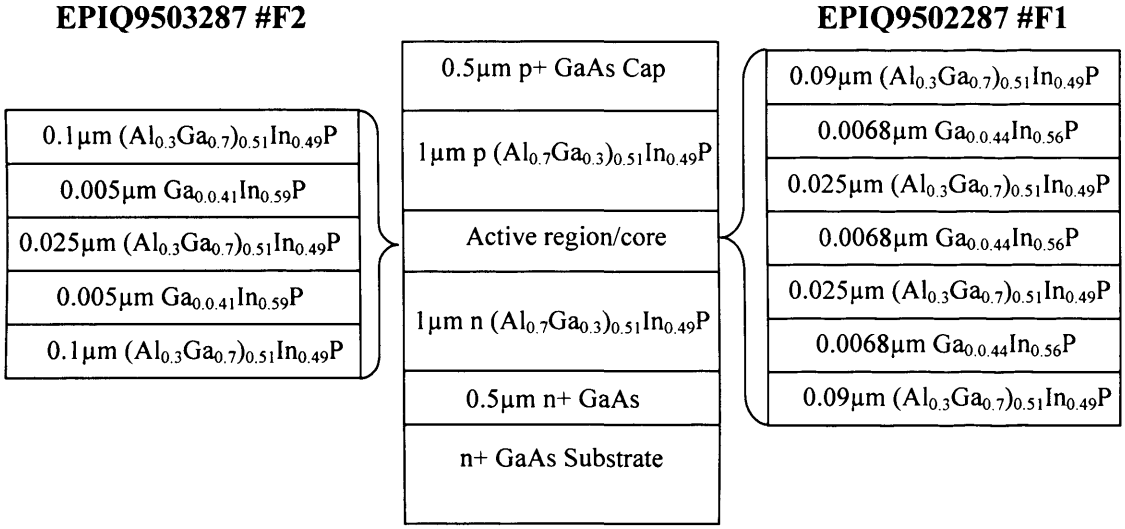

Figure 4.9 – Schematic Illustration of the basic layer structures to be etched.

The etch rate of SiO_2 was measured separately using 8×8mm samples taken from a single, thermally oxidised SiO_2 on Si, four inch wafer. SiO_2 deposited onto small (8×8 mm) Si samples by electron beam evaporation, compatible with laser processing, produced very similar etch rates but thermally oxidised SiO_2 was used in this study in the interests of reproducibility and convenience.

For measurement of Ni etch rate, nominally 60 nm of Ni was evaporated onto SiO_2 on Si samples. This allowed accurate determination of the etch time by laser interferometry (details in 4.5.2). Film thickness was measured with a stylus profilometer (details in section 4.5.1).

4.4. Sample preparation

4.4.1. Sample size

Etch study samples were cleaved to be 8 × 8 mm and mounted on 4 inch Si carrier wafers for compatibility with the automatic wafer handling described in section 4.2.2. Using a small sample can lead to complications when the etch rate of sample and carrier differ. One consequence is that active species in the plasma are consumed at different rates leading to variations in the etch rate of the sample in the vicinity of its edges, a so-called edge effect. Since the observed etch rate of the Si carrier wafer (typically <0.1 $\mu m\ min^{-1}$) was often lower than the etch rate of the sample, edge effects were expected and observed. In all the studies described here, this effect was avoided by taking care to make all measurements and analyses in the centre of the sample.

4.4.2. Sample cleaning

Samples were cleaned by successive five minute submersions in trichloroethylene, acetone, methanol and isopropanol (IPA) at ~100 °C. For particularly dirty samples this was preceded by carefully wiping the sample surface with a cotton bud soaked with Deacon 90 (a proprietary degreaser) followed by a 30 s deionised (DI) water rinse. As the GaAs cap layer on AlGaInP structures oxidises in air, a de-oxidation step was carried out on these samples immediately prior to etching. This consisted of a 30 s soak in 5 ml of NH_3 (ammonia) mixed with 100 ml of DI water followed by a 30 s rinse in DI water. After each cleaning step the sample was dried with a N_2 gun.

4.4.3. Etch rate/selectivity study samples

Samples used solely for etch rate/selectivity measurements were generally blanket etched (not masked). This was possible because of the etch rate measurement technique employed (details of which are given in section 4.5.2). For calibration or verification

purposes some masked samples were also etched and the etch rate measured independently by the technique detailed in section 4.5.1.

4.4.4. Patterning of SiO_2 ridge masks

SiO_2 masks were defined using a C_4F_8 RIE plasma etch step with a photoresist mask. SiO_2 was deposited in an Edwards electron beam evaporator. The photoresist used was Shipley Microposit S1813 SP15 spun on at 6 krpm for 45 s to give a film thickness of approximately 1.3 μm. Following spin-on, samples were pre-baked for 3 minutes at ~100 °C.

4 μm wide ridges were defined lithographically using a Karl Suss Hg-lamp optical mask aligner. Samples were exposed for 6 s and developed in Shipley Microposit 2401 developer for 15 s. This was then followed by a 15 s rinse in DI water.

Transfer of the pattern into the SiO_2 was achieved using a C_4F_8 RIE process in the Plasmalab 100 system. This process has 40 sccm gas flow, 275 W RIE power, 5 mTorr chamber pressure and 25 °C stage temperature. The dc bias for this process was ~380 V. The SiO_2 etch rate was measured to be 0.08 μm min^{-1} and the selectivity with respect to resist was measured to be ~2.4.

4.4.5. Patterning of Ni ridge masks

Ni ridge masks were defined using a two-layer resist lift-off technique. The first resist layer, Brewer Science WiDE 8 EXP04002, was spun on at 4 krpm for 45 s. This was followed by a 90 s bake at ~100 °C and a further 150 s bake at ~125 °C. Then the second layer, Shipley Microposit S1813 SP15, was spun on at 6 krpm for 45 s. This was followed by a 120 s baked at ~100 °C. The total resist thickness is ~ 2 μm.

4 μm wide ridges were defined lithographically using a Karl Suss Hg-lamp optical mask aligner. Exposure time was 6 s. Edge removal was done prior to exposure to ensure close contact between the mask and the sample. Exposed patterns were developed in Brewer Science PSC developer for 3 minutes. This was followed by a 3 minute rinse in DI water. A 1 minute de-scum process was then carried out in a 50 W O_2 RIE plasma.

Ni was then deposited in an Edwards thermal evaporator at a rate of 0.1 nm min^{-1} to a thickness of 60 nm. The sample was then submerged in acetone to lift off the unwanted Ni. Finally the sample was placed in the developer for a further minute to remove residual resist.

4.4.6. Patterning of sub-micron feature masks

Ni masks were used for etching of sub-micron features. These were defined using a lift-off process following electron beam lithography. Sub-micron features were patterned in Microchem Polymethylmethacrylate (PMMA) 950k spun on for 45 s at 6 krpm to a thickness of ~200 nm. Patterns were defined by electron beam lithography. Details of the electron beam system are given in Section 4.4.7. Development was carried out in a solution of Microchem methyl isobutyl ketone (MIBK) and IPA for 30 s followed by a 30 s IPA rinse. Ni was then deposited in an Edwards thermal evaporator at a rate of 0.1 nm min^{-1} to a thickness of 60 nm. The sample was then submerged in acetone to lift off the unwanted Ni.

4.4.7. Raith 50 electron beam lithography system

Electron beam lithography was carried out in a Raith50 e-beam lithography system incorporating a Phillips XL scanning electron microscope (SEM) with a single crystal LaB_6 filament and an electrostatic beam blanker. In SEM operating mode the system can be used for high resolution imaging. With the control of the beam taken over by the Raith software the system uses a finely focused beam of electrons to define structures with linewidths down to <50 nm on wafers of up to 2 inches in diameter. Beam acceleration voltages of 200 eV – 30 keV are available though typically accelerating voltages of 20 - 30 keV are used for pattern definition. Stage position is measured with a laser interferometer stage that has a resolution of 2 nm allowing multilevel lithography. The system is located in a class 1000 clean room.

4.5. Etch rate measurement

4.5.1. Stylus profilometry

Feature depth was measured using a Sloan Dektak IIa stylus profilometer. The mask thickness prior to etching, the height of the etched feature with the mask still in place and then the height of the etched feature after removal of the mask were measured.

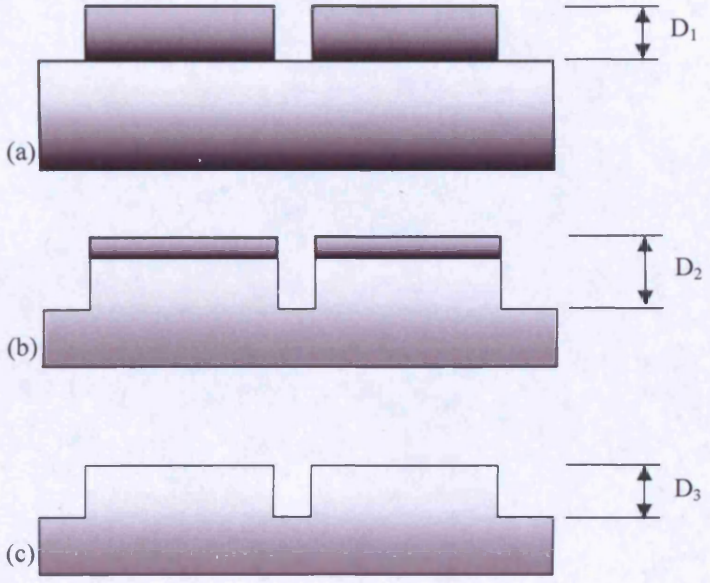

Figure 4.10 – Definition of the depths measured to calculate etch rate and selectivity from a etched feature.

From Figure 4.10 the etch rate of the film is given by

$$R_f = \frac{D_3}{t}$$

Equation 4.1

where t is the time taken to etch the film. The selectivity of the etch to the film over the mask is given by

$$S_m^f = \frac{D_3}{D_1 - (D_2 - D_3)}$$

Equation 4.2

4.5.2. Laser interferometry

The Plasmalab 100 system is equipped with a normal incidence laser interferometry unit operating at 677 nm. This is mounted on top of the process chamber and the beam is aimed through a view port in the top plate onto the sample as shown in Figure 4.1. Reflections from the top surface of the sample, and from underlying layer interfaces in materials transparent at the laser wavelength, undergo constructive/destructive interference and are detected by a sensor in the unit. The detected signal is characteristic of the laser wavelength, the film thicknesses, and the refractive indices of the films. As the sample etches and the thickness of the top film changes the detected signal oscillates sinusoidally as the interference alternates between being destructive and constructive. A typical intensity trace for an AlGaInP laser structure is shown in Figure 4.11.

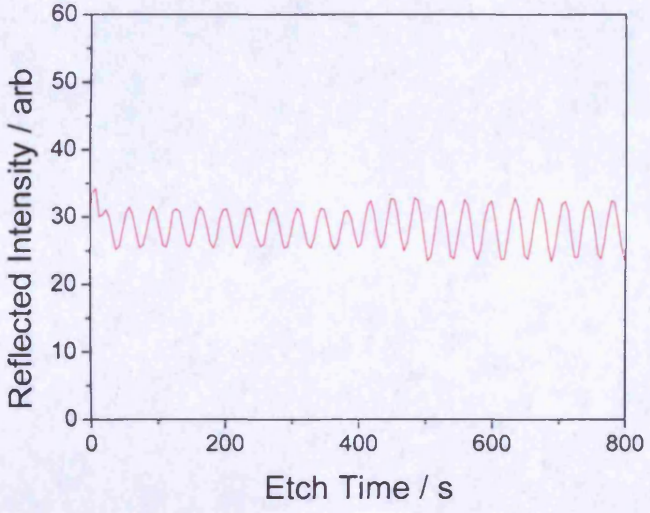

Figure 4.11 – Typical laser interferogram of the etching of an AlGaInP laser structure.

The depth etched in one period of oscillation, Δd, is given by the half wavelength as this value is equal to the difference in optical path length required for complete destructive interference. For an incidence angle θ_i, Δd is given by [68]

$$\Delta d = \frac{\lambda}{2\sqrt{n^2 - \sin^2 \theta_i}}$$

Equation 4.3

Which for normal incidence is reduces to [69]

$$\Delta d = \frac{\lambda}{2n}$$

Equation 4.4

Where n is the refractive index of the film being etched and λ is the laser wavelength. This can be used to measure the etch rate if the period of oscillation is known as described by Hayes et al [68]. The etch rate is given by

$$R_v = \frac{\lambda}{2nT}$$

Equation 4.5

Where T is the period of oscillation.

The etch rate can often be accurately determined from one period of the interference oscillation. This method has the advantage that no etch mask is required so prior processing is limited to cleaning. There is also no need to remove the sample for post-etch measurement as is necessary when using the profilometry technique described in section 4.5.1. Also many measurements can be made on one sample in relatively quick succession allowing data to be collected more rapidly than is possible when using conventional post-etch stylus profilometry.

A further advantage is that this technique allows the time-dependent etch rate to be monitored using multiple oscillations. The use of post-etch stylus profilometry measurements of the etch depth gives an accurate measure of average etch rate of the material. However, this can be misleading if the etch rate changes as the etch progresses (for example as the sample temperature increases). This turns out to be very advantageous when measuring etch rates in In-containing semiconductors in Cl-based plasmas due to the temperature and subsequently time-dependent nature of the process. This is discussed in greater detail in Chapter 5.

The spot size required to obtain a good quality interferogram is usually very small (typically only ~10 μm in diameter) compared to the area being etched. Consequently non-uniformities in the film thickness or etch rate (due perhaps to varying feature size

or edge effects) will not be picked up. Care must therefore be taken when using laser interferometry to measure etch rate to keep the laser spot away from the sample edge. When etching small features, with the interferometer spot focussed on a large exposed area to measure etch depth/rate it is important to bear in mind the potential for error in the outcome and, if necessary, calibrate measurements by etching test structures.

The main source of error is the measurement of the period. At high etch rates the sampling time is the largest error source being system limited to a minimum 1 s.

At 677 nm SiO_2 and all of the phosphide layers are transparent but Si and GaAs substrates are not. Due to the small difference in refractive index between the different compositions of the phosphide layers any observable change in period of oscillation must result from a change in etch rate and not from the refractive index change. Values of refractive index at 677 nm were calculated using the modified single effective oscillator (MSEO) model [17] to be n=3.36 for $(Al_{0.3}Ga_{0.7})_{0.51}In_{0.49}P$ and n=3.23 for $(Al_{0.7}Ga_{0.3})_{0.51}In_{0.49}P$. A spatially averaged refractive index value of 3.25 is used to calculate etch rate. This gives a value for Δd = 0.1 μm. The number of oscillations produced when etching the whole structure was in agreement with the thickness measured by the wafer supplier [70] on another piece of the same wafer by stylus profilometry following a selective wet etch.

The thickness of the SiO_2 layer produced by thermal oxidation was measured by white light reflection spectroscopy by the supplier to be (166±1) nm. The time taken to remove the whole layer was measured to give a measurement of etch rate. A typical intensity trace for SiO_2 on Si is shown in Figure 4.12.

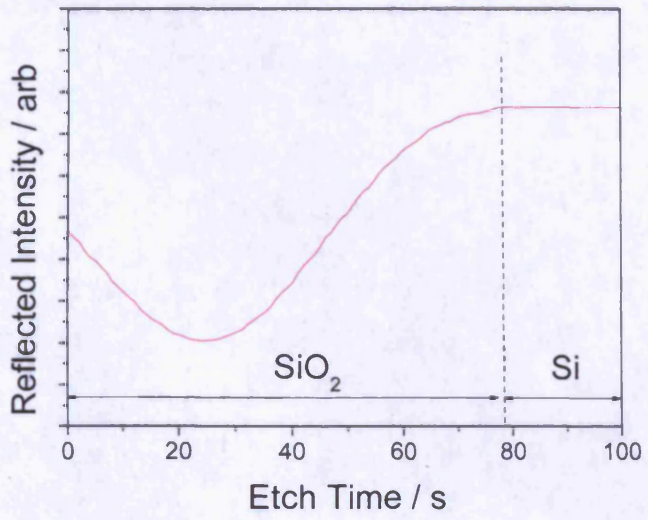

Figure 4.12 – Tpical laser interferogram of the etching of a SiO_2 on Si sample

For measurement of the etch rate of opaque metal masks such as Ni the material was evaporated onto transparent SiO_2 before etching. This allowed easy determination of the etch time with the laser interferometer. A typical trace of such an etch is given in Figure 4.13. Average etch rate was then calculated by dividing the film thickness (measured by stylus profilometry) by the etch time.

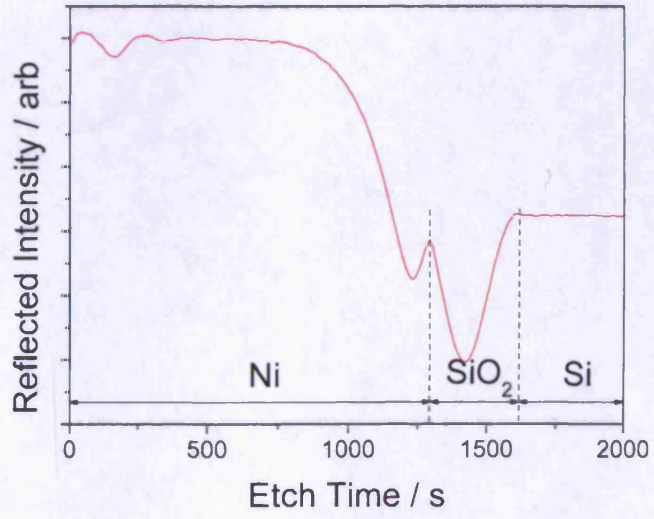

Figure 4.13 – Laser interferogram of the etching of a Ni/SiO2/Si sample showing the points at which the interfaces are reached.

4.6. Sidewall profile analysis

Measurements of feature dimensions were made using the Phillips XL scanning electron microscope (SEM) that forms part of the Raith50 lithography system. Samples were cleaved across the etched features and mounted on angled copper blocks at 15 ° to the vertical to allow the sidewall profile to be imaged. The system allows measurement of linear dimensions to assess the sidewall profile.

4.7. Surface roughness measurements

Roughness values are calculated using a least squares algorithm and consequently are more sensitive to the heights of features than their spatial frequency. Therefore care must be taken to choose a scan area that it is large enough to observe surface roughness over the appropriate length scale. RMS roughness is given by

$$R_{RMS} = \sqrt{\frac{\sum_{i=1}^{N}\left(Z_i - \overline{Z}\right)^2}{N}}$$

Equation 4.6

Where N is the total number of points, Z_i is the value at a given point, and $\overline{Z}$ is the flattened average of all Z values within the scan area.

Post-etch surface roughness measurements were performed on the samples using a Digital Instruments Nanoscope IIIa multimode atomic force microscope (AFM) over a 10 × 10 μm scan area located centrally between the ridges.

5. Results of ICP etching studies

5.1. Introduction

In this chapter I will detail the results of the plasma etching studies required to develop a process for fabricating photonic crystals. This includes the results of the selectivity and etch rate studies for the etching of AlGaInP with SiO_2 and Ni masks in $Cl_2/BCl_3/Ar$, a comparison of the suitability of SiO_2 and Ni as mask materials, and a study into the effect of plasma chemistry (Cl_2/BCl_3:Ar ratio) on the sidewall profile and surface morphology. Finally, a process for fabricating sub-micron, high aspect ratio features in a single step in AlGaInP/GaAs laser structures is described.

5.2. Experimental design

The etch study for fabricating AlGaInP photonic structures was split into two distinct stages; the first being a study into how to obtain the high selectivity required to etch photonic crystals and the second to determine how to adjust the selective etch to achieve vertical sidewalls without compromising selectivity. The rationale for this approach is that without the etch being highly selective in the first instance it is not possible to fabricate photonic crystals even if the etch process is completely anisotropic. It is therefore important to understand how the relative etch rates depended on process conditions and obtain a selective process before attempting to etch vertical structures. With a selective etch process in hand one can be more certain that effects causing loss of anisotropy are related solely to the process parameters and not the condition of the etch mask.

5.3. Selectivity study experimental details

The process was characterised as a function of the main process variables (sample temperature, process powers, plasma chemistry and chamber pressure) by measuring etch rates of separate AlGaInP, SiO_2 and Ni samples. This allowed the selectivity of AlGaInP with respect to SiO_2 and Ni, the potential mask materials, to be determined. Measurements of etch rate give insight into the role of different etch mechanisms and increasing the etch rate is often a desirable goal. However, when etching small feature-size, high-aspect-ratio structures it is more important that the process is selective in

favour of the semiconductor. To minimise processing problems that cause loss of anisotropy, such as faceting, a selectivity at least twice that of the simple ratio of etch depth to mask thickness is usually required (as per Section 3.6.2). Therefore, to etch completely through the active region and lower waveguide layers (~2500 nm) of a typical laser structures with a 50 nm thick mask, a selectivity of >100:1 is needed.

A possible complication of using small 8×8 mm samples relates to the temperature reached during plasma process. Simply placing the samples on the carrier (unclamped) provides a thermal contact between sample and carrier that is quite poor. This means that energy transferred to the sample from the plasma cannot be efficiently removed with consequences for the temperature. This was initially investigated as an approach to intentionally increase the sample temperature and consequently the etch rate. A second approach was to establish a better thermal contact and then heat the sample stage. To achieve thermal contact the samples were mounted with Fomblin oil (clamped). Etch rate and selectivity were measured for temperatures of 20 °C to 190 °C. Above 190 °C there were difficulties in maintaining the thermal contact between sample and carrier wafer due to evaporation of the Fomblin oil.

Measurements of etch rate and selectivity were also made for ICP powers from 500 W to 2500 W and RIE powers from 50 W to 150 W. The total gas flow was kept at 40 sccm throughout the investigation. The BCl_3 and Cl_2 composition was varied from pure BCl_3 to pure Cl_2 to investigate the effect of plasma composition. Ar was also added to the gas mix with the relative amount of BCl_3 and Cl_2 kept at 25:15 and the amount of Ar varied from 0 % to 100 %. Chamber pressure was varied from 5 mTorr to 20 mTorr. Process parameters were varied systematically in a pseudo-random order while the other process conditions were kept constant at the values given in Table 5.1, unless otherwise indicated. The 'standard' process conditions are labelled in each figure by a dashed vertical line.

BCl_3 flow	25 sccm
Cl_2 flow	15 sccm
RIE Power	100W
ICP Power	1000W
Chamber Pressure	10 mTorr
He Pressure	10 Torr

Table 5.1 – 'Standard' process parameters used in the selectivity study

5.4. Selectivity study results

5.4.1. Temperature dependence

Using the standard process conditions given in Table 5.1 and varying the temperature from 20 °C to 190 °C, the dependence of the etch rate of clamped AlGaInP, SiO_2 and Ni was examined and the results are shown in Figure 5.1. Removal of $InCl_3$ is the result of the combined effect of plasma-assisted and thermally-assisted desorption. Within error there is no change in the etch rate of AlGaInP between 20 °C and 100 °C. As the temperature is increased above 100 °C there is a significant increase in etch rate, the form of which is consistent with a predominantly thermally-assisted desorption process. However, at temperatures below 100 °C there is a non-zero etch rate that exhibits no further decrease with decreasing temperature suggesting that below 100 °C the $InCl_3$ removal is predominantly plasma-assisted.

The temperature dependence of the etch rate of SiO_2 under the same conditions is very different. The etch rates are lower than for AlGaInP and within error there is no change in etch rate over the whole temperature range presumably as there are no involatile etch products. This leads to a selectivity (shown in Figure 5.2) that, in this range of temperatures, increases significantly with increased temperature.

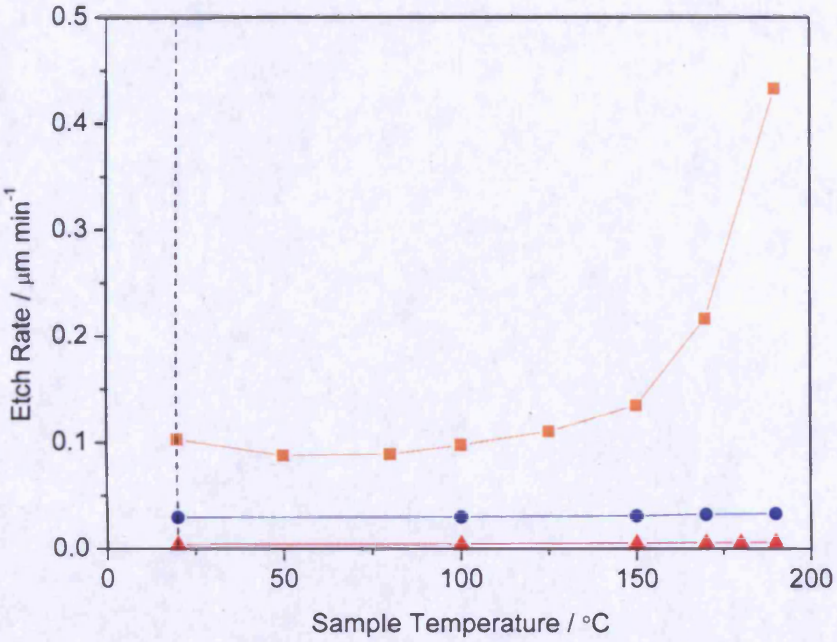

Figure 5.1 – Etch rate of AlGaInP (orange squares), SiO_2 (blue circles) and Ni (red triangles) as a function of sample temperature (all other conditions as in Table 5.1, dashed vertical line shows the 'standard' conditions).

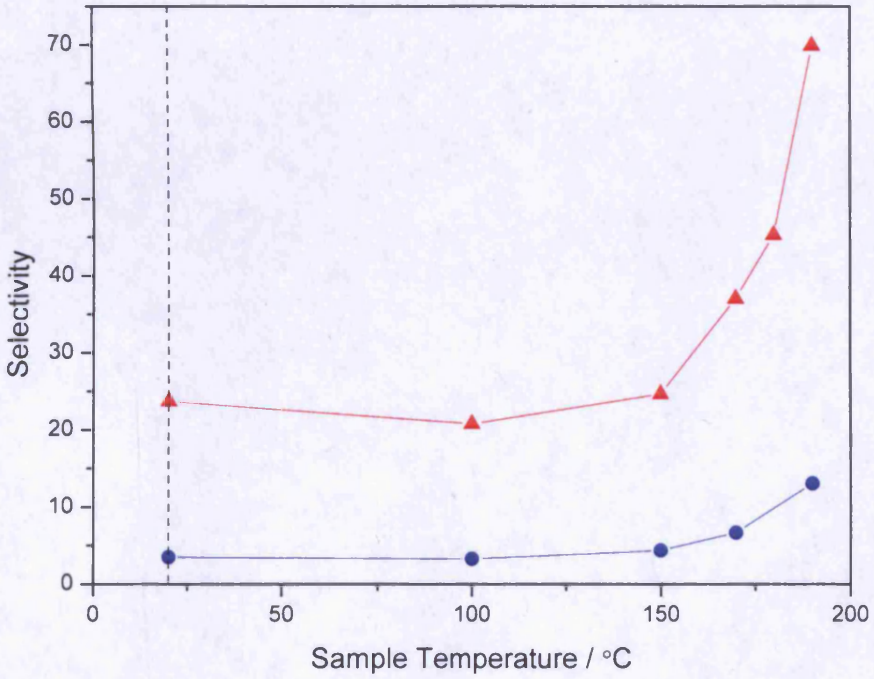

Figure 5.2 – Selectivity of the AlGaInP etch with respect to SiO_2 (blue circles), and Ni (red triangles) masks as a function of sample temperature (all other conditions as in Table 5.1, dashed vertical line shows the 'standard' conditions).

The Interferograms shown in Figure 5.3 show the difference in etching characteristics between clamped and unclamped samples. The etch rate is plotted as a function of time for each sample in Figure 5.4. Etch conditions are as in Table 5.1 with the exception that a higher value of 1500 W ICP power is used. Etch rate is determined from single oscillation period measurements. There is a clear difference in the behaviour of etch rate of samples that have been mounted with and without oil. After 2 minutes there is a significant increase in etch rate for the sample that is unclamped. From comparison with Figure 5.1 it can be seen that this is consistent with a temperature dependent etch rate where after 2 minutes the temperature is >100 °C. This is in contrast to the sample that is clamped where the etch rate remains stable meaning sample temperature does not increase above ~100 °C during the etch. The constant etch rate also indicates that the Al:Ga ratio plays little role in determining the etch rate. This is also consistent with the expectation that the formation and subsequent removal of $InCl_3$ is the dominant factor in determining the etch rate for the In-containing layers.

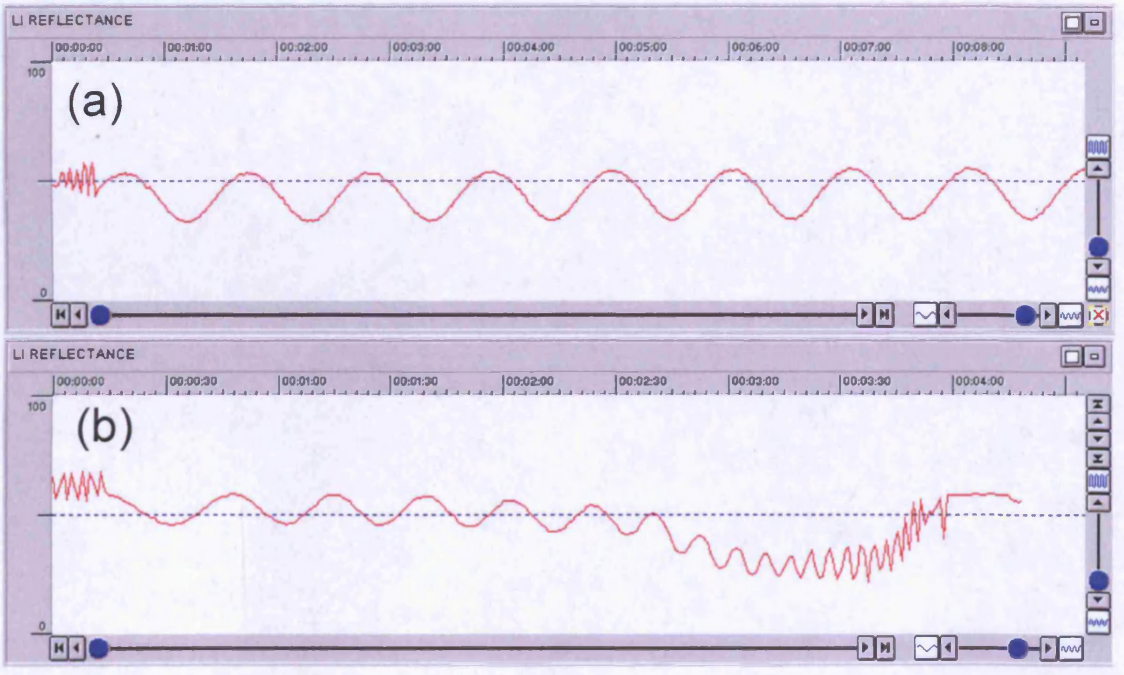

Figure 5.3 – Inteferograms of the etching of two samples, (a) mounted with oil (bottom) and (b) dry mounted (top). ICP power is 1500 W and the sample temperature is 20 °C at the beginning of the etch (all other conditions as in Table 5.1).

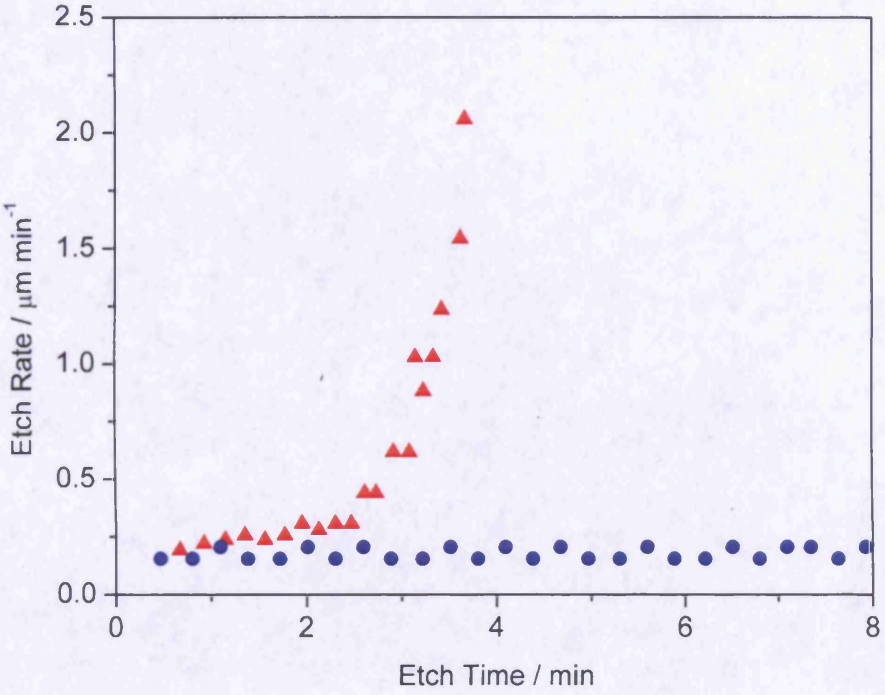

Figure 5.4 – Etch Rate as a function of time for two samples, mounted with oil (blue circles) and dry mounted (red triangles). ICP power is 1500 W and the sample temperature is 20 °C at the beginning of the etch (all other conditions as in Table 5.1).

At temperatures above 100 °C where $InCl_3$ becomes more volatile there are increases in etch rate over multiple oscillations. Etching a sample for 4.5 minutes using powers of 200 W RIE and 800 W ICP at 165 °C, the etch rate was observed to increase by a factor of 2. However, the etch rate was stable for the first 1.5 minutes (corresponding to 2 AlGaInP oscillations). This is consistent with the expected exponential dependence of etch rate on temperature. At 190 °C, even with ICP powers up to 2500 W, the etch rate is stable over at least one oscillation within error. Therefore, etch rates are stable for all the single oscillation etches employed in this study. However, under these conditions they are expected to increase during the etching of deep structures, although this need not present difficulties provided the etch rate can be monitored.

5.4.2. Power dependence

The effects of RIE and ICP powers on the plasma are complex and difficult to measure directly. Increased RIE power results in increases in both ion flux and ion energy. Increased ICP power, whilst affecting the ion energy, mainly results in an increase in ion flux.

The dependence of etch rate of AlGaInP on ICP power is shown in Figure 5.5 for temperatures of 20 °C to 190 °C. Similar behaviour is seen for a wide range of temperatures where the etch rate of AlGaInP increases with ICP power to ~1500 W. As ICP power is increased further the etch rate dependence weakens. Figure 5.6 shows the stabilised DC bias, measured without a wafer in place, which is related to average ion energy. The DC bias increases sharply to a maximum (this is not a transient effect but probably a consequence of the changing geometry of the inductively coupled plasma) then decreases slowly between ~600-1500 W above which it decreases rapidly. This rapid decrease starts at about the same power that the rate of increase in etch rate slows. It is known that the ion flux increases linearly with the ICP power [71]. Therefore, these results imply that the AlGaInP etch rate is sensitive to both ion energy and ion flux.

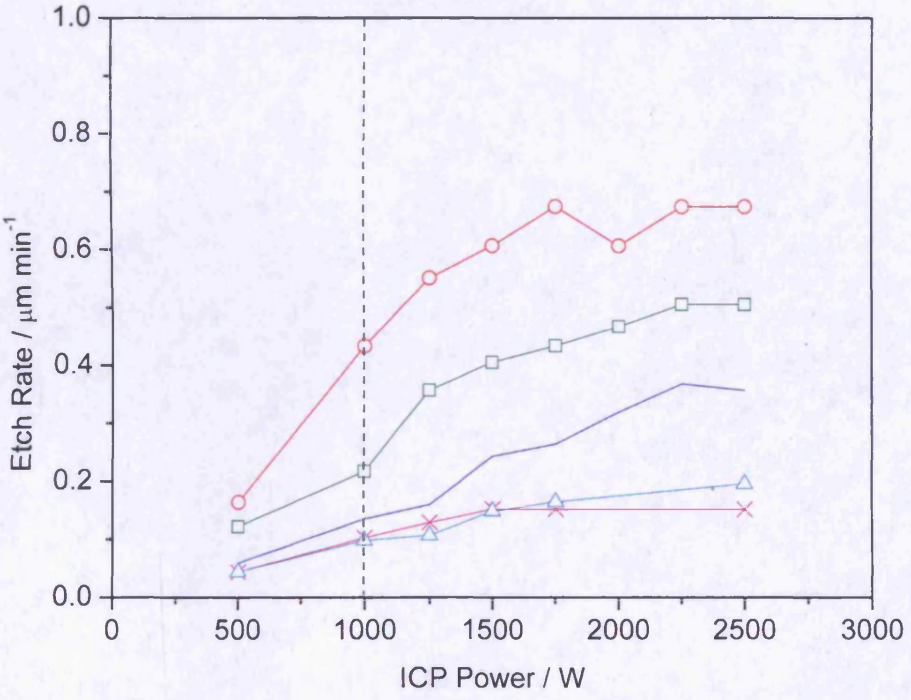

Figure 5.5 - Etch Rate as a function of ICP power for a range of temperatures: 20 °C (magenta crosses), 100 °C (cyan hollow triangles), 150 °C (blue filled squares), 170 °C (green hollow squares), and 190 °C (red hollow circles). (all other conditions as in Table 5.1, dashed vertical line shows the 'standard' conditions).

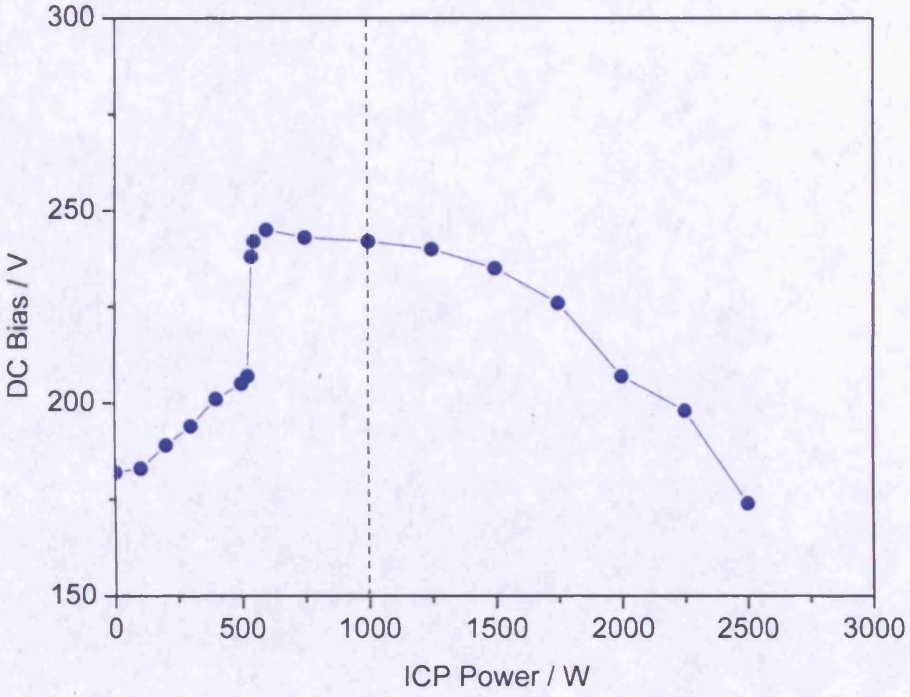

Figure 5.6 - DC Bias as a function of ICP Power at 190 °C (all other conditions as in Table 5.1, dashed vertical line shows the 'standard' conditions).

Figure 5.7 shows the etch rate of AlGaInP (reproduced from Figure 5.5) and SiO_2 as a function of ICP power at 190 °C. The selectivity as a function of ICP power at 190 °C is shown in Figure 5.8. It was not possible to take complete measurements for Ni because at higher ICP powers $NiCl_2$, the product of the Ni removal, is re-deposited on the sample and the chamber interior. The contamination causes a significant drop in selectivity. (In order to restore the chamber condition following contamination with this substance required repeated cleaning of the chamber interior with IPA and high power Ar plasma cleans. Successful decontamination restored etch rate and selectivity values to normal.) The dependence of the etch rate of SiO_2 is very different to that of AlGaInP. There is a linear increase in the etch rate of SiO_2 with increasing ICP power. This implies that etching of SiO_2 appears to be dominated by ion flux and is insensitive to ion energy. The resulting selectivity decreases with increased ICP power indicating that lower ICP powers are preferable for highly selective etching.

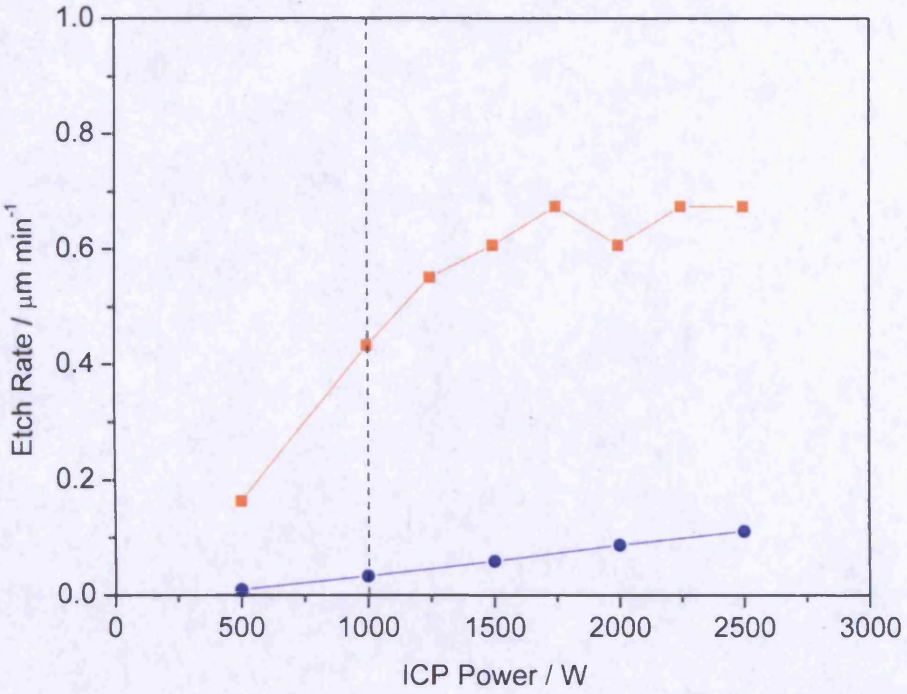

Figure 5.7 - Etch Rates of AlGaInP (orange squares) and SiO_2 (blue circles) as a function of ICP Power at 190 °C (all other conditions as in Table 5.1, dashed vertical line shows the 'standard' conditions). Ni data unavailable.

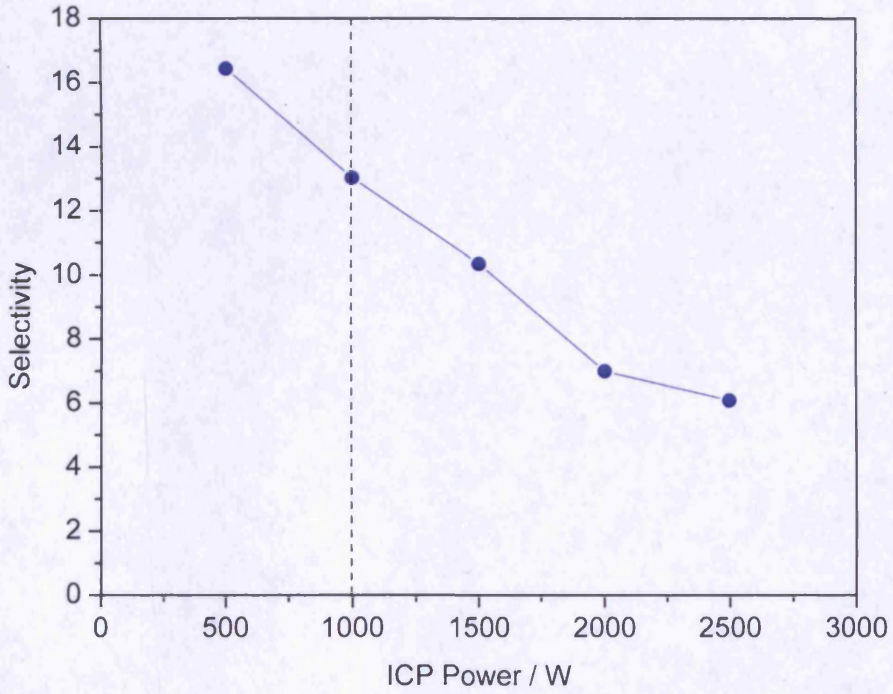

Figure 5.8 - Selectivity of the AlGaInP etch with respect to SiO_2 (blue circles) masks as a function of ICP power at 190 °C (all other conditions as in Table 5.1, dashed vertical line shows the 'standard' conditions). Ni data unavailable.

To investigate the effect of RIE power, an ICP power of 1000 W was chosen to compromise between selectivity and reasonable etch rate. A temperature of 190 °C was also chosen to achieve high etch rates and selectivity.

Figure 5.9 shows how etch rate of AlGaInP, SiO_2 and Ni varies as a function of RIE power. Figure 5.10 shows the DC bias as a function of RIE power. There is a slightly super-linear increase in the etch rate of AlGaInP with RIE power in this range. This is also true for results taken at 20 °C. There is a weaker, linear dependence of the SiO_2 etch rate. Since AlGaInP etching is sensitive to both DC bias (increases linearly with RIE power) and ion flux and SiO_2 etching is predominantly dependent on ion flux then a stronger dependence of the AlGaInP etch rate on RIE power than for the SiO_2 etch rate is expected. Consequently, the resulting selectivity, shown in Figure 5.11, increases as RIE power is increased indicating that higher RIE powers are preferable for highly selective etching.

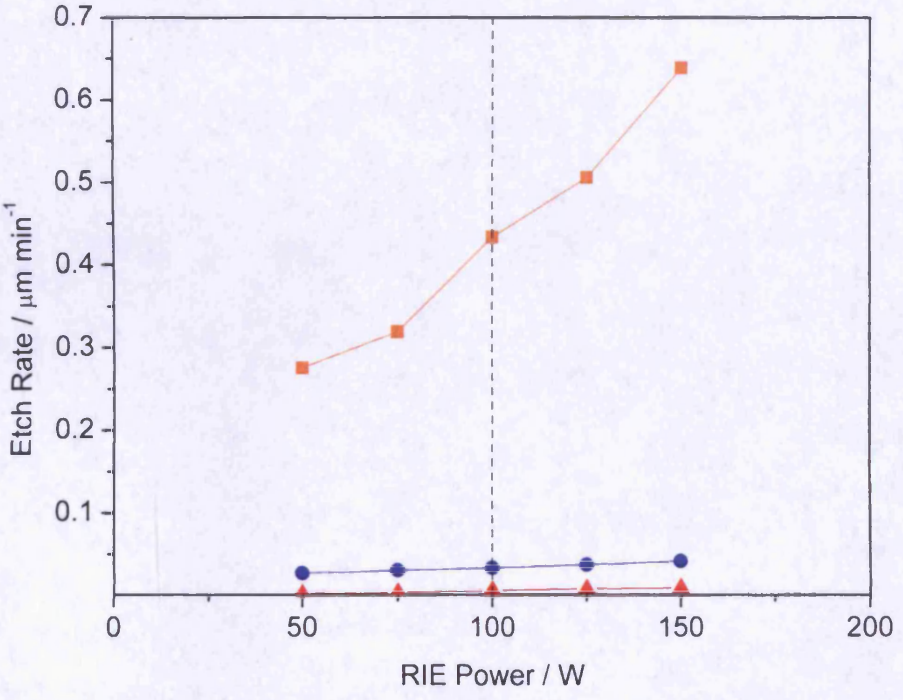

Figure 5.9 - Etch Rates of AlGaInP (orange squares), SiO_2 (blue circles) and Ni (red triangles) as a function of RIE Power at 190 °C (all other conditions as in Table 5.1, dashed vertical line shows the 'standard' conditions).

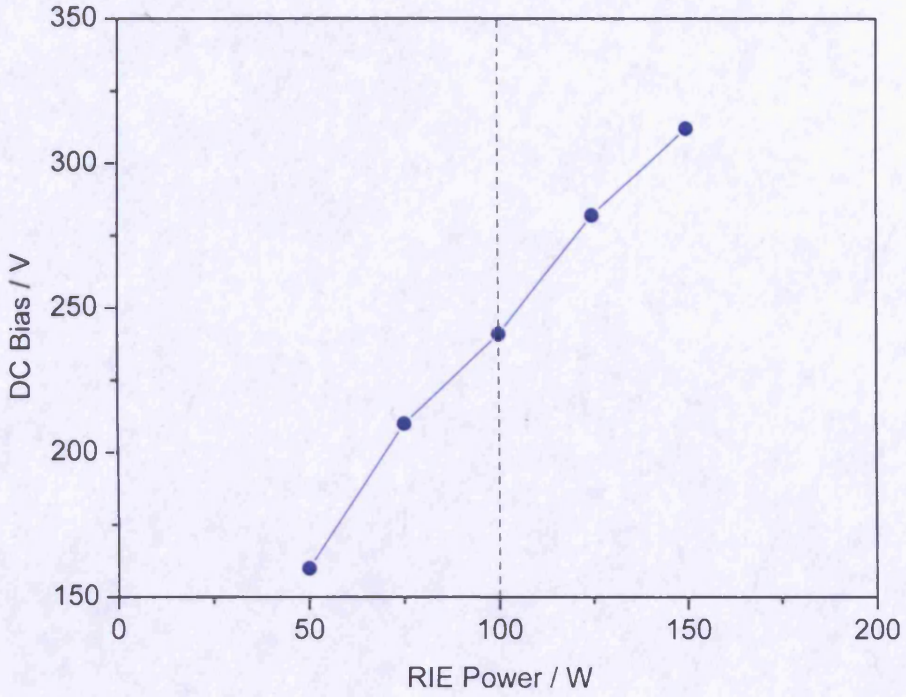

Figure 5.10 – DC Bias as a function of RIE Power at 190 °C (all other conditions as in Table 5.1, dashed vertical line shows the 'standard' conditions).

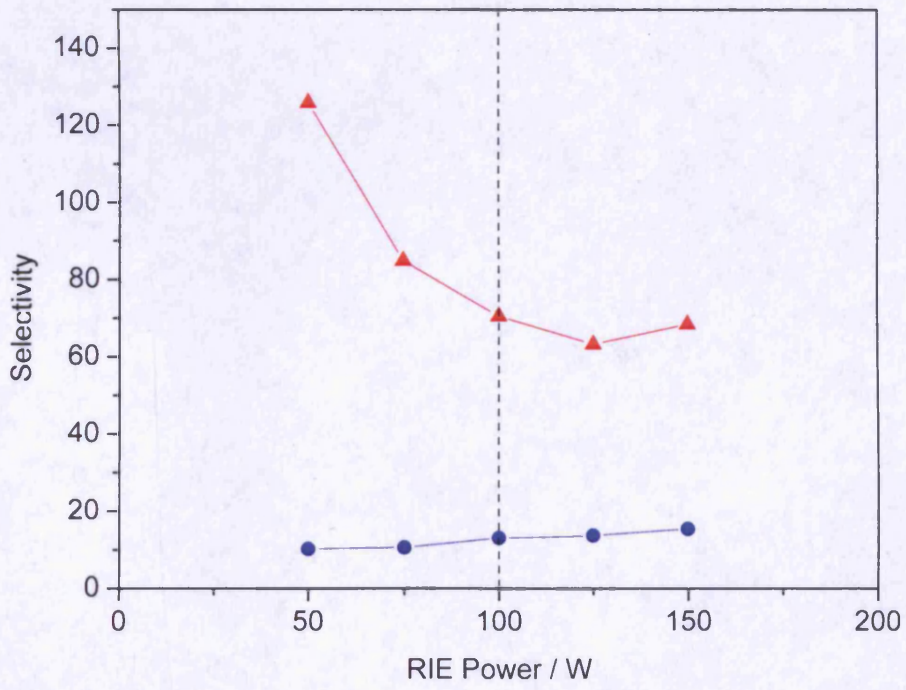

Figure 5.11 - Selectivity of the AlGaInP etch with respect to SiO_2 (blue circles), and Ni (red triangles) masks as a function of RIE power at 190 °C (all other conditions as in Table 5.1, dashed vertical line shows the 'standard' conditions).

5.4.3. Pressure dependence

The etch rate of AlGaInP shows a strong increase with decreasing chamber pressure. This is shown in Figure 5.12. The etch rate of both SiO_2 and Ni shows a functionally similar but weaker dependence on chamber pressure. The etch rate dependence for both AlGaInP and SiO_2 seems reasonable as collisions and recombination events within the plasma are expected to decrease the plasma density and ion flux. This would also be expected to result in an increase in DC bias and a small increase in DC bias of about 20V is observed, as shown in Figure 5.13.

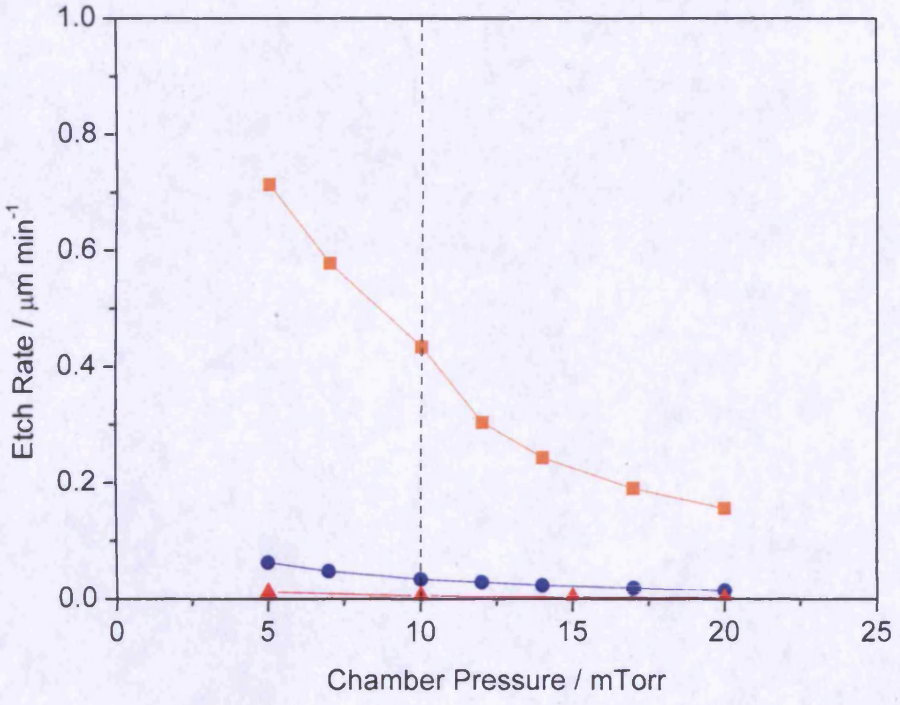

Figure 5.12 - Etch Rates of AlGaInP (orange squares), SiO_2 (blue circles) and Ni (red triangles) as a function of chamber pressure at 190 °C (all other conditions as in Table 5.1, dashed vertical line shows the 'standard' conditions).

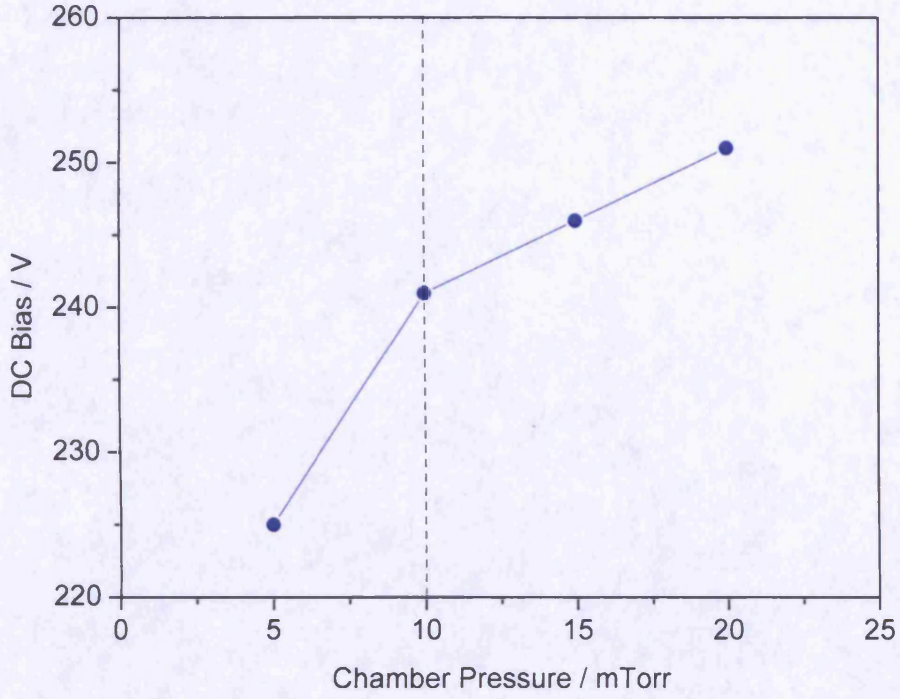

Figure 5.13 - DC Bias as a function of chamber pressure at 190 °C (all other conditions as in Table 5.1, dashed vertical line shows the 'standard' conditions).

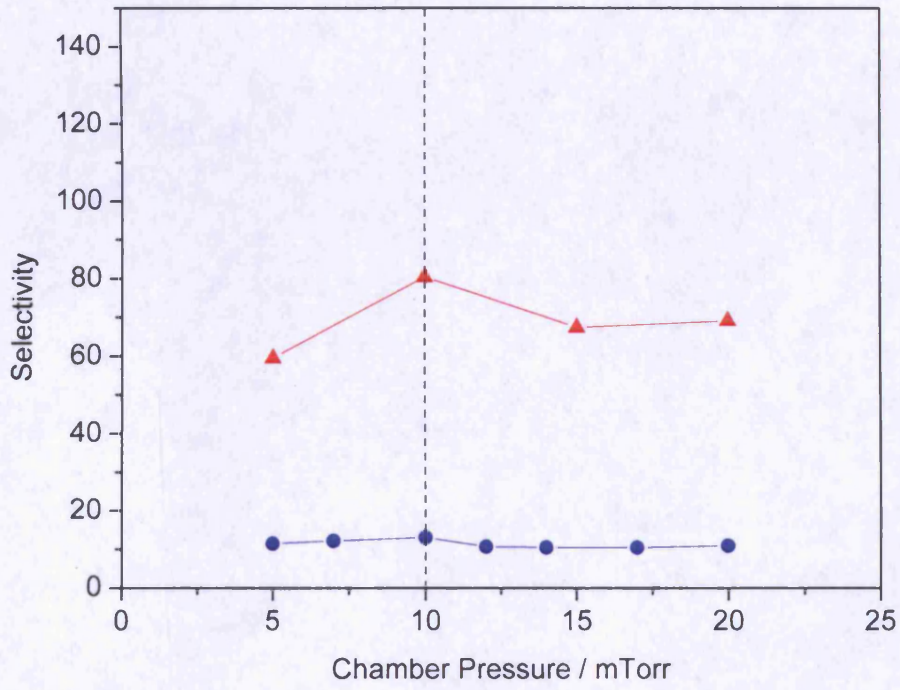

Figure 5.14 - Selectivity of the AlGaInP etch with respect to SiO_2 (blue circles), and Ni (red triangles) masks as a function of chamber pressure at 190 °C (all other conditions as in Table 5.1, dashed vertical line shows the 'standard' conditions).

As there is little change in DC bias, changes in ion flux are likely to be the dominant cause of changes in etch rate. As AlGaInP and SiO_2 etch rates are both dependent on ion flux we might expect to see similar dependences and no overall change in selectivity as chamber pressure is varied, as is observed. This agrees with the results shown by Hong et al. [46] who reported decreases in the etch rate of InGaP, AlInP and AlGaP in a planar ICP reactor with increased pressure but apparently contradicts Shul et al. [72] who saw a constant InP etch rate with pressure. However, Shul et al. reported a much larger increase in DC bias.

5.4.4. Chemistry dependence

The dependence of the etch rate of AlGaInP, SiO_2 and Ni at 190 °C on BCl_3/Cl_2 composition is shown in Figure 5.15. Total gas flow is kept at 40sccm and the gas composition is varied from pure BCl_3 to pure Cl_2. No Ar is added to the process gas. All other conditions are standard as given in Table 5.1. The etch rates of both AlGaInP and SiO_2 are lowest when there is no Cl_2 in the process gas. The etch rate rises to a maximum etch rate of 0.56 μm min^{-1} at ~85 % Cl_2 with no further increase to 100 % Cl_2. The DC bias decreases by ~15 V as the Cl_2 concentration increases from 0-100 % and so is not the cause of the increased etch rate. Similar behaviour has been reported in GaN etching [73,74] where etch rate was generally found to increase with Cl_2 concentration. These studies also reported increases in ion current density and amounts of Cl radicals with increased Cl_2 concentration. The etch rate of SiO_2 (at 190 °C) has a slightly weaker, linear dependence on Cl_2 concentration than the etch rate of AlGaInP. The resulting selectivity is weakly dependent on gas composition reaching a maximum of 17:1 at 85 % Cl_2. Although the Ni etch rate increased only very slightly as Cl_2 concentration the proportional increase was larger than that of SiO_2 resulting in selectivity that decreased with increased Cl_2 concentration.

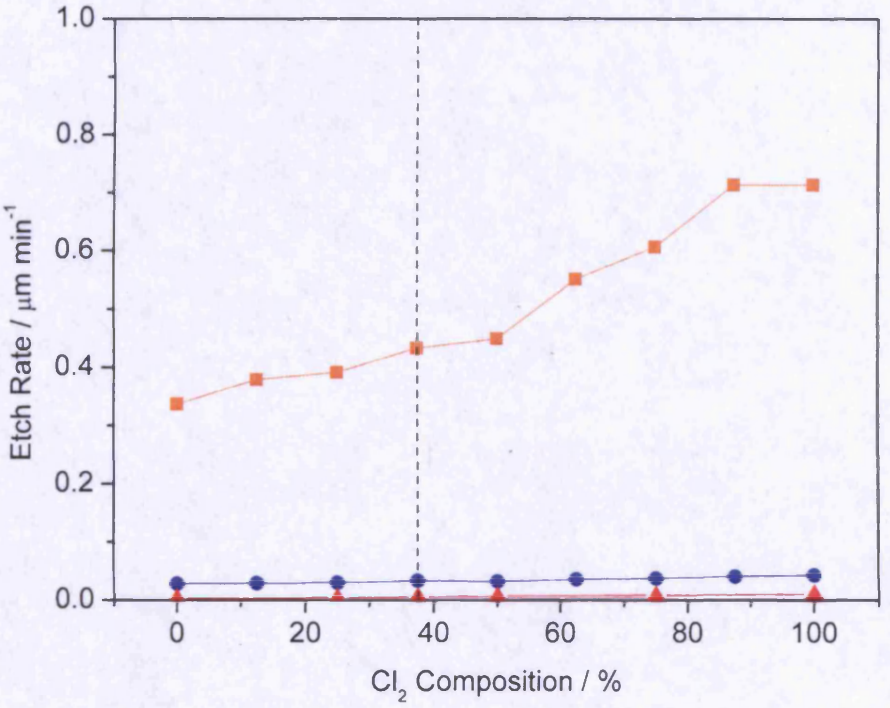

Figure 5.15 – Etch Rates of AlGaInP (orange squares), SiO_2 (blue circles) and Ni (red triangles) as a function of Cl_2 composition at 190 °C (all other conditions as in Table 5.1, dashed vertical line shows the 'standard' conditions).

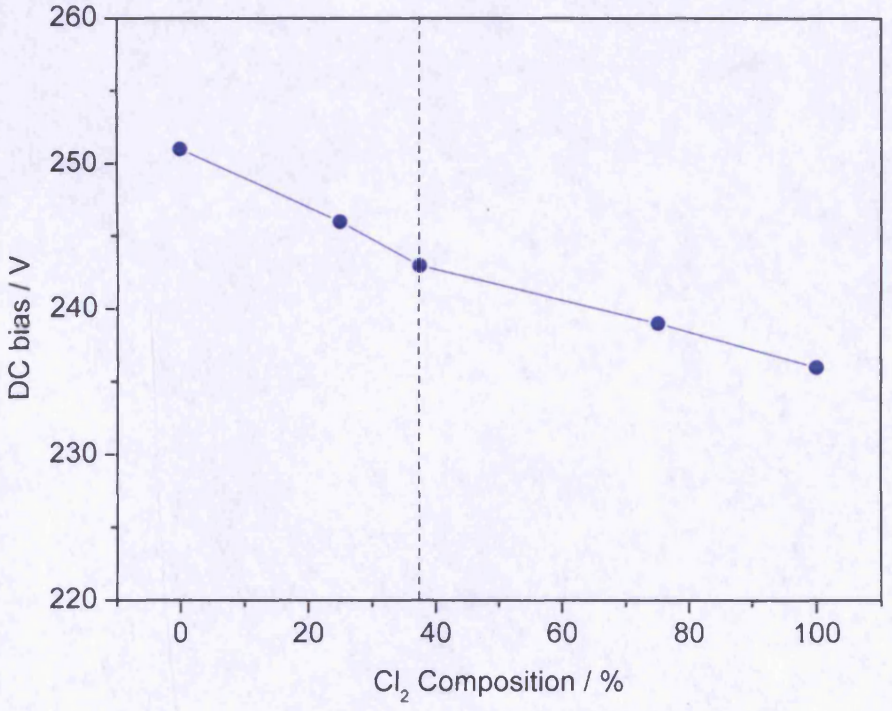

Figure 5.16 – DC Bias as a function of Cl_2 composition at 190 °C (all other conditions as in Table 5.1, dashed vertical line shows the 'standard' conditions).

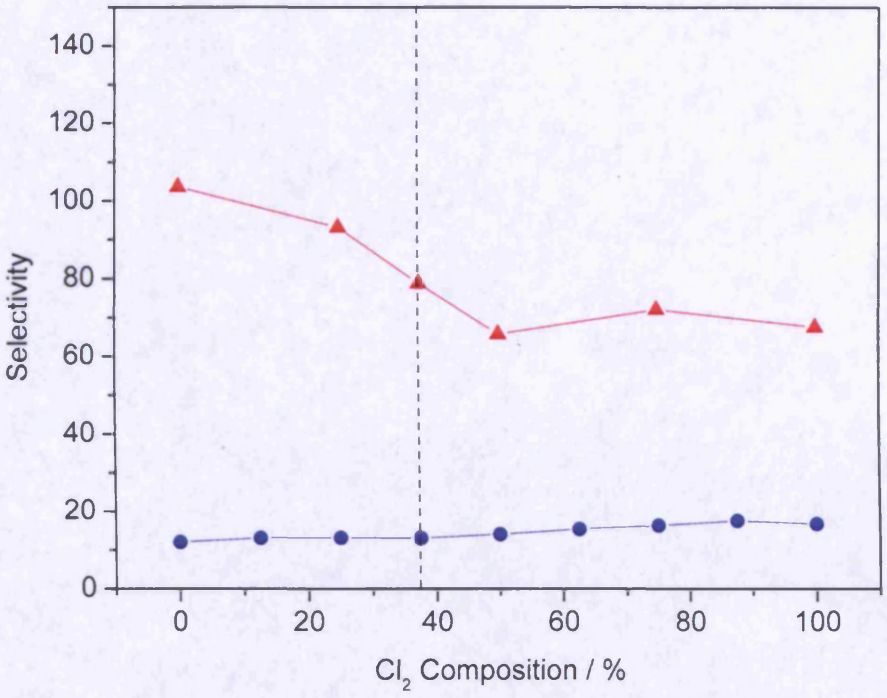

Figure 5.17 - Selectivity of the AlGaInP etch with respect to SiO_2 (blue circles), and Ni (red triangles) masks as a function of Cl_2 composition at 190 °C (all other conditions as in Table 5.1, dashed vertical line shows the 'standard' conditions).

The addition of Ar to either Cl_2 or BCl_3 has been suggested as a means to increase the etch rate of In-containing materials as an alternative to raising the temperature. Figure 5.18 shows that at 20 °C there is an increase in etch rate of AlGaInP with increasing Ar concentration to a maximum at around 70 % then a sharp decrease as the concentration increases further. This is similar behaviour to that observed by Hong et al. [46] in a planar ICP reactor for Cl_2/Ar or BCl_3/Ar chemistries when etching GaInP, AlInP and AlGaP. Here, the total gas flow is kept at 40sccm and the relative amounts of BCl_3 and Cl_2 are not varied. The enhancement reported here is a factor ~1.35 increase, much smaller than the factor ~5 and ~8 increases in reference 46 for Cl_2 and BCl_3 respectively. The origin of these differences is unclear; they may relate to the differences in reactor design. If the rate is limited by removal of $InCl_3$ this result suggests that the presence of Ar (i.e. sputtering by Ar ions) aids removal. At Ar concentrations above 70 % it appears the amount of reactive species is limiting the etch rate. Similar behaviour is observed when etching SiO_2 resulting in a selectivity of ~3:1 that does not change significantly with Ar concentration. It is clear that at room temperature the addition of Ar does not lead to the enhancement in selectivity achieved by elevating the sample temperature. However, when the sample temperature is raised

to 190 °C there is a marked difference in behaviour. The etch rate dependence has a similar form to the low-temperature Ar fraction dependence but there is a large enhancement to the peak which rises to a sharp peak value at ~80 % of (0.85±0.05) μm min^{-1}. This in turn results in a selectivity that rises to a peak value of ~125:1. There is some uncertainty about how well the sample temperature is controlled in the experimental set ups of references 41-46 so it is possible that the enhancements observed were not just ion-assisted but in fact a combined effect of increased thermally-assisted and ion-assisted desorption.

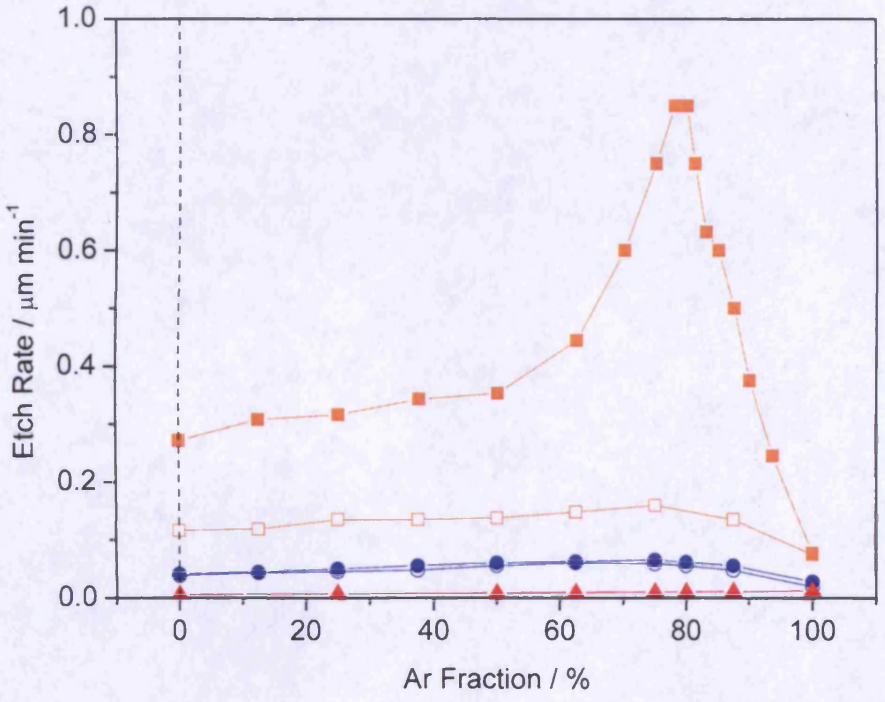

Figure 5.18 - Etch Rates of AlGaInP (orange squares), SiO_2 (blue circles) and Ni (red triangles) as a function of Ar fraction at 190°C (solid symbols) and 20 °C (hollow symbols) (all other conditions as in Table 5.1, dashed vertical line shows the 'standard' conditions).

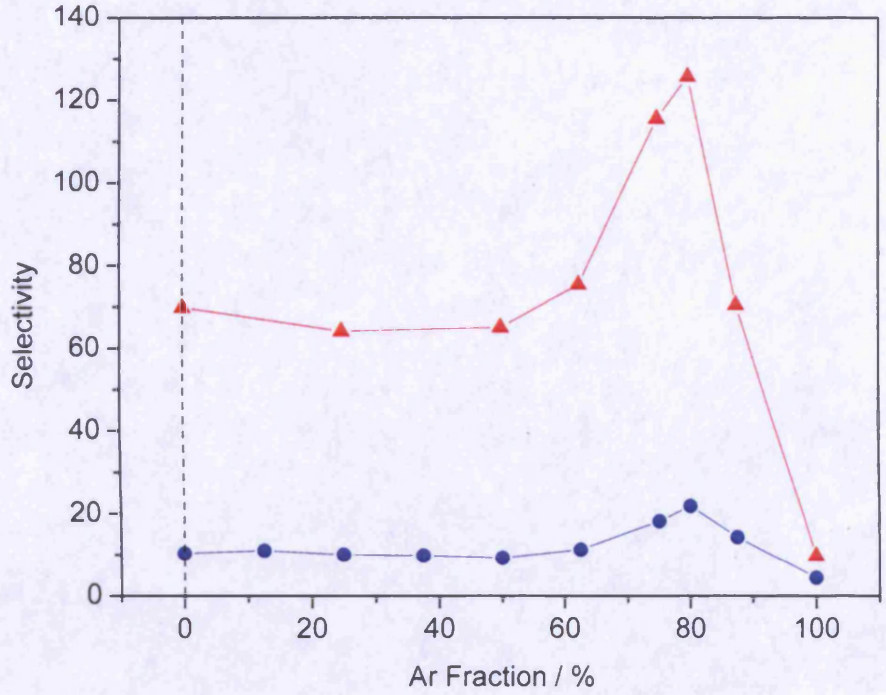

Figure 5.19 - Selectivity of the AlGaInP etch with respect to SiO_2 (blue circles), and Ni (red triangles) masks as a function of Ar fraction at 190°C (all other conditions as in Table 5.1, dashed vertical line shows the 'standard' conditions).

5.4.5. Conclusions of selectivity study

The aim of this study was to characterise the etching of AlGaInP in a BCl_3/Cl_2 environment and determine the conditions required for achieving reasonable etch rates while maintaining the selectively, with respect to SiO_2 and Ni masks, necessary for etching high-aspect-ratio features.

The greatest enhancement in phosphide etch rate was achieved by raising the sample temperature from room temperature up to 190 °C. Since SiO_2 and Ni etching is largely temperature insensitive this also produced the largest enhancement in selectivity. At 190 °C an AlGaInP etch rate up to 0.7 μm min^{-1} and selectivity, with respect to SiO_2, as high as 17:1 was achieved. Selectivity with respect to Ni was as high as 70:1 under the same conditions. This was a far greater enhancement than produced by changing any other parameter alone. However, there is a requirement for thermal contact between sample and carrier, over the required process time, which places an upper limit on the available temperature range. With Fomblin oil, a temperature of 190 °C is close to this limit since the oil evaporates leading to loss of thermal contact and thermal runaway. As the

AlGaInP etch rate and the selectivity obtained at below 190 °C are sufficient for the etch depths required this effect should not be a problem here.

A consequence of the temperature sensitivity of the AlGaInP etch rate at elevated temperature is that it is almost certain to increase during the etching of deep structures. Real-time measurement of etch rate allows this effect to be monitored and gives better control of etch depth.

In contrast to what has been seen in other reactors, the addition of Ar to the gas mix produces relatively minor changes at room temperature in both etch rate and selectivity and is therefore unsuitable in isolation for this application. Changing the Cl_2:BCl_3 ratio similarly produces relatively minor changes. However, the addition of Ar at 180 °C resulted in significant enhancement to the etch rate. This seems to be the combined effect of increased thermally-assisted and ion-assisted desorption of $InCl_3$.

The power and pressure dependent results can be understood by considering that the AlGaInP etch rate is strongly dependent on both DC bias and ion flux while for SiO_2 it is strongly dependent on flux but not DC bias. This is consistent with the ion energy being important in the removal of $InCl_3$ but being much less important in the formation of etch products with SiO_2. These observations are also consistent with the observation that the selectivity is improved by increasing the RIE power at the expense of ICP power.

5.5. Comparison of mask materials

Ni was found to have a much lower etch rate than SiO_2 and therefore a correspondingly higher AlGaInP selectivity. Perhaps more importantly, the horizontal component of the SiO_2 etch rate was significantly higher than that of Ni. This led to rough edges and angled sidewalls even under conditions where vertical etching was observed when using a Ni mask. This is shown in Figure 5.20, where the plasma conditions would ordinarily produce a highly anisotropic feature.

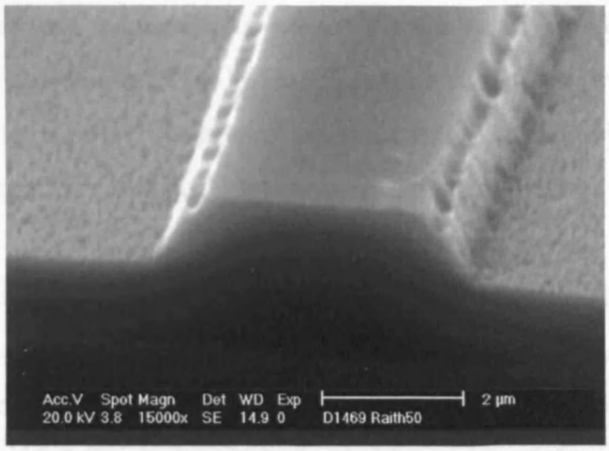

Figure 5.20. Scanning electron micrograph of a 4 µm ridge etched with a SiO2 mask, BCl3:Cl2 ratio kept at 25:15 and total gas flow kept at 40 sccm. 32sccm (80%) Ar gas flow, 1000 W ICP, 100 W RIE and 10 mTorr chamber pressure at 180 °C.

For the purposes of this project in the reactor type and etch chemistry available it is therefore obvious that SiO_2 is an unsuitable mask material and therefore further studies were restricted to using only Ni masks.

An etch rate and selectivity study was carried out to determine conditions suitable for etching SiO_2 for mask preparation. However, as SiO_2 is unsuitable for masking in the fabrication of photonic structures, details of the findings of this study are not included here.

5.6. Vertical etching study experimental details

This work builds upon the previous study of the selective etching of AlGaInP in BCl_3/Cl_2 inductively coupled plasmas (ICP) [Section 5.4] that highlighted the importance of elevated process temperatures in order to remove involatile, and therefore passivating $InCl_3$ [39,40]. Here, a BCl_3/Cl_2/Ar gas chemistry has been employed, on the basis that as the percentage of Ar in the mix is increased the physical effects of the etch will increase at the expense of the chemical and allow the optimum conditions to be identified. A potential major complication of this study is that it proved essential to retain a GaAs cap layer above the AlGaInP (see experimental details below). Etching of GaAs in Cl_2/Ar was not thought to involve a passivant but anisotropic etching of such structures has been achieved using Cl_2/Ar ECR-RIE plasmas containing ~90 % Ar, as described by Avary et al. [75]. The mechanism for etching anisotropically in this process was described by Hu et al. to result from dilution of the active neutral species

by inert Ar which leaves the lateral etch rate of the GaAs a relatively small fraction of the ion-assisted vertical etch rate [76]. Therefore, although it is possible that the BCl_3 present in the gases used in this study may act as a passivant [62,63], it is to be expected that the GaAs will etch in a very different manner to the underlying AlGaInP.

The results of Section 5.4.4 show that at elevated temperature there is a significant AlGaInP etch rate enhancement when the amount of Ar introduced into the plasma is optimum. It seems reasonable to expect that this variable has a strong influence on the degree of anisotropy of the etch, particularly as this parameter has a large effect on the relative amounts of chemical and physical etching. It was therefore decided to look at the effects on sidewall profile of varying the Ar fraction present in the plasma.

The laser structures etched in this study were grown by MOCVD and lattice matched to GaAs. They consist of a ~0.25 μm $(Al_{0.3}Ga_{0.7})_{0.51}In_{0.49}P$ waveguide core within ~1 μm $(Al_{0.7}Ga_{0.3})_{0.51}In_{0.49}P$ cladding layers. The waveguide contains two ~5 nm $Ga_{0.41}In_{0.59}P$ quantum wells. The structure is topped with a ~10 nm $Ga_{0.51}In_{0.49}P$ interface layer and finally a ~0.5 μm GaAs cap layer. The layer structure is ~2.7 μm thick in total.

The process was developed firstly using 4 μm wide, 300 μm pitch ridges that were etched to allow an accurate evaluation of the sidewall profile and post-etch surface morphology. For consistency, these were always etched to a depth of 1.5 μm. The results of these measurements were then used to determine a process for etching sub-micron features. Apart from the lithography steps, the fabrication processes prior to etching for sub-micron features was identical to the ridge fabrication process. Ni was used as the mask material in preference to the SiO_2 used in the previous study [Section 5.4] due to its much lower vertical and horizontal etch rates.

The 4 μm wide ridges were defined by optical lithography using a two layer resist comprising S1813 SP15 photoresist on Brewer Science WiDE8 EXP04002 lift-off resist. Development was carried out in Brewer Science PSC developer for 3 minutes followed by a 3 minute de-ionised water rinse.

Sub-micron features were patterned in polymethylmethacrylate (PMMA) 950k spun on to a thickness of ~200 nm. Patterns were defined in a Raith50 electron beam lithography

system at 20 keV. However, such lithography of ~0.1 micron features requires the presence of a highly conductive layer under the electron beam resist in order to minimise charging effects. To achieve this it proved necessary to retain the GaAs cap layer which is much more conductive than the underlying AlGaInP. Development was carried out in a methyl isobutyl ketone (MIBK)/isopropyl alcohol (IPA) solution for 30 s followed by a 30 s IPA rinse. Scanning electron micrographs of sub-micron features patterned in PMMA are shown in Figure 5.21.

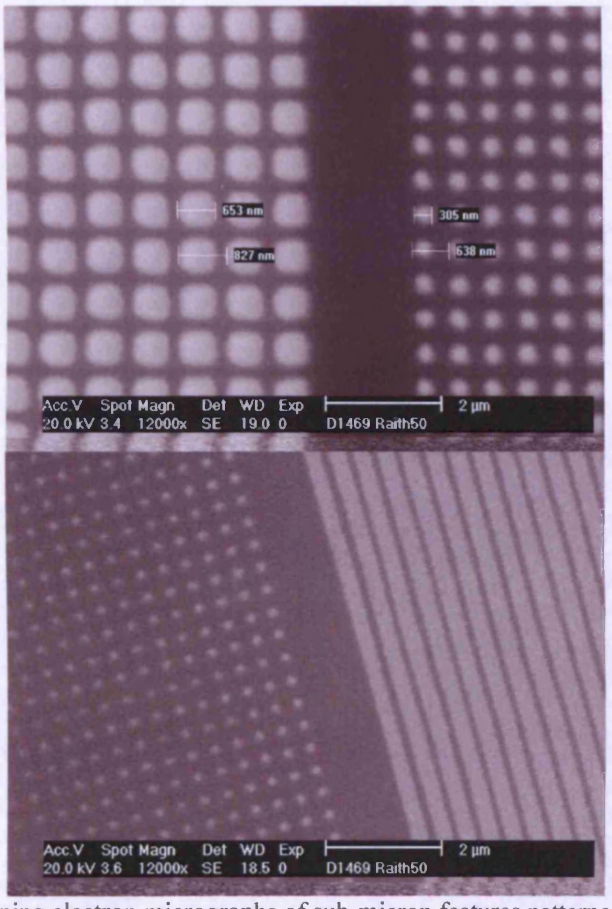

Figure 5.21 – Scanning electron micrographs of sub-micron features patterned by electron beam lithography in PMMA.

For both ridges and sub-micron features thermally evaporated Ni masks, typically ~60nm thick, were defined following lithography via a lift-off process with high quality pattern reproduction. A scanning electron micrograph of a typical sub-micron pattern is shown in Figure 5.22.

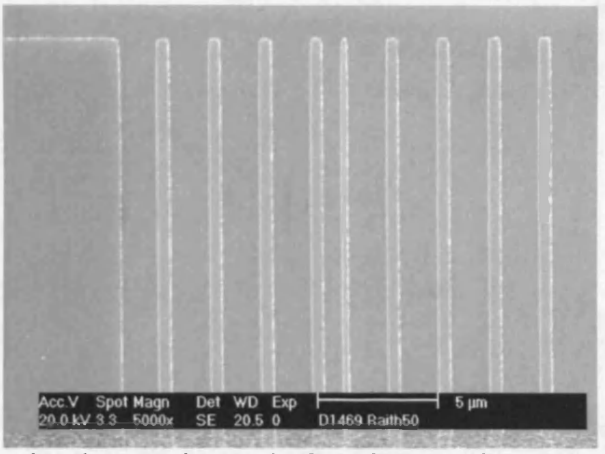

Figure 5.22 – Scanning electron micrograph of a typical sub-micron pattern after Ni lift-off.

Etching was carried out in an Oxford Instruments Plasmalab System 100 with ICP 380. Si wafers were used as carriers for the ~8×8 mm AlGaInP test samples used in this study. Samples were mounted with Fomblin oil to establish a better thermal contact and therefore better control of sample temperature, which is measured at the sample stage. The maximum sample temperature used here was 180 °C; at temperatures above ~180 °C evaporation of the Fomblin oil leads to difficulties in maintaining thermal contact between sample and carrier wafer in the time scale of the etch process.

The system was equipped with a normal incidence laser interferometry unit operating at 677.4 nm, which was used to determine the etch rates and to endpoint. This system also allowed the time-dependent etch rate to be monitored based on the technique describe by Hayes et al [68]. This technique is particularly useful when etching AlGaInP in Cl-based chemistries due to the highly temperature, and consequently time, dependent etch rate [Section 5.4]. Etch rates were measured between the ridges by laser interferometry over 2 periods of oscillation with a Rayleigh mean taken of the maxima and minima to establish the period of oscillation. An average refractive index value of 3.35 and laser wavelength of 677.4 nm were used. The technique used to measure etch rate allowed a large number of measurements to be made in quick succession on one sample. In contrast, each measurement of RMS roughness and sidewall profile has to be done on a separate sample. Consequently there are inevitably fewer data points for these measurements. Post-etch surface roughness measurements were performed on the samples using a Digital Instruments Nanoscope IIIa multimode atomic force microscope (AFM) over a 10 × 10 μm scan area located centrally between the ridges.

Measurements of feature dimensions were made using the Phillips XL scanning electron microscope (SEM) that forms part of the Raith50 lithography system. Samples were cleaved across the etched features and mounted on angled copper blocks at 15° to the vertical to allow the sidewall profile to be imaged. The system allows measurement of linear dimensions to assess the sidewall profile.

As previously considered, the etch process needs to produce vertical sidewalls in the GaAs cap as well as the AlGaInP growth layers. Since the etch rate of GaAs is much higher than that of AlGaInP (in BCl_3/Cl_2) a 2-step etch procedure was developed. The GaAs cap layers were etched at 25 °C with 300 W ICP power and 50 W RIE power based on conditions obtained in a separate GaAs/AlGaAs etch study. The sample was then moved to the load-lock and kept under vacuum while the stage temperature was increased to 180 °C, the temperature at which the AlGaInP layers were etched. 1000 W ICP power and 100 W RIE power were used to etch the AlGaInP layers. For both steps of the etch process the chamber pressure was kept at 10 mTorr, the ratio of BCl_3:Cl_2 was kept at a constant 25:15 and a He backing pressure of 10 Torr was used. These values were chosen to enable direct comparison with previous results [Section 5.4]. The fraction of Ar added to the BCl_3/Cl_2 process gas was varied from 0-100 % and the sidewall angle, etch rate and RMS roughness measured as a function of Ar content.

5.7. Vertical etching study results

The results of the etch study are split into sections. Firstly, the effect of adding Ar on the sidewall profile will be discussed in terms of the different etching mechanisms described earlier. Then the correspondence with the vertical etch rate and RMS surface roughness measurements of the horizontal surface will be examined. Finally, the fabrication of sub-micron gratings using the developed process will be described.

5.7.1. Ar content dependence of ridge sidewall profile

Cross-sectional SEM images of the etched features from selected samples are shown in Figure 5.23. Several problems are encountered when etching AlGaInP based active device structures in BCl_3/Cl_2 alone. The profile of such an etch can be seen in Figure 5.23(a). The first thing to note is that the GaAs and AlGaInP layers etch in very

different ways. The AlGaInP sidewall is not vertical, it has a positive profile, and its edge is jagged. Closer inspection reveals the mask edge has not receded during the etch and it is straight. This means that the sidewall angle is not a result of linewidth loss mechanisms such as an angled mask sidewall profile or faceting of the mask and the jagged edge is not a reproduction of the mask but rather the profile is consistent with passivation of the surface. Another feature of the etch profile is that the GaAs cap layer has been severely undercut, by over 1μm each side, leaving much of the Ni mask free-standing. For clarity an expanded view is shown in Figure 5.24. This undercutting is apparent not only in the cross section of the ridge but also on the top surface of the ridge due to sagging of Ni where it is no longer supported. This is consistent with a lack of passivation, resulting in strongly isotropic chemical etching of GaAs [76].

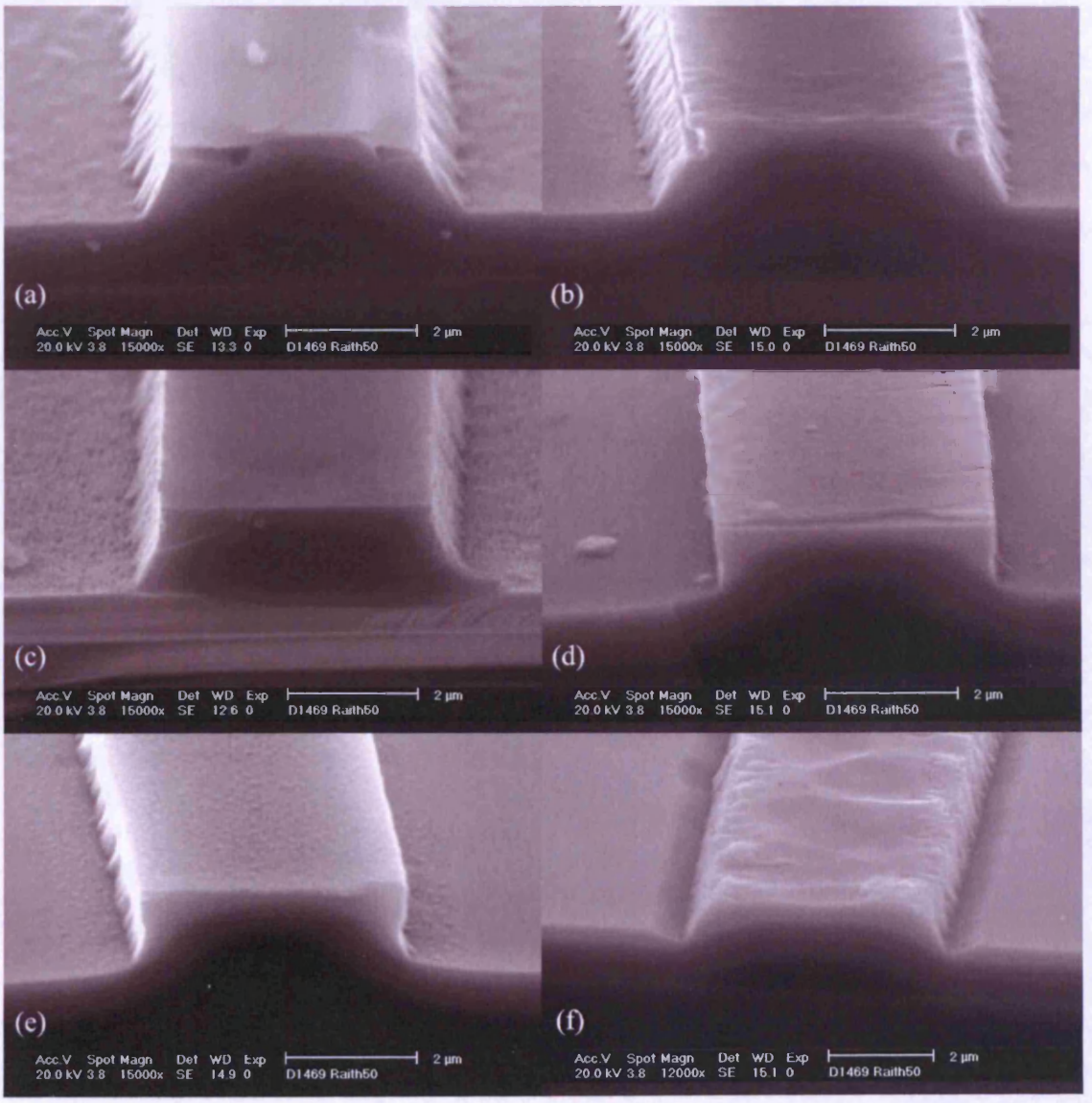

Figure 5.23 Scanning electron micrograph of a 4μm ridges etched with a Ni mask, 25:15 BCl3:Cl2, 1000 W ICP, 100 W RIE and 10 mTorr chamber pressure at 180 °C with (a) 0%, (b) 40%, (c) 75%, (d) 85%, (e) 90% and (f) 100% Ar. Total gas flow is kept at 40 sccm.

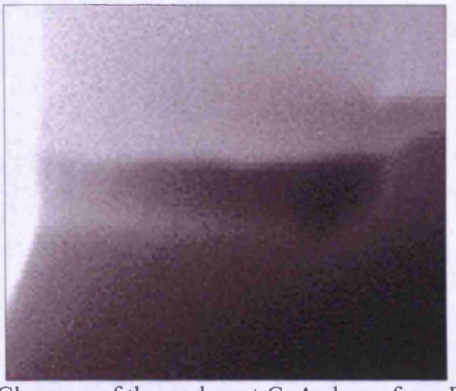

Figure 5.24 – Close-up of the undercut GaAs layer from Figure 5.23(a).

At 40 % Ar fraction (Figure 5.23(b)) the severe undercut seen in Figure 5.23(a) is evident but greatly reduced. However, the sidewall profile of the AlGaInP layers is still significantly jagged and angled. With 75 % Ar (Figure 5.23(c)) the GaAs undercut has been completely eliminated. However, there is still a significant though less pronounced sidewall roughness and an angled sidewall on the AlGaInP layers. At 85% Ar Figure 5.23(d) shows a near-vertical etch profile whilst at 90% Ar Figure 5.23(e) shows slight undercutting of the AlGaInP. At 100% Ar (Figure 5.23(f)) it is clear that that the etch selectivity has reduced such that the Ni mask has etched through, exposing the underlying semiconductor layers.

These observations are consistent with the models of the etch process described earlier. As the Ar fraction is increased and the etch became more physical, the unpassivated GaAs cap directly underneath the Ni mask etched more anisotropically, acquired a vertical sidewall somewhere between 40 % and 75 % Ar and remained vertical whilst the mask remained intact. By contrast the AlGaInP showed clear evidence of $InCl_3$ passivation having a positive sidewall profile at low Ar concentrations and slight undercutting (negative sidewall profile) indicative of passivant removal and chemical, isotropic etching at 90 % Ar. Additional measurements showed that there is a relatively narrow range of Ar fractions, between 80 % and 85 % Ar, in which AlGaInP etches vertically. It is curious that the AlGaInP appears to exhibit chemical undercutting at Ar concentrations that produce vertical sidewalls in GaAs. This may be due to differences between GaAs and AlGaInP or may be a consequence of the protection afforded to the thin GaAs cap by the Ni mask immediately above it.

Since vertical sidewalls are expected when sufficient $InCl_3$ passivant has been removed it should be noted that this will depend not only on the Ar fraction but other etch conditions as well. For example, increasing or decreasing the sample temperature would be expected to result in enhanced or inhibited removal of $InCl_3$. This has been illustrated by etching a 4μm ridge with 85 % Ar at 25 °C. Figure 5.25 shows that the reduced evaporation of passivant results in a return to a positive sidewall profile as expected. The post-etch surface roughness under these conditions is ~1 nm (Figure 5.26).

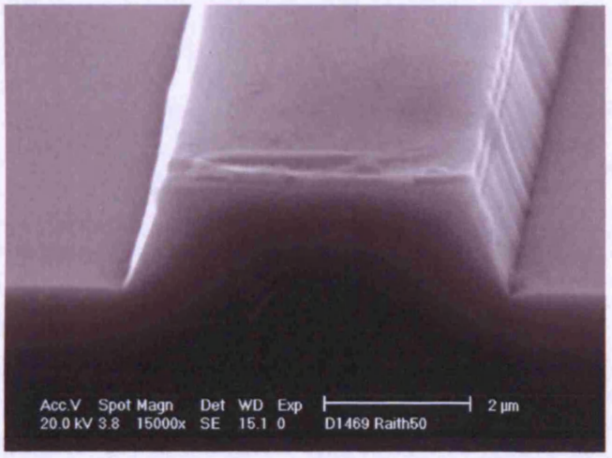

Figure 5.25 - Scanning electron micrograph of a 4 μm ridge etched with a Ni mask, BCl3:Cl2 ratio kept at 25:15 and total gas flow kept at 40 sccm. 34sccm (85%) Ar gas flow, 1000 W ICP, 100 W RIE and 10 mTorr chamber pressure at 25 °C.

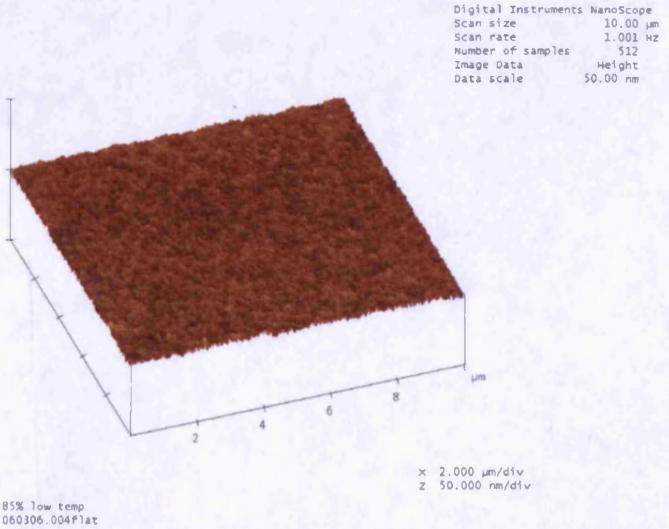

Figure 5.26 – AFM scan of a sample etched to the centre of the active region. BCl3:Cl2 ratio kept at 25:15 and total gas flow kept at 40 sccm. 34sccm (85%) Ar gas flow, 1000 W ICP, 100 W RIE and 10 mTorr chamber pressure at 25 °C*.

* Thanks to Henje Simmonds for assistance taking AFM scans

5.7.2. Discussion

Having established the general principle and a specific range of conditions for obtaining vertical sidewall features other properties of the etch process will now be considered, specifically how the etch rates (both GaAs and AlGaInP) and post-etch RMS surface roughness (of the surfaces etched by 1.5 μm) varied with Ar content. The stabilized DC bias was also measured as a function of Ar fraction. These results are shown in Figure 5.27. The AFM scans used to measure the RMS roughness are shown in Figure 5.28 for illustrative purposes.

For GaAs the etch rate approximately doubles on increasing the Ar content from 0% to 75% where it reaches its maximum observed value of (1.00±0.07) μm min^{-1} although the true maximum is likely to occur somewhere between the measured points. In our reactor, the measured DC bias decreases with increased Ar fraction as shown in Figure 5.27. This indicates an increased overall ion flux as well as the increase in the amount of inert Ar. Above 75% the etch rate decreases rapidly to a very low rate corresponding to Ar ion sputtering. This behaviour indicates the highly chemical nature of the etch due to the presence of chlorine and can be compared to the previous study of Pearton et al [77] who used a Cl_2/Ar gas mix and observed that the GaAs etch rate remained constant up to 40% Ar and then decreased increasingly rapidly. It is not clear what the origin of the difference between the results of Pearton's study and this is, although it is noted that Pearton's study was carried out in a reactive ion etcher (RIE) with a simpler gas mix and with a constant DC bias rather than constant RF powers.

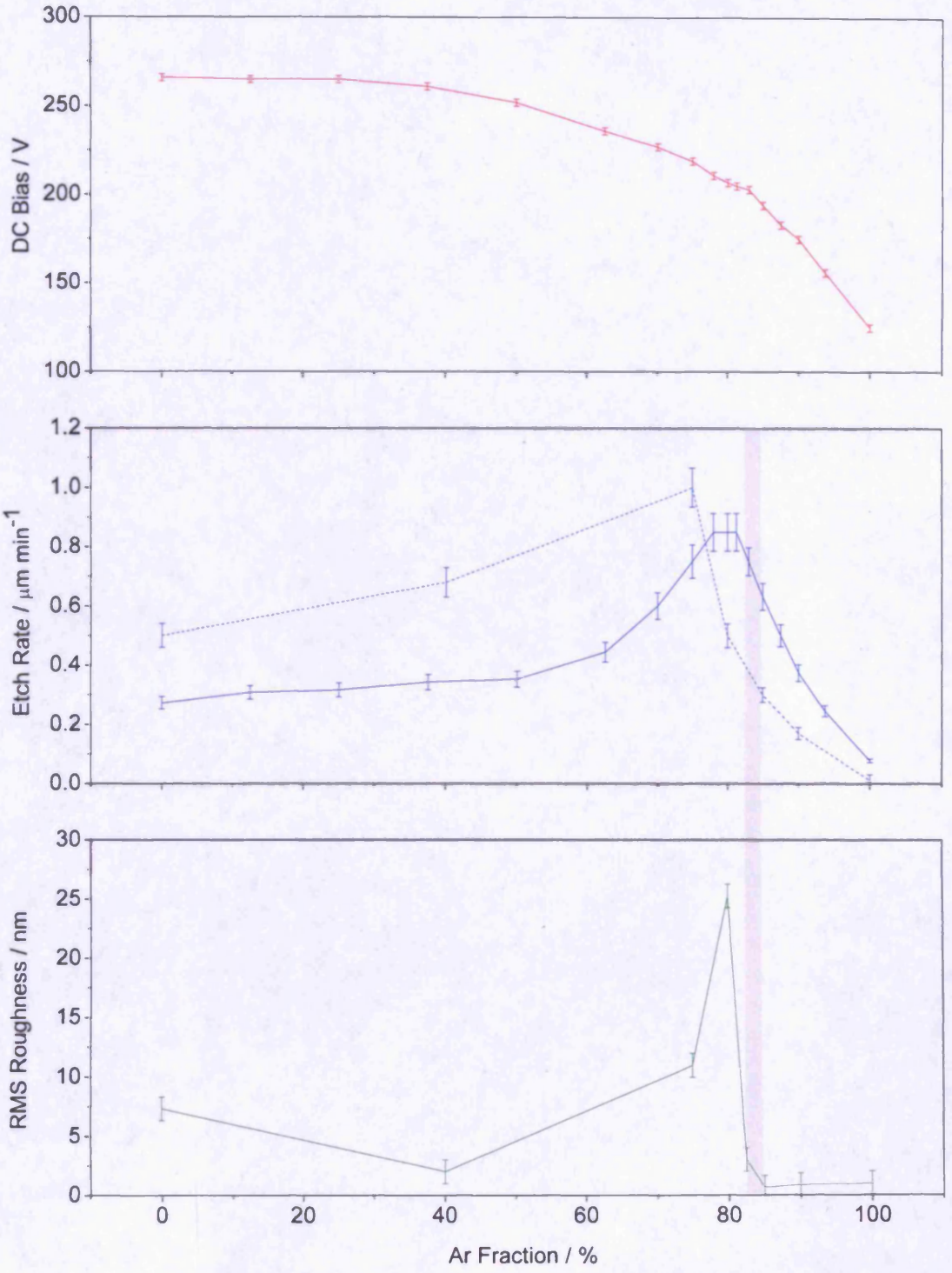

Figure 5.27 - Variation of DC Bias (red solid line), post-etch RMS roughness (green solid line) and Etch rate for GaAs (blue dashed line) and AlGaInP (blue solid line) as a function of Ar content. GaAs was etched with 300W ICP, 50W RIE at 25 °C and AlGaInP was etched with 1000 W ICP, 100 W RIE at 180 °C. The BCl3:Cl2 ratio was kept at 25:15 and chamber pressure was 10 mTorr. The range over which vertical features are produced in both GaAs and AlGaInP with high etch rate and low post-etch roughness is highlighted with the grey bar. The technique used to measure AlGaInP etch rate has allowed more data points to be measured than would be in a conventional etch study.

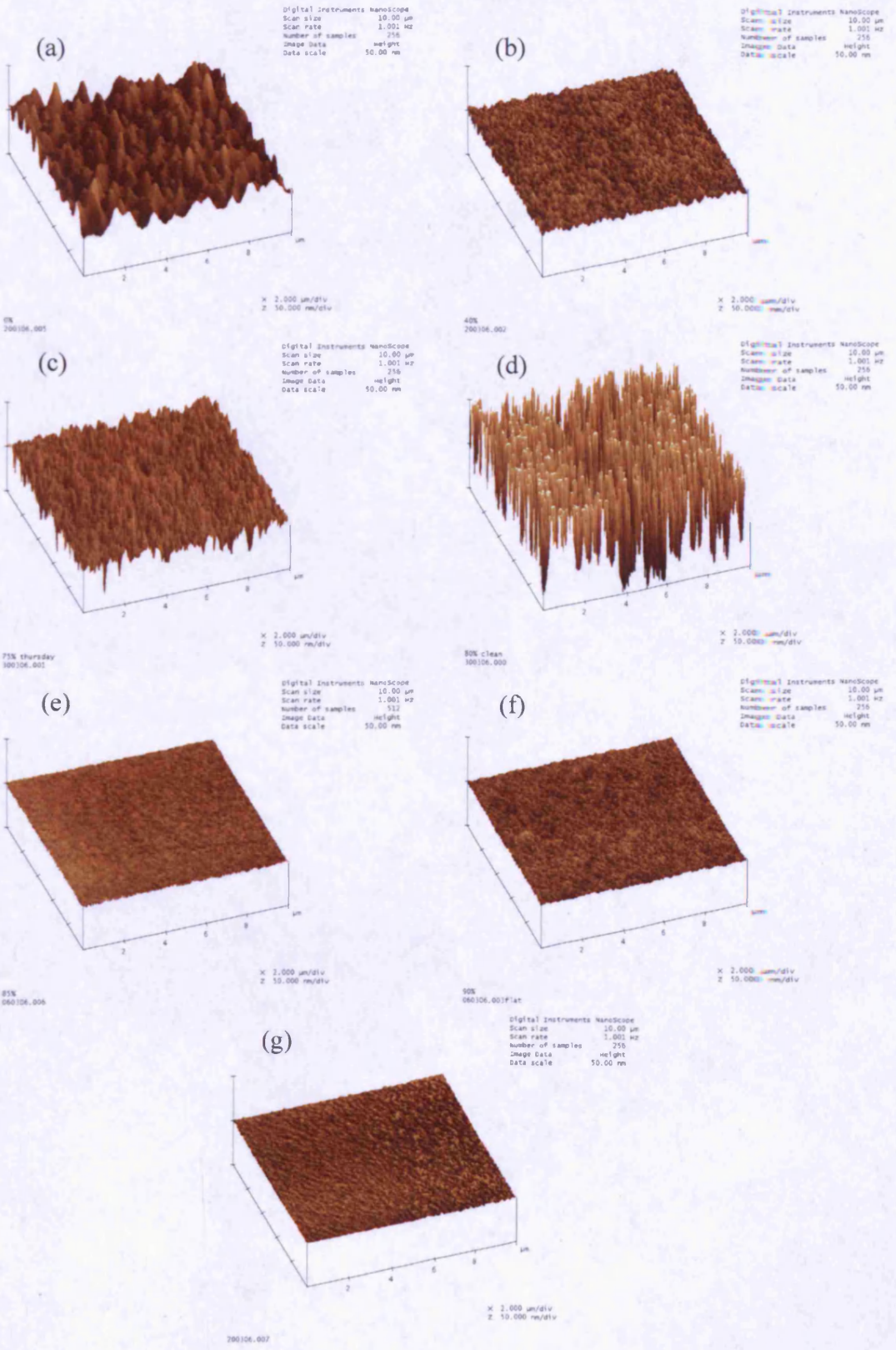

Figure 5.28 – AFM scans of samples etched to the centre of the active region with a BCl3/Cl2/Ar plasma containing (a) 0%, (b) 40%, (c) 75%, (d) 80%, (e) 85%, (f) 90% and (g) 100% Ar at 180 °C*.

* Thanks to Henje Simmonds for assistance taking AFM scans

For AlGaInP the etch rate was approximately constant up to 50% Ar from which point it rose to a maximum of (0.85±0.05) μm min^{-1} at ~80% Ar (note that at these conditions the etch selectivity with respect to Ni was ~80:1) before falling rapidly as sputtering increasingly dominates. The shape of this peak is presumably governed by the increasing Ar ion flux which aids removal of the passivating $InCl_3$ and the dilution of chemical etching effects of chlorine as the Ar content increases. It is perhaps not a coincidence that the peak in etch rate corresponds to the conditions under which the AlGaInP sidewalls of the ridge structure became vertical (the same may be so for GaAs also but there are insufficient points to tell).

The post etch RMS surface roughness was measured on surfaces between ridges from which 0.5 μm of GaAs and 1.0 μm of AlGaInP had been removed. The most striking feature is that the roughness has a sharp maximum of value (25.3±1.0) nm at the same conditions as the maximum etch rate was reached. Although not entirely clear is seems possible that this may be the point at which $InCl_3$ is effectively cleared, although not entirely uniformly, from the etching surface. The graph also indicates that lower roughness is obtained at higher Ar fraction when sputtering dominates and the surface is free of passivant compared to below where the $InCl_3$ is still present.

The range over which vertical features are produced in both GaAs and AlGaInP with high etch rate and low post-etch roughness is ~82-85% Ar (indicated by a grey bar in Figure 5.27). Using 85 % Ar, at which the AlGaInP etch rate has dropped slightly to (0.63±0.05) μm min^{-1} and there is a dramatic drop in surface roughness to ~1nm, a range of 1-D sub-micron features were patterned and etched in the laser material. Figure 5.29 shows a grating nominally consisting of 100 nm lines with 200nm period, similar to the period required to fabricate first order Distributed Bragg reflectors for edge-emitting lasers, with approximately vertical sidewalls. A slight overexposure in the lithography step has resulted in the semiconductor portions of the grating being slightly greater than half the period. Also, there is rounding of the tops of the etched features which may be caused by a slight retreat of the Ni mask. This is unlikely to affect the optical mode, which is confined deeper in the structure. Importantly, the horizontal removal of Ni is significantly less than that observed in SiO_2 masks. The measured etch depth of the structures in Figure 5.29 is (1.95±0.05) μm which, as expected for high-aspect-ratio features [56], corresponds to a lower etch rate (~0.45 μm min^{-1}) than

measured in an open area of the sample. The feature aspect ratio is ~20:1 which I believe is the highest reported for this material system.

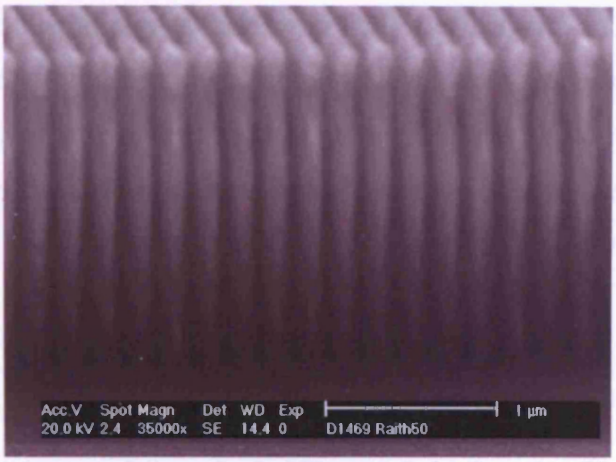

Figure 5.29 - Scanning electron micrograph of a 200 nm period 1-D grating. The aspect ratio is ~20:1.

Finally, during the course of this extended etch, laser interferometry on an open area of the sample indicated that the etch rate did not change as a function of time. This can be contrasted with previous measurements performed using BCl_3/Cl_2 chemistry, in the same system and at the same elevated temperature, during which the etch rate did change significantly with time as the sample temperature increased under the influence of the plasma and due to enhanced evaporation of $InCl_3$ [13]. This observation provides additional support for the earlier assertion that one of the actions of the increasing Ar fraction is to remove passivant from the surface, and that at the maximum etch rate the surface is largely passivant free.

5.7.3. Summary of the two-step vertical etching process

The sidewall profile of features etched in GaAs and AlGaInP is strongly dependent on Ar content in a $BCl_3/Cl_2/Ar$ plasma. However, the mechanisms for etching vertically for the two materials are shown to be quite different; GaAs etches chemically in Cl-rich environments causing severe undercut whereas AlGaInP is strongly passivated. As the Ar fraction was increased and the etch became more physical, the unpassivated GaAs cap directly underneath the Ni mask etched more anisotropically, acquired a vertical sidewall somewhere between 40 % and 75 % Ar and remained vertical whilst the mask remained intact. AlGaInP behaved very differently, showing clear evidence of $InCl_3$

passivation (a positive sidewall profile) at low Ar concentrations and slight undercutting (indicative of passivant removal and chemical, isotropic etching) at 90 % Ar.

It is remarkable that despite the difference in etch mechanisms and the use of a 2-step process, at the same Ar fraction vertical sidewall features were achieved not only on relatively wide ridges but also in a 1-D array with 200 nm lattice constant and 20:1 aspect ratio. To the best of my knowledge these are the deepest vertically etched structures on a scale suitable for fabrication of 1st order photonic crystals in AlGaInP.

5.8. Etching of GaAs and AlGaInP in a single process step

One of the findings of the preceding etch study was that the sidewall profile of GaAs is much less sensitive to the process conditions than AlGaInP. That is to say that GaAs etches vertically under a wider range of conditions. It therefore seems an obvious progression to see if GaAs will etch vertically under the same conditions that are needed to etch AlGaInP – allowing both material layers to be etched in one process step. Figure 5.30 is a SEM image showing the sidewall profile of an AlGaInP/GaAs laser structure etched in this way. It can be seen from the figure that GaAs does indeed etch anisotropically under these conditions with an etch rate is similar to that of AlGaInP. This is an important finding as it allows a much higher throughput in the fabrication of devices. The exact process parameters used are given in Table 5.2.

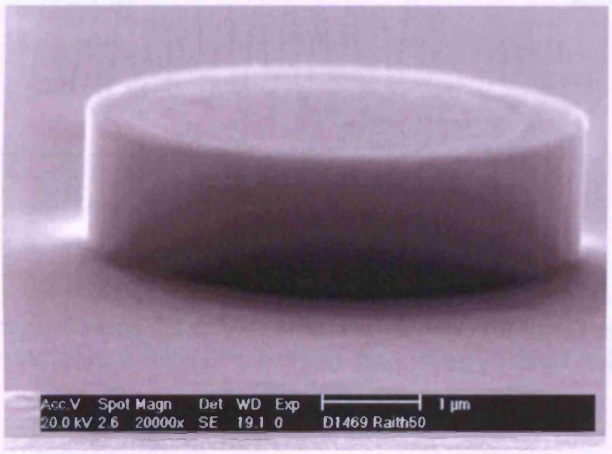

Figure 5.30 – Scanning electron micrograph showing the sidewall profile of a circular feature etched in an AlGaInP/GaAs laser structure using a single etch step at 180 °C, 100 W RIE, 1000 W ICP (all other conditions as in Table 5.1).

Temperature	180 °C
ICP Power	1000 W
RIE Power	100 W
BCl_3 Flow Rate	4.4 sccm
Cl_2 Flow Rate	2.6 sccm
Ar Flow Rate	33 sccm
Chamber Pressure	10 mTorr
He Backing Pressure	10 Torr

Table 5.2 – Process parameters for the single-step AlGaInP/GaAs ICP etch.

5.8.1. Temperature dependence and etch rate stability

Figure 5.31 shows laser interferometry signals as a function of time for a sample etched with 82.5% Ar and a sample etched in an Ar free plasma. Clearly, there is a strong

contrast between the etch rate of the material etched in the Ar free plasma, which more than doubles during the etch, and the steady etch rate when using 82.5% Ar. These etch rate dependences are shown in the inset of Figure 5.31.

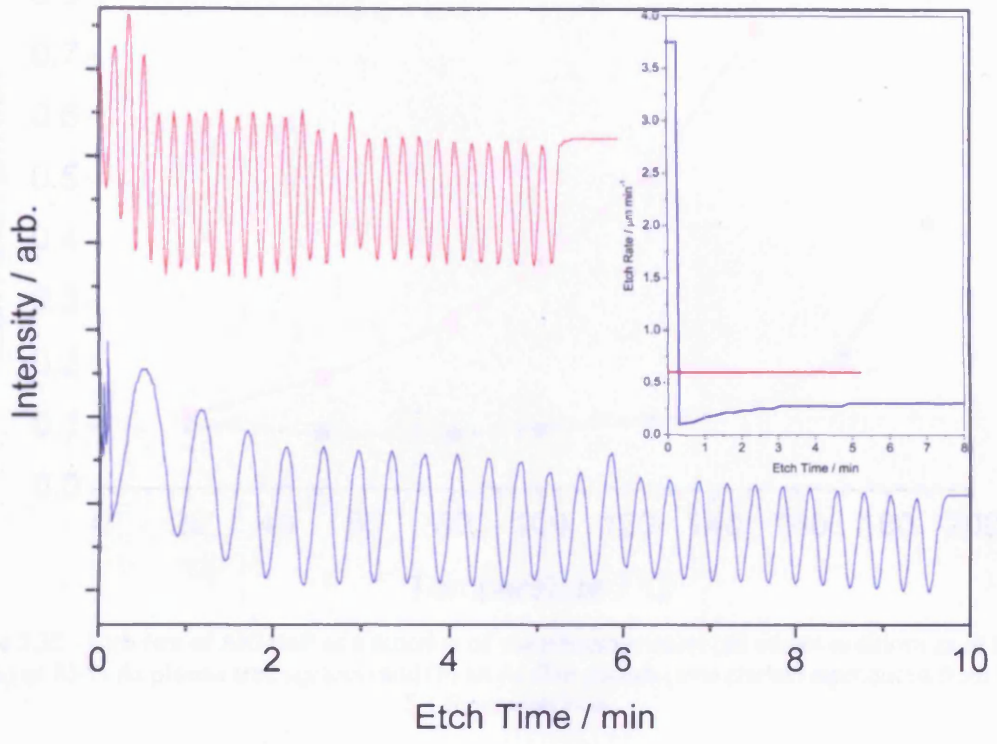

Figure 5.31 - Interferograms showing the etching behaviour of AlGaInP for (a) an 82.5 % Ar plasma (red line, top) and (b) an Ar-free plasma (blue line, bottom). Inset: the equivalent etch rates as a function of etch time.

By considering the temperature dependences of the AlGaInP etch rate for these two regimes (shown in Figure 5.32) the reason for these time dependences becomes clear. When etching with an Ar free plasma the etch rate is strongly temperature dependent as previously discussed. This in turn leads to a strong time-dependence at elevated temperature due to heating of the sample by the plasma. In contrast when etching with 80 % Ar the etch rate has a very different dependence on temperature. As the temperature is increased above 20 °C there is a significant rise in etch rate but this rise begins to saturate at temperatures above ~150 °C. At 180 °C the etch rate is fairly insensitive to temperature which explains why the etch rate does not change with time under high Ar conditions. This is consistent with the assertion that the strong temperature dependence of the AlGaInP etch rate in Cl environments is due to increased thermal desorption of $InCl_3$ at elevated temperatures – with $InCl_3$ efficiently removed by ion- and thermal-assistance the temperature dependence lessens.

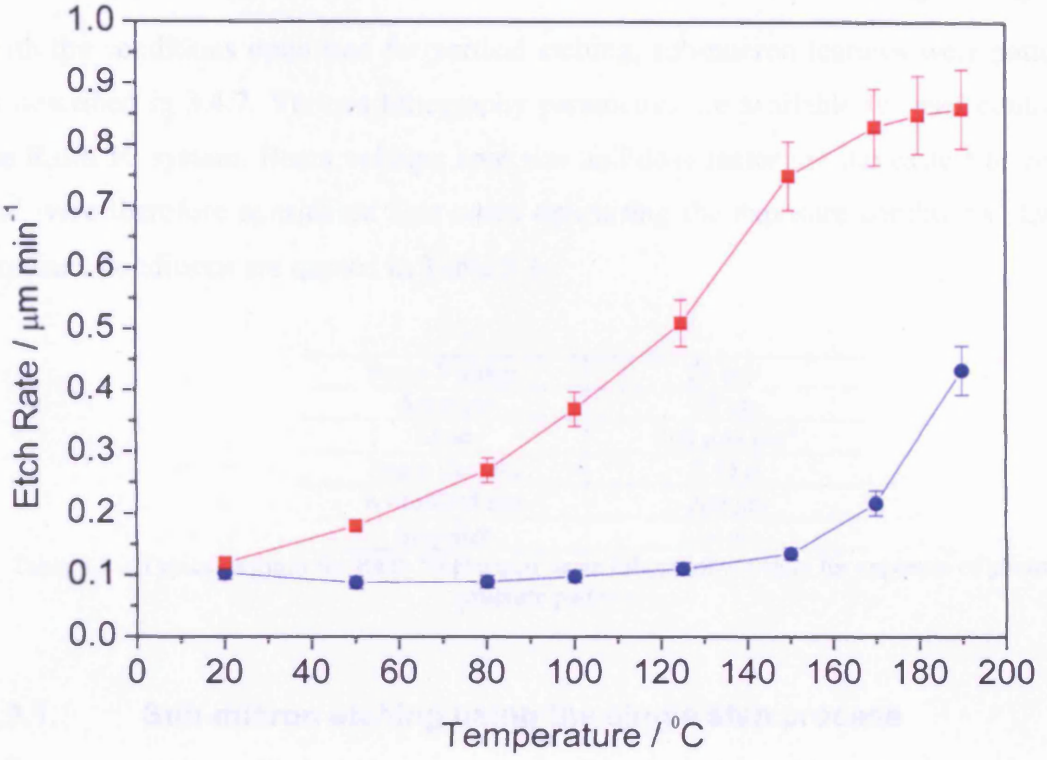

Figure 5.32 - Etch rate of AlGaInP as a function of sample temperature (all other conditions as in table 1) for (a) an 85 % Ar plasma (red squares) and (b) an Ar-free plasma (blue circles) reproduced from Figure 5.1 for comparison.

5.9. Application of the etch process to sub-micron gratings

With the conditions optimised for vertical etching, sub-micron features were patterned as described in 3.4.7. Various lithography parameters are available for user control on the Raith 50 system. Beam voltage, spot size and dose factor are the easiest to control and were therefore considered first when optimising the exposure conditions. Typical exposure conditions are quoted in Table 5.3.

Beam Voltage	20 keV
Aperture	25 μm
Dose	200 μAs cm^{-2}
Beam Current	0.15 A
Write-field size	200 μm
Step size	10 nm

Table 5.3 – Typical settings for Raith 50 electron beam lithography system for exposure of photonic structure patterns.

5.9.1. Sub-micron etching using the single step process

A number of effects were observed when etching sub-micron features in AlGaInP with an 85% BCl_3/Cl_2/Ar ICP. Perhaps the most important for etching the deep, high aspect-ratio features required to fabricate photonic structures is aspect ratio dependent etching (ARDE) where the etch rate typically decreases with increased aspect ratio [56,57]. ARDE is difficult to quantify because the aspect-ratio of any feature changes with time during the etch. Therefore, to make rigorous measurements of the etch rate as a function of aspect ratio requires measurements of etch depth to be made on samples patterned with a range of feature sizes etched for a range of times. This is time and material consuming, therefore, more straightforward measurements of etch depth (to infer the average rate) as a function of linewidth were made under various plasma conditions to assess the relative degrees of ARDE.

The single step process described in Section 5.8 was used to etch sub-micron gratings. The resulting structures exhibited severe ARDE such that the achievable etch depth was very much shallower than that required to etch DBRs in these laser structures. A typical example is shown in Figure 5.33.

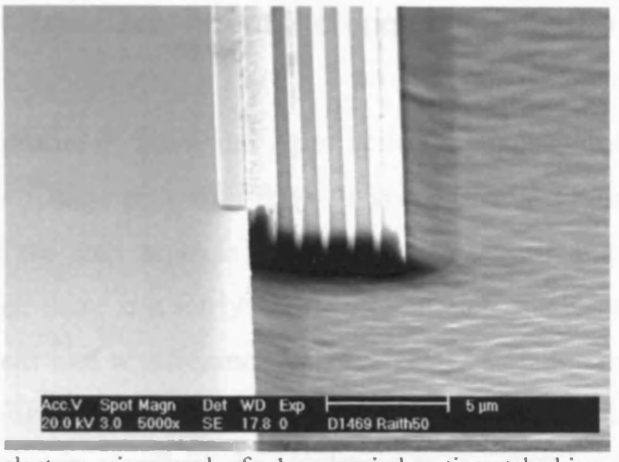

Figure 5.33 - Scanning electron micrograph of a 1 µm period grating etched in a single step with 82.5 % Ar in a BCl_3/Cl_2/Ar ICP.

As previous results (e.g. Figure 5.29) have shown that there is no fundamental reason why these aspect ratios can not be achieved it seemed likely that the cause of the problem is the etching of the GaAs cap at elevated temperatures. To determine whether this was the case a GaAs/AlGaAs laser structure was etched at 25 °C and at 180 °C. The resulting structures, shown in Figure 5.34, show that whereas at room temperature there is very little ARDE at 180 °C the GaAs/AlGaAs structure barely etches at all. This is consistent with the explanation that in the single-step process the GaAs cap is limiting the etch rate, making this process unsuitable for high-aspect-ratio etching of AlGaInP/GaAs structures.

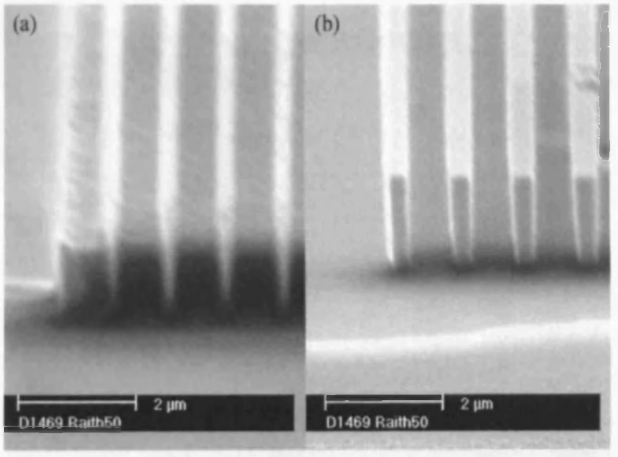

Figure 5.34 - Scanning electron micrographs of 1 µm period gratings etched in a GaAs/AlGaAs laser structure at (a) 180 °C and (b) 25 °C with 82.5 % Ar in a BCl3/Cl2/Ar ICP.

5.9.2. Aspect Ratio Dependent Etching (ARDE) in the two step process

The cross-sectional profile of 1 μm and 2 μm period gratings etched in AlGaInP/GaAs structures using a two stage etch with 85% Ar are shown in Figure 5.35(a). The first thing to note is that the etch depth is far greater than seen in Figure 5.33. ARDE is, however, still evident; there is a fairly abrupt step in etch depth between the patterned and un-patterned areas and a difference in the etched depth for the different periods. Closer inspection (Figure 5.35(b)) reveals that within the etched trench the surface appears to be uniform and smooth as expected from Figure 5.27 and Figure 5.28.

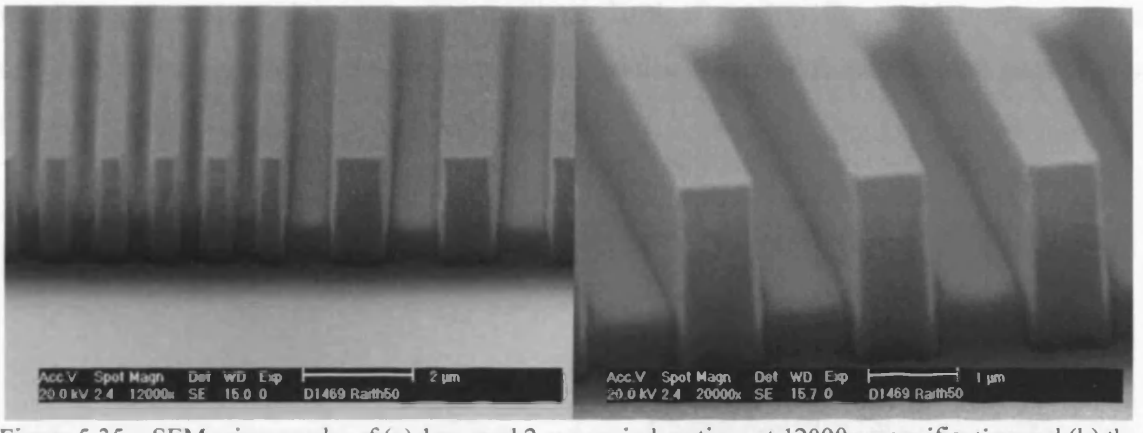

Figure 5.35 – SEM micrographs of (a) 1μm and 2 μm period gratings at 12000x magnification and (b) the 2 μm period grating at 20000x magnification showing aspect-ratio dependent etching (ARDE) in AlGaInP etched in a two step process with 85 % Ar in a BCl3/Cl2/Ar ICP.

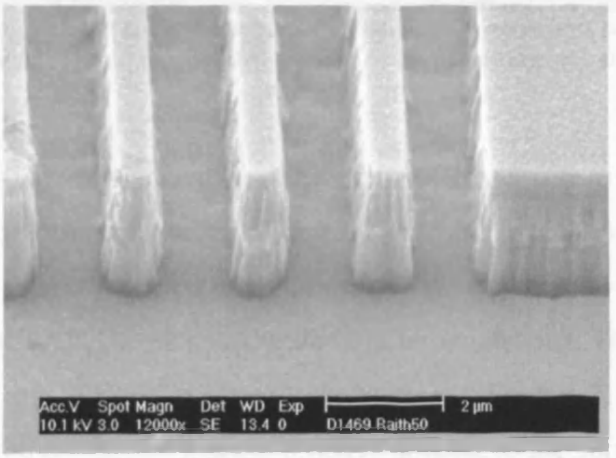

Figure 5.36 - Scanning electron micrograph of a 2 μm period grating etched in two stages with 80 % Ar in a BCl_3/Cl_2/Ar ICP showing no aspect-ratio dependent etching (ARDE).

Figure 5.36 shows a 2 μm pitch grating etched with 80 % Ar at 180°C. In contrast to the structure etched at 85 % Ar no ARDE is observed. As expected, the sidewalls are rough

and have a very slightly angled profile when etching under these conditions. The surface of the trench floor also appears to rougher and less uniform than seen in Figure 5.35. At 80 % Ar, where the etch rate reaches its peak value, the etch rate is equal to the removal rate of $InCl_3$, which is rate limiting. As the Ar fraction is further increased the supply of neutral species to take part in reactions with the semiconductor limits the etch rate. The observed increase in ARDE as the Ar fraction is increased is therefore also likely to be caused by further localized reduction in neutral species. Coburn et al. give a simple vacuum conductance argument to explain the effect that holds if the etch rate is not limited by an ion-assisted process [78]. The results are also consistent with what was reported by Giapis et al. who reported uniform etching on both macroscopic and microscopic scales when the etch rate was limited by ion flux, which is naturally uniform and conversely non-uniform etching when the conditions allowed neutral gas transport to the surface to be rate limiting [55].

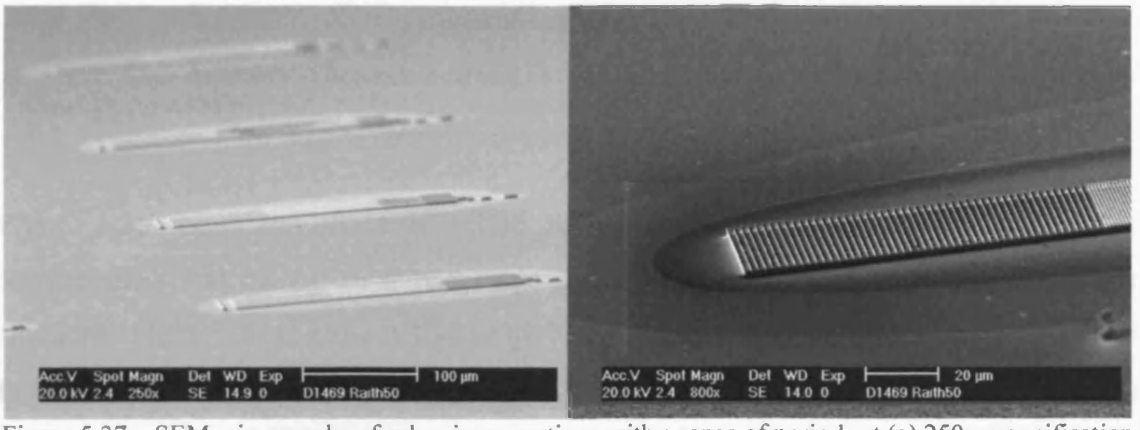

Figure 5.37 – SEM micrographs of sub-micron gratings with a range of periods at (a) 250x magnification and (b) 800x magnification. The regions around areas of dense patterning etch at a lower rate than open regions.

Figure 5.37 gives lower magnification views of patterned test gratings. A region of sloped semiconductor surrounds areas of dense patterning which means the etch rate is lower. This effect was reported by Gottscho et al. [56] when etching III-V semiconductors in $BCl_3/Cl_2/Ar$ plasmas under similar conditions. The explanation given describes the effect resulting from neutral shadowing, whereby in a regime where the etch reaction is limited by flux of neutral reactive species to the surface and transport is in via molecular flow the flux of the species is hindered as the aspect ratio of features increased. When etching with 80 % Ar at 180 °C this effect is again absent supporting the case that neutral flux is responsible for the ARDE of AlGaInP.

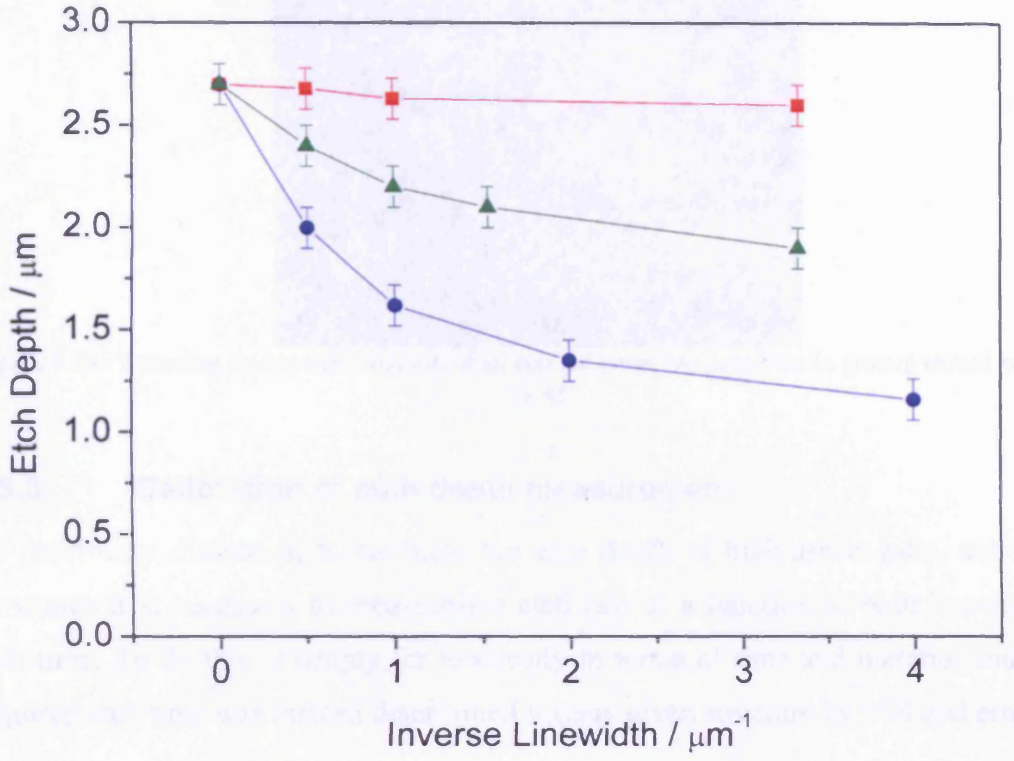

Figure 5.38- Aspect-ratio dependent etching (ARDE) - etch depth plotted as a function of inverse linewidth for AlGaInP/GaAs etched in a two-step BCl3/Cl2/Ar plasma containing 80 % (red squares), 82.5 % (green triangles) and 85 % (blue circles) Ar.

Figure 5.38 shows the effect of ARDE for three samples patterned with a range of feature sizes and etched in a two stage process with 80 %, 82.5 % and 85 % Ar fractions. There is negligible ARDE at 80 % Ar and as the Ar fraction is increased there is a corresponding increase in the strength of the dependence on feature size. There is a fine balance to be made between the quality of the sidewall and the effects of ARDE and the range of conditions over which both can be satisfied for sub-micron high-aspect-ratio features is even narrower than the range of conditions that allow anisotropic etching of low-aspect-ratio features. Therefore, for applications that require very high aspect-ratio features, and so mask thickness is limited, it may be necessary to compromise on the sidewall quality to reduce the effects of ARDE. For less demanding requirements, however, a balance can be met, as shown in Figure 5.39. Here the sidewalls are vertical and the ARDE, although evident, has not adversely affected the etch.

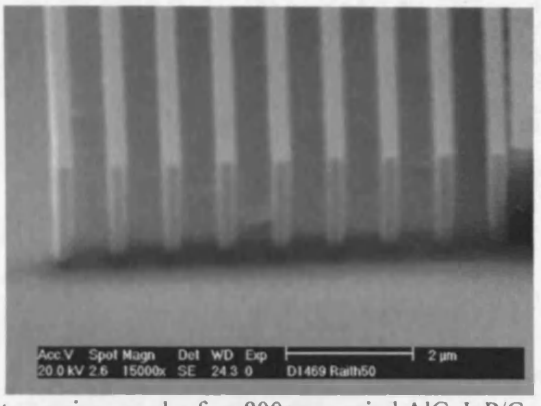

Figure 5.39 - Scanning electron micrograph of an 800 nm period AlGaInP/GaAs grating etched with 82.5 % Ar.

5.9.3. Calibration of etch depth measurement

As previously discussed, to calibrate the etch depth of high-aspect-ratio, sub-micron structures it is necessary to measure the etch rate as a function of both linewidth and etch time. To do this is simply far too costly in terms of time and material and so the required etch time was instead determined for any given structure by trial and error.

5.10. Summary

A process has been described which allows the fabrication of high-aspect-ratio, sub-micron features in AlGaInP/GaAs laser structures in a $BCl_3/Cl_2/Ar$ ICP. The process was arrived at by studying the effects of the main process parameters on the etch rate, selectivity and post-etch surface roughness leading to an understanding of how the interactions between the semiconductor materials and the plasma under different process conditions gives rise to different sidewall geometries.

The greatest enhancement in phosphide etch rate was achieved by raising the sample temperature from room temperature up to 190 °C. Since etching of the mask is largely temperature insensitive this also produced the largest enhancement in selectivity. At 190 °C an AlGaInP etch rate up to 0.7 μm min^{-1} and a selectivity, with respect to Ni, as high as 70:1 were achieved. This was a far greater enhancement than produced by changing any other parameter alone. However, there is a requirement for thermal contact between sample and carrier, over the required process time, which places an upper limit on the available temperature range. With Fomblin oil, a temperature of 190 °C is close to this limit since the oil evaporates leading to loss of thermal contact and thermal runaway. As the AlGaInP etch rate and the selectivity obtained at below 190 °C are sufficient for the etch depths required this effect should not be a problem here.

At elevated temperature further enhancement to the phosphide etch rate and selectivity were achieved adding 80-85 % Ar to the gas composition. An AlGaInP etch rate up to 0.85 μm min^{-1} and a selectivity, with respect to Ni, as high as 125:1 were achieved at 180 °C.

The power- and pressure-dependent results can be understood by considering that the AlGaInP etch rate is strongly dependent on both dc bias and ion flux while for SiO_2 it is strongly dependent on flux but not dc bias. This is consistent with the ion energy being important in the removal of $InCl_3$ but being much less important in the formation of etch products with SiO_2. These observations are also consistent with the observation that the selectivity is improved by increasing the RIE power at the expense of ICP power.

The sidewall profile of features etched in GaAs and AlGaInP is strongly dependent on Ar content in a $BCl_3/Cl_2/Ar$ plasma. However, the mechanisms for etching vertically for the two materials are shown to be quite different; GaAs etches chemically in Cl-rich environments causing severe undercut whereas AlGaInP is strongly passivated. As the Ar fraction was increased and the etch became more physical, the unpassivated GaAs cap directly underneath the Ni mask etched more anisotropically, acquired a vertical sidewall somewhere between 40 and 75% Ar and remained vertical whilst the mask remained intact. AlGaInP behaved very differently, showing clear evidence of $InCl_3$ passivation (a positive sidewall profile) at low Ar concentrations and slight undercutting (indicative of passivant removal and chemical, isotropic etching) at 90% Ar.

A process for anisotropically etching AlGaInP/GaAs laser structures in a single, high temperature step at 180 °C has been demonstrated. The etch rate is stable over the duration of the etch due to its insensitivity to temperature and the post-etch surface is smooth.

However, the single step process is unsuitable for etching high-aspect-ratio features due to the strong aspect-ratio dependence of the GaAs etch rate at 180 °C. Therefore, a two stage etch was required where the GaAs is etched at lower temperature (25 °C) and the AlGaInP layers are etched at 180 °C. With this etch we have shown that there is still aspect-ratio dependent etching of AlGaInP when etching is limited by transport of neutral species to the surface and the effect is not observed when removal of the etch product is rate limiting. As the Ar fraction is increased (above ~80 %) and the amount of available neutral reactive species is depleted the ARDE effect becomes more pronounced.

Finally, with an optimized set of etch parameters, etching of high-aspect-ratio, sub-micron features in AlGaInP/GaAs laser structures has been demonstrated. Despite the difference in etch mechanisms of GaAs and AlGaInP and the use of a 2-step process, at the same Ar fraction vertical sidewall features were achieved not only on relatively wide ridges but also in sub-micron gratings. Using this process a range of 1-D arrays were etched with lattice constants as short as 200 nm and aspect ratios as high as 20:1. To the best of my knowledge these are the deepest vertically etched structures on this scale in AlGaInP.

6. Deep-etched AlGaInP/GaAs laser devices

6.1. Introduction

In this chapter I will describe the application of the etch process defined in Chapter 5 to real laser devices. The measurement techniques used to characterise the devices, in particular the apparatus used to measure L-I and I-V characteristics, is given. Descriptions of how the threshold current density are extracted from the L-I characteristic, and how I-V characteristics are used to make comparisons between devices to ensure they are electrically identical are given. Comparisons are made between devices containing Distributed Bragg Reflectors with cleaved and etched facet Fabry-Perot devices. Finally, the use of the etch process to fabricate a prototype integrated emitter and detector on a single chip for potential biophotonic applications is described.

6.2. Laser device fabrication

All devices studied in this project were processed in the cleanroom facilities of Cardiff University by the author. The devices described were all grown on n-type substrates and are processed and mounted n-side down. The wafer material was fabricated into both laser and segmented contact devices. The exact details of the segmented contact device structure are described in Appendix II. The fabrication processes for devices incorporating DBRs is based on a standard oxide isolated stripe device process described in reference 79.

6.2.1. Laser devices

All lasers described in this thesis are oxide isolated stripe devices. Stripe width is typically 20 μm and the orientation of the stripe is such that the facet lies along the (100) plane when cleaving perpendicular to the stripe. The basic device structure is depicted in Figure 6.1 with specific details of the epitaxial layers given in Figure 6.2. When fabricating microstructures in this type of symmetrical structure it is desirable to etch completely through to the substrate. This gives the maximum step in effective refractive index (as the optical mode sees mainly air in the air-gaps) but this also ensures that the effective index profile in the z-direction is symmetrical. This is

important to prevent the optical mode from being pushed toward the substrate, reducing the confinement factor, Γ.

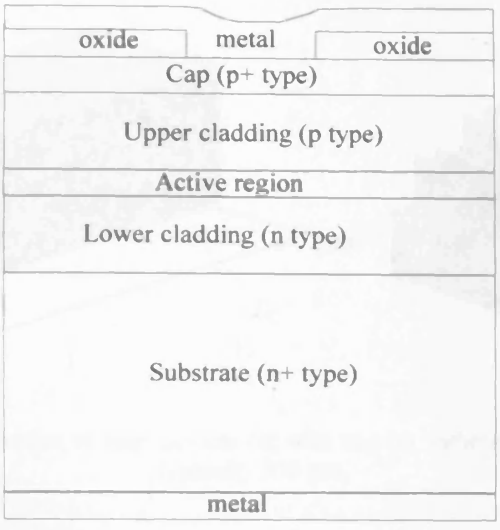

Figure 6.1 – Schematic illustration of the edge of an oxide isolated stripe laser, showing the various layers.

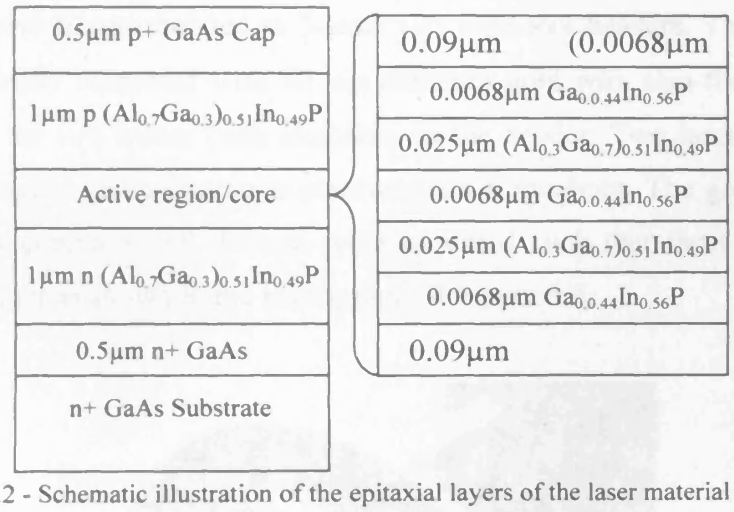

Figure 6.2 - Schematic illustration of the epitaxial layers of the laser material used.

To process the wafer into laser chips involves various lithography, deposition and etching steps. The outcome of this processing are the devices similar to that depicted in Figure 6.3. For the devices presented here the cavity length was fixed at 500 μm. It is important when describing lasers with distributed reflectors to be clear when defining cavity length. The length of a standard plain facetted cavity is fairly well defined, however, this is not the case with distributed reflector cavities. For this work the cavity length of devices containing photonic reflectors is taken as the distance between the innermost semiconductor-air interfaces of each reflector. Considering the device lengths

used and the low numbers of grating periods it is not a great concern anyway as the cavity length is much greater than the extent of the grating.

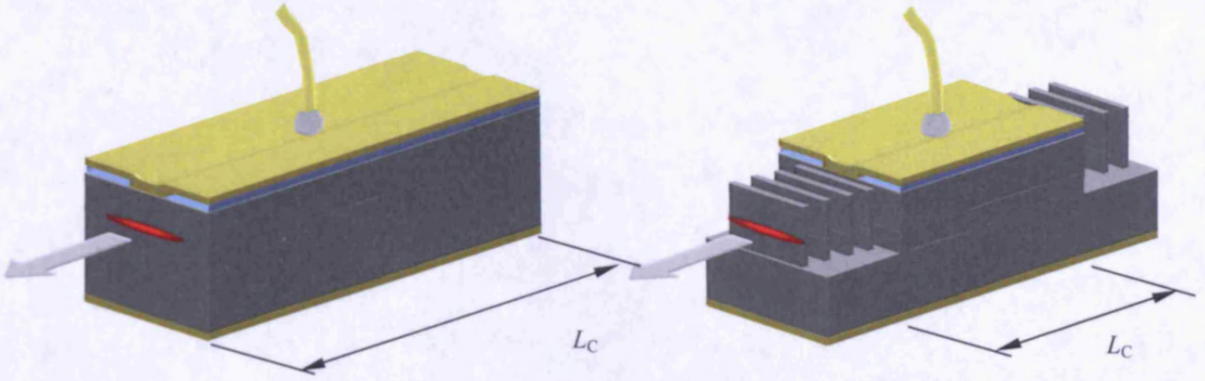

Figure 6.3 – Schematic illustration of laser devices (a) with and (a) without micro-structured mirrors. L_C typically 500 µm.

6.2.2. Device mounting

After processing laser devices were bonded with Epo-Tex H20E silver epoxy to copper heat sinks that were in turn bonded to 3-lead T05 transistor headers. The p-type sides were then electrically contacted with 50 µm diameter gold wire also fixed with silver epoxy to one of the two solder pads available on the header. Two laser devices were mounted per 3-lead header to improve measurement throughput. The ground for these two devices was common. All devices were mounted such that facet emission was normal to the header as shown in the photograph of Figure 6.4.

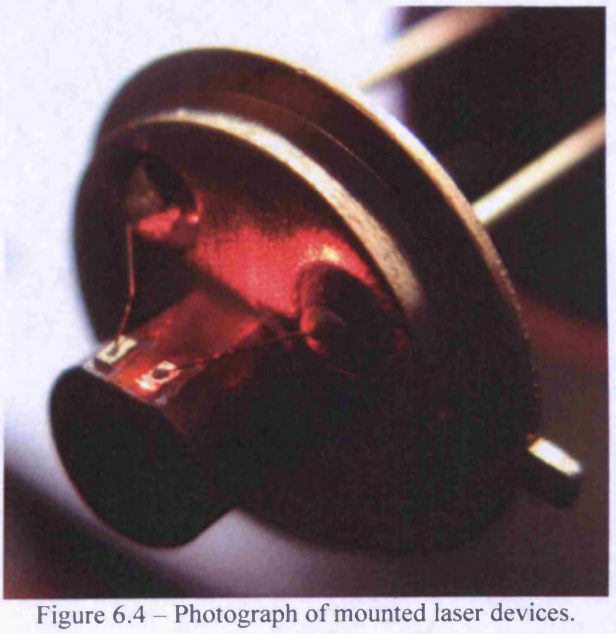

Figure 6.4 – Photograph of mounted laser devices.

6.3. Standard device measurement techniques

In this section some the commonly used techniques employed to measure the performance of laser diodes are described.

6.3.1. Laser threshold from light vs. current characteristic

The system used to measure both the light vs. current (L-I) and current vs. voltage (I-V) characteristics of laser structures was built by K. Griffiths and is described in more detail in his thesis [80]. All devices are driven at a pulse repetition rate of 1 kHz at a duty cycle of 0.004 to prevent sample heating and measurements are gated. The sample stage consists of a device holder within an evacuated cryostat mounted on a microscope sample stage through which runs a copper cold-finger which is immersed into liquid nitrogen (LN_2). The cold-finger is thermally coupled to the copper heat sink onto which the device is mounted. This allows control of the temperature in the 130K to 390K range.

Figure 6.5 shows a typical L-I characteristic for a quantum well laser. The curve consists of two distinct linear regions with different slopes. The current at which the change of slope occurs is the threshold current, I_{th}. Below this current the radiative recombination within the device is dominated by spontaneous emission which increases with drive current. However, at threshold, where the round trip gain matches the cavity loss, the spontaneous emission rate clamps and any further increase in drive current causes an increase in light due to stimulated emission.

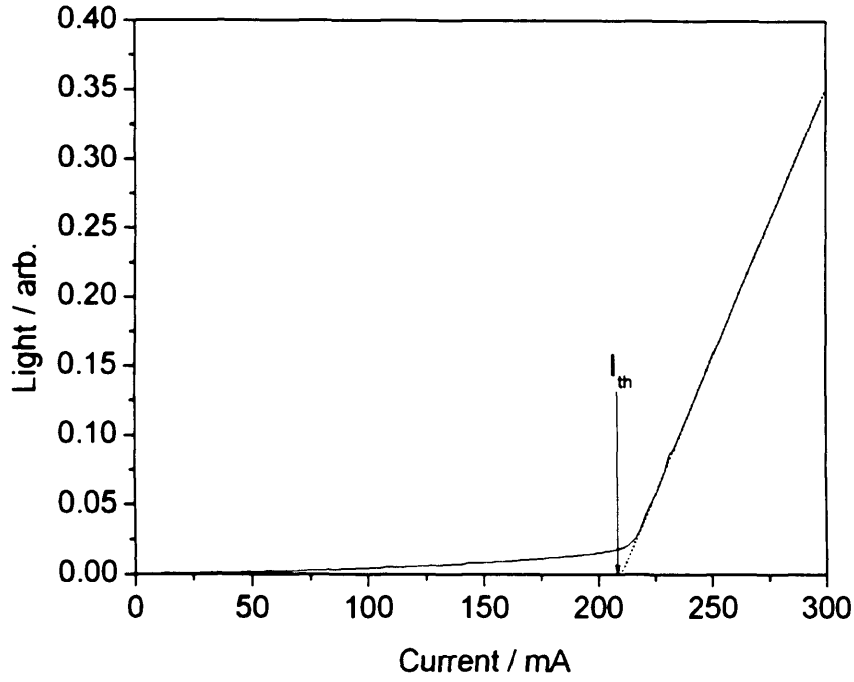

Figure 6.5 – Typical L-I characteristic of a semiconductor laser diode. Ith is taken where the tangent of the curve above threshold meets the x-axis.

I-V characteristics of laser devices are made to determine the turn on voltage of a device and to assess the consistency between one device and another. I-V measurements are also made on the individual sections of the segmented contact devices to ensure that the sections are electrically identical (Appendix II).

6.3.2. Measurement of lasing wavelength

Laser wavelength is measured above threshold with an Ando AQ6317 Optical Spectrum Analyser (OSA). The experimental setup is shown in Figure 6.6. Light from the device is focused with a microscope objective onto the end of an optical fibre which guides light into the OSA. The OSA has a wavelength range of 600 – 1750 nm, is accurate to ±0.5 nm and has a maximum resolution of 0.015nm.

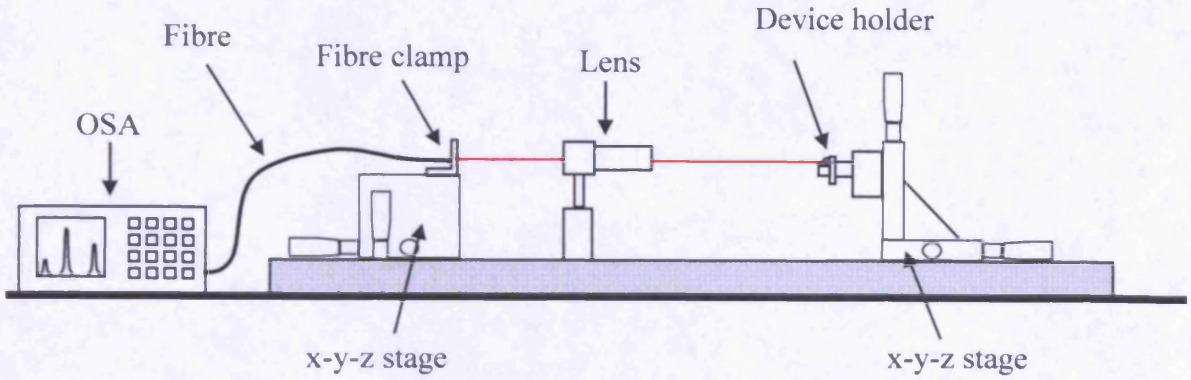

Figure 6.6 – Experimental setup for measuring laser wavelength.

6.3.3. Measurement of near-field patterns

Measurements of the near-field pattern of a device are a useful indication of the quality of the facet condition, contact uniformity and current spreading. The device is orientated such that the epitaxial layers are perpendicular with the input slit. Light from the device is focused with a microscope objective via a variable neutral density filter onto a CCD camera. The camera is connected to a PC with commercially available software for recording the image. The image is then digitised using Origin7 graphing software and the data from a single line of pixels is plotted to give the near-field intensity profile. A typical near-field image and intensity profile is shown in Figure 6.7.

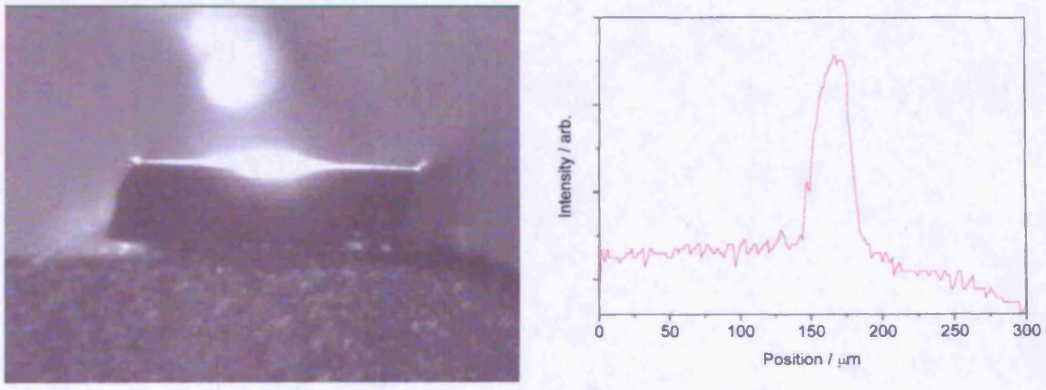

Figure 6.7 – Near-field image and intensity profile of a DBR laser device.

6.4. Dry-etched edge-emitting lasers

With an etch process capable of etching vertical facets in laser structures the obvious starting point in making an assessment of the quality of the etch (in terms of electrical leakage and optical quality) is to make a comparison between samples that are identical in every respect other than the formation of the facets; comparing etched facets with cleaved facets. This was done for 500 μm long oxide stripe isolated devices with a 20 μm stripe width. I-V and L-I characteristics of the devices were measured and these are plotted in Figure 6.8 and Figure 6.9 respectively.

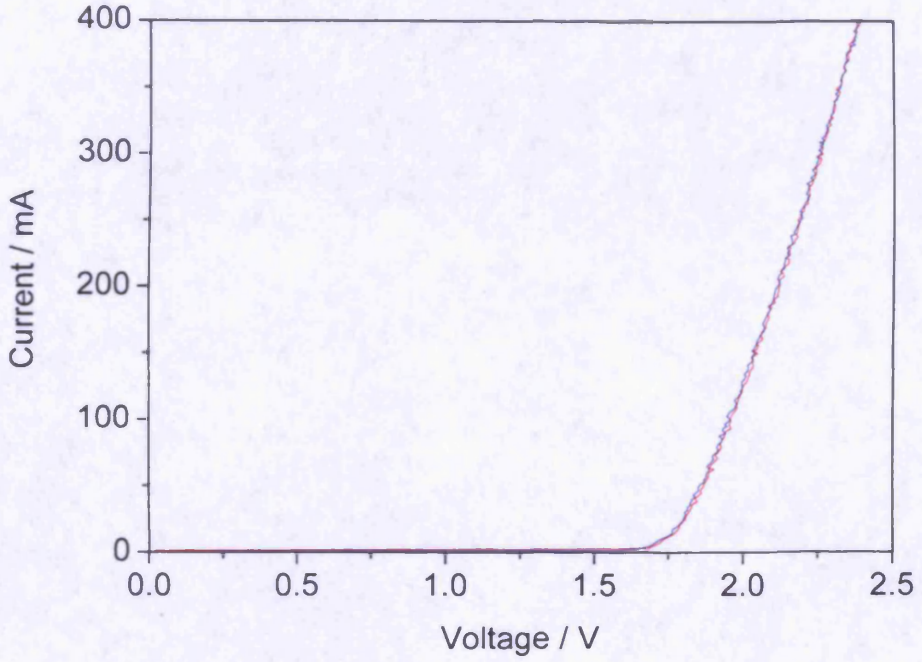

Figure 6.8 – I-V characteristics of 500 μm long lasers with cleaved (red) and dry-etched (blue) facets.

The I-V characteristics plotted for the two devices in Figure 6.8 show that the devices are electrically identical despite the etching. This is a positive indication that there is no catastrophic electrical damage to the p-n junction caused by the plasma.

However, the L-I characteristics in Figure 6.9 show that there is a considerable difference in laser threshold between the two devices. Whereas the device with cleaved facets has a threshold current of 210 mA the etched device has a threshold current of 270 mA.

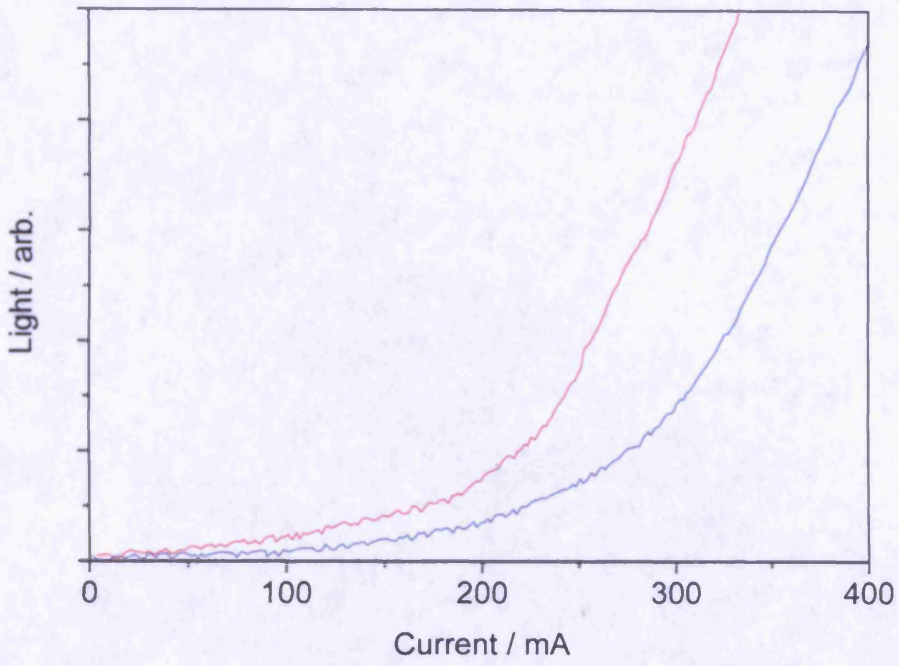

Figure 6.9 – L-I characteristics of 500 μm long lasers with cleaved (red) and dry-etched (blue) facets.

The likely explanation is that the finish of the etched facet, which can be seen in the SEM images of Figure 6.10 to be markedly rougher than a cleaved facet which is typically flat to within a few monolayers. This will inevitably increase the scattering losses and therefore increase the gain required for lasing.

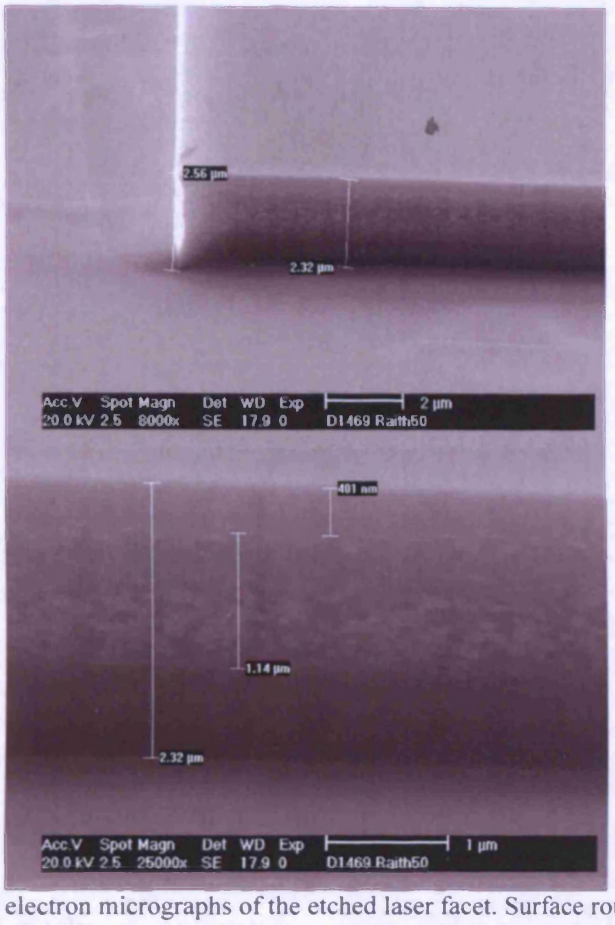

Figure 6.10 – Scanning electron micrographs of the etched laser facet. Surface roughness can be seen on the different epitaxial layers which are distinguishable.

6.5. DBR laser devices

Laser devices were then fabricated containing DBR reflectors with 850 nm and 1065 nm (as shown in the SEM image of Figure 6.11) periods. I-V and L-I characteristics were compared with Fabry-Perot devices without DBRs and these are shown in Figure 6.12 and Figure 6.13 respectively.

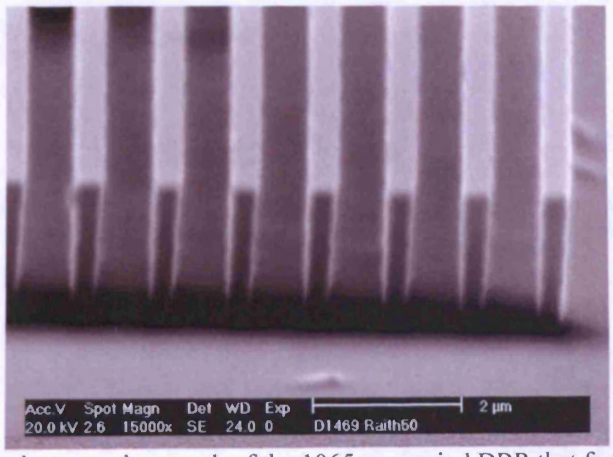

Figure 6.11 – Scanning electron micrograph of the 1065 nm period DBR that forms one end of the laser cavity.

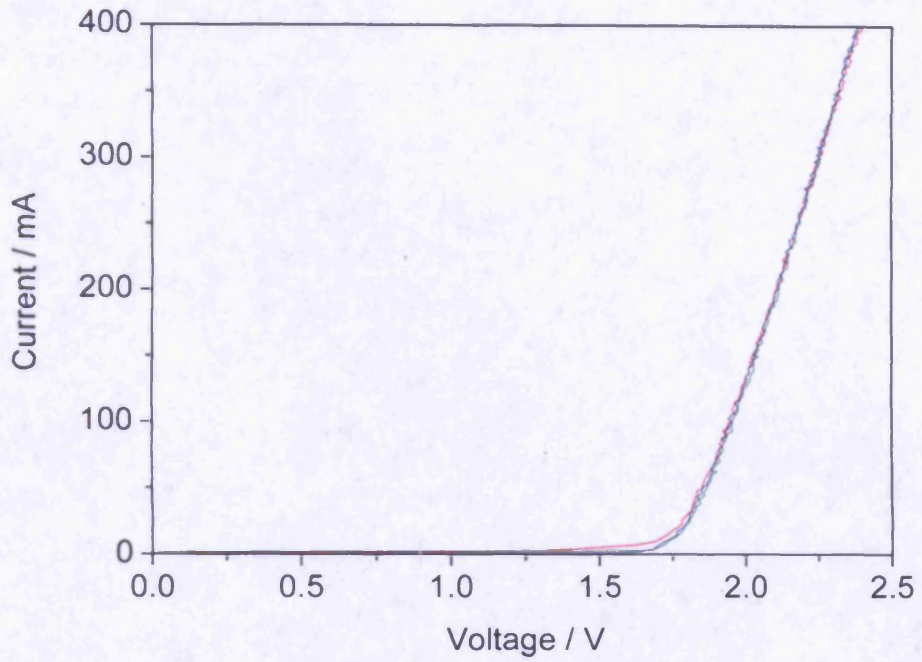

Figure 6.12 – I-V characteristics of of laser devices with plain etched facets (blue), period DBRs (green) and period DBRs (red)

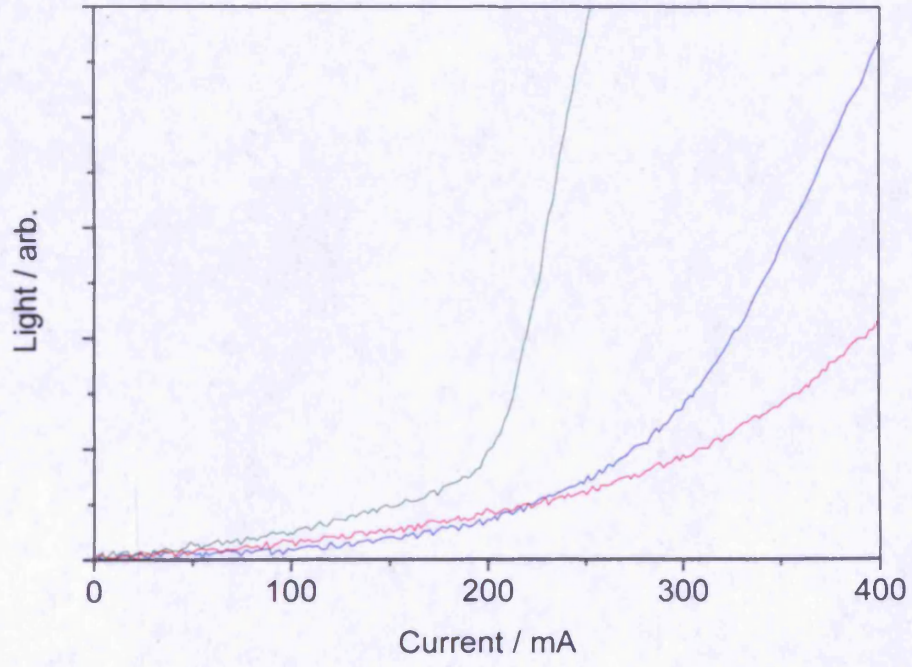

Figure 6.13 – L-I characteristics of laser devices with plain etched facets (blue), 1065 nm period DBRs (green) and 850 nm period DBRs (red)

Again the I-V characteristics of the devices, plotted in Figure 6.12, show that the devices are electrically identical. For the device with 1065 nm period DBRs the L-I curve shows that there is an improvement in both threshold current and differential

efficiency. The threshold current drops from 270 mA for the plain etched facet to 195 mA for the 1065 nm DBR device. In contrast the device with 850 nm period DBRs has a poorer L-I characteristic and in fact does not reach threshold over the drive current range measured.

The effect of the DBRs on the behaviour of the devices can be understood by considering the reflectance spectra of the structures. Figure 6.14 shows the modelled reflectance spectrum for the DBRs the dimensions of which were measured with the SEM.

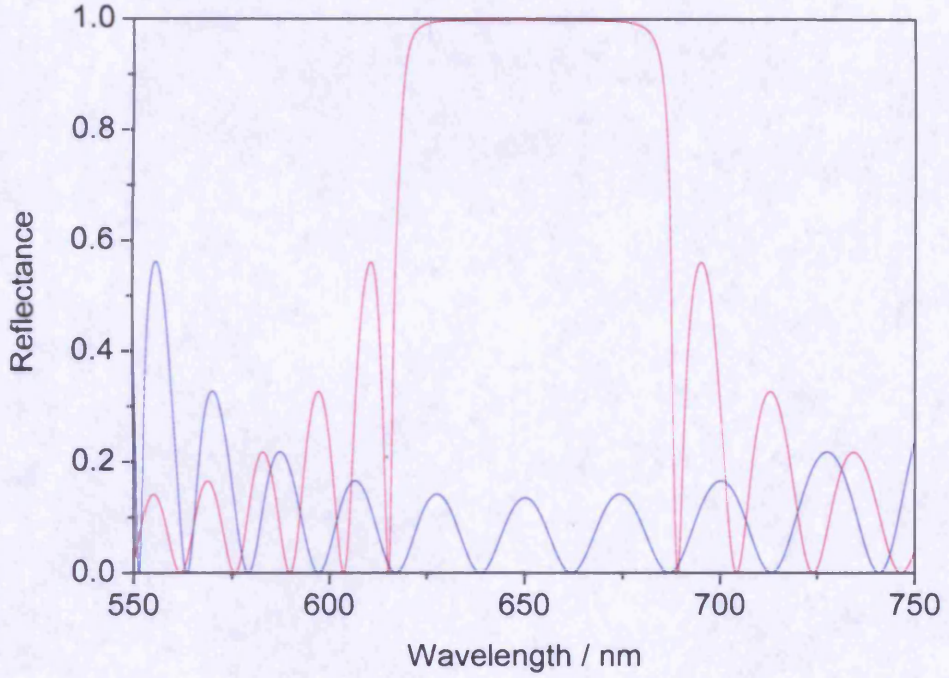

Figure 6.14 – Modelled reflectance spectra of 1065 nm period (red) and 850 nm period (blue) DBRs.

6.6. Integrated etched devices for potential biophotonic applications

The customisable optical and electronic properties of semiconductor optoelectronic make it an ideal technology for bio-photonic applications. Semiconductor laser and photo-diodes are widely used in bio-sensing and analysis systems but the potential for true bio-photonic integration i.e. embedding the living system within the semiconductor device has not really been exploited. Work by Gourley et al. [81] is a notable exception to with the inclusion of cell flow within a vertical cavity laser and bio-analysis via spectral analysis of the laser modes.

Dry-etched edge-emitting devices allows the development of integrated bio-photonic systems within the wafer plane for specific application to cell cycle and function analysis. The concept, shown schematically in Figure 6.8, is to integrate cell fluidics with LED or laser emitters plus detectors all within a single, monolithic chip. Structural information about the cell can then be obtained by angle resolved light scatter measurements and inverse transformation. This is an optical analogue of protein structure analysis via x-ray diffraction.

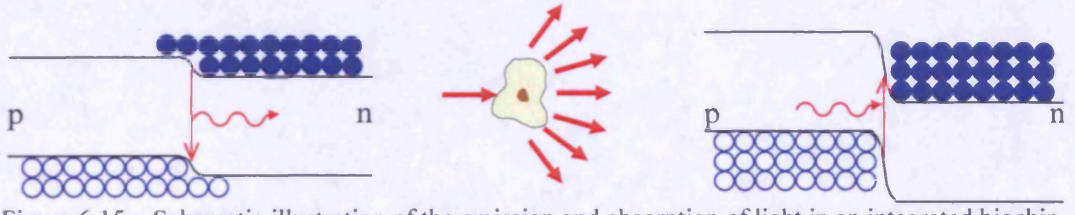

Figure 6.15 – Schematic illustration of the emission and absorption of light in an integrated biochip.

To integrate cell fluidics with LED or laser emitters plus detectors all within a single, monolithic chip a number of semiconductor fabrication issues must be addressed, the most important of which is the structuring by plasma-etching. Deep etched structures must be produced with sub-micron accuracy to enable both sample delivery and photonic control via periodic structuring. Multiple optically functionality must also be addressed with the isolation of light emitting and detecting areas and the fabrication of micro-lenses for controlled delivery of light at the point of interrogation.

Here a demonstration of the application of the etch process to simple integrated devices containing emitters and detectors and free space (into which living cells could be placed) is presented. Figure 6.16 shows a plan view representation of the test structure to be fabricated. The long, narrow device at the bottom of the diagram is the intended emitter with a fan-arrangement of photo-detectors. The position of a cell sample in a realised device is also depicted in the figure.

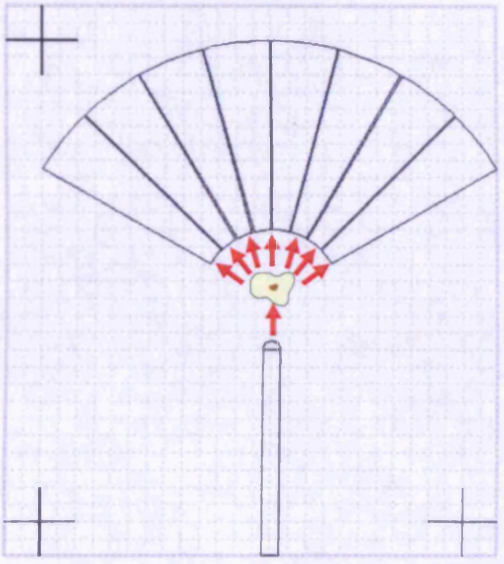

Figure 6.16 – Schematic depiction of the structure of the prototype device. The plan view is shown with the emitter at the bottom of the figure and a fan-arrangement of photo-detectors.

For the integrated device to be realised different devices on the same piece of wafer need to be isolated and the design must allow for the placement (and possibly manipulation) of cells. This requires deep (>10μm) etching. Accurate placement of the features (<100nm) and sub-wavelength structures (to allow photonic control) is needed which can be achieved with e-beam lithography.

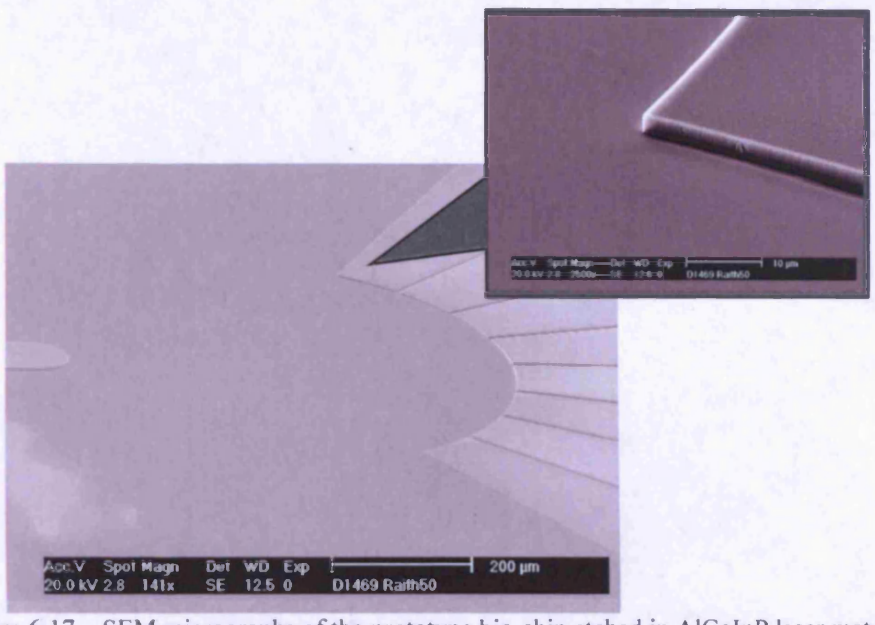

Figure 6.17 – SEM micrographs of the prototype bio-chip etched in AlGaInP laser material.

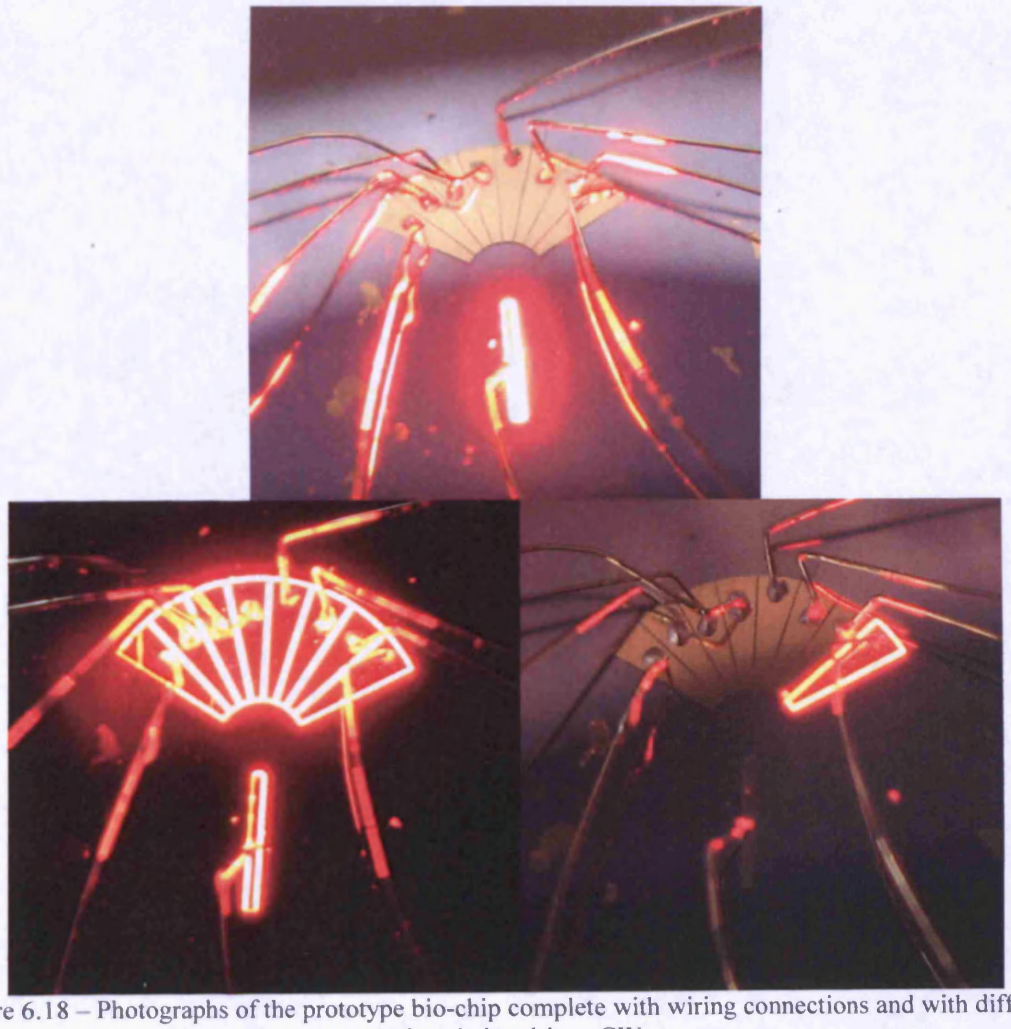

Figure 6.18 – Photographs of the prototype bio-chip complete with wiring connections and with different sections being driven CW.

Using the processes developed for fabricating laser structures it is possible to satisfy all of these requirements and realise such a device allowing isolation of devices and fabrication of optical elements on a single chip for bio-analysis applications. A scanning electron micrograph of the fabricated device after ICP etching is shown in Figure 6.17. The sidewall profile of the etched facet is also shown. Figure 6.18 shows the finished device being driven. The individual elements can be driven independently showing that they have been successfully isolated.

Figure 6.19 is a plot of photovoltage measured at one of the detector elements as a function of the current through the emitter device. This demonstrates that light can be emitted and detected by the integrated device over distances large enough to contain cells.

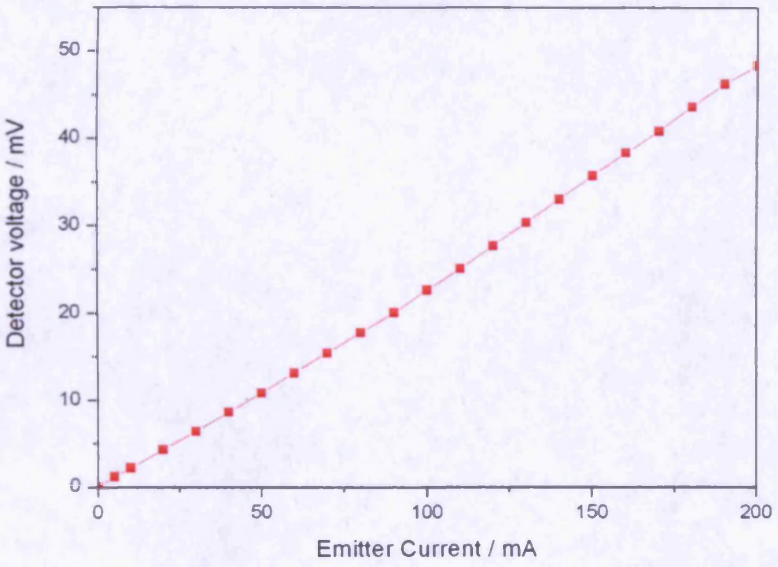

Figure 6.19 – A plot showing the photovoltage measured at one of the detector elements as a function of the drive current through the emitter.

6.7. Summary

Laser cavities defined by reflectors formed by plasma etching have been demonstrated in AlGaInP. Devices with cleaved facets, plain etched mirrors and distributed Bragg reflectors were fabricated and the electrical behaviour threshold characteristics of the devices compared.

The I-V characteristics of all the etched devices were identical to that of cleaved devices which is consistent with there being no catastrophic adverse effect of the etching on the p-n junction. There was, however, a significant increase in threshold current of devices with plain etched facets over cleaved. SEM analysis shows that the likely cause of this increase is the rougher semiconductor-air interface that results from dry-etching.

To overcome this increase in threshold current the mirror reflectance was increased by etching a 1065 nm distributed Bragg reflector microstructure at each end of a laser cavity. These structures were designed to have a stop-band centred on the lasing wavelength. With these reflectors there was an improvement in threshold current and differential efficiency. Devices were also fabricated with 850 nm DBRs which have a much lower reflectance at the lasing wavelength. As would be expected, performance of the device was much worse than both the 1065 nm DBR device, as well as the plain mirror device, with the device not reaching threshold over the drive current range measured.

Finally, a series of separate devices isolated on the same sample by plasma etching was demonstrated. The devices can be pumped independently and were shown to be able to emit and detect light on the same chip. Devices of this kind could potentially be used as integrated sensors for biophotonic applications.

7. Summary

7.1. Conclusions of this work

In this thesis I have described work to develop a process that allows the fabrication of high-aspect-ratio, sub-micron features in AlGaInP/GaAs laser structures in a $BCl_3/Cl_2/Ar$ ICP. Studying the effects of the main process parameters on the etch rate, selectivity and post-etch surface roughness has lead to an understanding of how the interactions between the semiconductor materials and the plasma under different process conditions gives rise to different sidewall geometries.

The behaviour of the two types of material in the presence of a Cl-based plasma was found to be very different due to the production of $InCl_3$ when etching the AlGaInP epitaxial layers that was obviously lacking when etching GaAs. This etch product was found to be involatile and rate limiting in Cl-rich plasmas. As the removal of this product was rate limiting and the In content for all AlGaInP alloys lattice matched to GaAs (49% In) the etch rate was found to be independent of the Al:Ga ratio.

The greatest enhancement in phosphide etch rate was achieved (when varying the process parameters independently) by raising the sample temperature from room temperature up to 190 °C. This has previously been shown to increase thermally assisted desorption of $InCl_3$. Since etching of the mask is largely temperature insensitive this also produced the largest enhancement in selectivity.

At elevated temperature further enhancement to the phosphide etch rate and selectivity were achieved adding 80-85 % Ar to the gas composition. Around these compositions the AlGaInP etch rate reached it's peak value. The time and temperature dependences of the etch rate at these compositions suggests that this is where the removal rate of the $InCl_3$ inhibitor layer first matches it's formation rate. This is corroborated by analysis of the post-etch RMS surface roughness as a function of plasma composition. With these conditions an AlGaInP etch rate of 0.85 $\mu m\ min^{-1}$ and a selectivity, with respect to Ni, as high as 125:1 were achieved at 180 °C.

The sidewall profile of features etched in GaAs and AlGaInP was also strongly dependent on Ar content in a $BCl_3/Cl_2/Ar$ plasma. However, the mechanisms for etching vertically for the two materials are shown to be quite different; GaAs etches chemically in Cl-rich environments causing severe undercut whereas AlGaInP is strongly passivated. As the Ar fraction was increased and the etch became more physical, the unpassivated GaAs cap directly underneath the Ni mask etched more anisotropically, acquired a vertical sidewall somewhere between 40 and 75% Ar and remained vertical whilst the mask remained intact. AlGaInP behaved very differently, showing clear evidence of $InCl_3$ passivation (a positive sidewall profile) at low Ar concentrations and slight undercutting (indicative of passivant removal and chemical, isotropic etching) at 90% Ar.

A process for anisotropically etching AlGaInP/GaAs laser structures in a single, high temperature step at 180 °C was demonstrated. The etch rate is stable over the duration of the etch due to its insensitivity to temperature (a result of the efficient removal of $InCl_3$) and the post-etch surface is smooth. However, the single step process was found to be unsuitable for etching high-aspect-ratio features. This is due to the strong aspect-ratio dependence of the GaAs etch rate at 180 °C. Therefore, a two stage etch was required where the GaAs is etched at lower temperature (25 °C) and the AlGaInP layers are etched at 180 °C.

With the two-stage etch there is still aspect-ratio dependent etching of AlGaInP when etching is limited by transport of neutral species to the surface and the effect is not observed when removal of the etch product is rate limiting. As the Ar fraction is increased (above ~80 %) and the amount of available neutral reactive species is depleted the ARDE effect becomes more pronounced.

With an optimized set of etch parameters, etching of high-aspect-ratio, sub-micron features in AlGaInP/GaAs laser structures has been demonstrated. Despite the difference in etch mechanisms of GaAs and AlGaInP and the use of a 2-step process, at the same Ar fraction vertical sidewall features were achieved not only on relatively wide ridges but also in sub-micron gratings. Using this process a range of 1-D arrays were etched with lattice constants as short as 200 nm and aspect ratios as high as 20:1.

To the best of my knowledge these are the deepest vertically etched structures on this scale in AlGaInP.

Using this process, laser cavities defined by reflectors formed by plasma etching were fabricated. Devices with cleaved facets, plain etched mirrors and distributed Bragg reflectors were fabricated and the electrical behaviour threshold characteristics of the devices compared.

The I-V characteristics of all the etched devices were identical to that of cleaved devices which is consistent with there being no catastrophic adverse effect of the etching on the p-n junction. However, the increased roughness of the etched facet compared to a cleaved facet causes an increase in threshold current for plain etched cavities. To overcome this increase in threshold current the mirror reflectance was increased by etching distributed Bragg reflectors at each end of a laser cavity. These structures were designed to have a stop-band centred on the lasing wavelength and gave rise to reduced threshold current and increased differential efficiency. Devices were also fabricated with 850 nm DBRs which have a much lower reflectance (than a straightforward semiconductor-air interface) at the lasing wavelength. As would be expected, performance of the device was much worse than both the 1065 nm DBR device, as well as the plain mirror device, with the device not reaching threshold over the drive current range measured.

Finally, the etch process was used to isolate separate devices on the same sample in order to be able to contact the devices independently. The chip was able to emit and detect light on the same chip. This kind of device could potentially be used as integrated sensors for biophotonic applications.

7.2. Future Work

The main purpose of this work was to develop the technology to enable high quality plasma etching of AlGaInP/GaAs laser structures. As part of that development I have made several optoelectronic devices to prove the quality of the etching rather than develop or demonstrate an understanding of the device physics. Now with the capability to etch a wide variety of structures ranging from very large ridges and mesas through to very small gratings with the nanometer scale periods suitable for photonic control there is vast scope for exploitation.

Laser and LED devices with enhanced functionality, reduced size, lower threshold, high power and frequency and spatial control of the light are all possible avenues that may be explored. Integrated devices for optical sensing are also a possible route for further development and understanding.

Finally, one aspect of this work which I began working on but have yet to complete is the development of a technique utilising a segmented contact device to assess the reflection properties of deep-etched gratings. Details of the proposed technique are included in Appendix II.

8. Appendix I – The Transmission Matrix Method

The method described here is for the case of optical waves propagating in thin dielectric films – semiconductor and air. The layers are assumed to be homogeneous and isotropic and the refractive index varies periodically in the z-direction only. The layers are assumed to have infinite extent in the other dimensions. The notation used is taken from reference 82.

Figure 8.1 depicts a multiple layer thin film stack containing S interfaces and therefore S-1 layers. The j^{th} layer has a refractive index n_j and thickness d_j. The j^{th} layer contains a wave travelling to the right with electric field E_j^+ and a wave travelling to the left with electric field E_j^-. The waves are at an angle θ_j to the normal. We define the total electric field at the j/(j-1) interface to be

$$E_j = E_j^+ + E_j^-$$

Equation 8.1

And similarly for the magnetic field

$$H_j = H_j^+ + H_j^-$$

Equation 8.2

For the laser mirrors being modelled, film 0 represents air outside of the device structure. Film S represents the incident medium (the laser cavity) and films 1 to S-1 represent the elements of the DBR. These are all depicted in Figure 8.1.

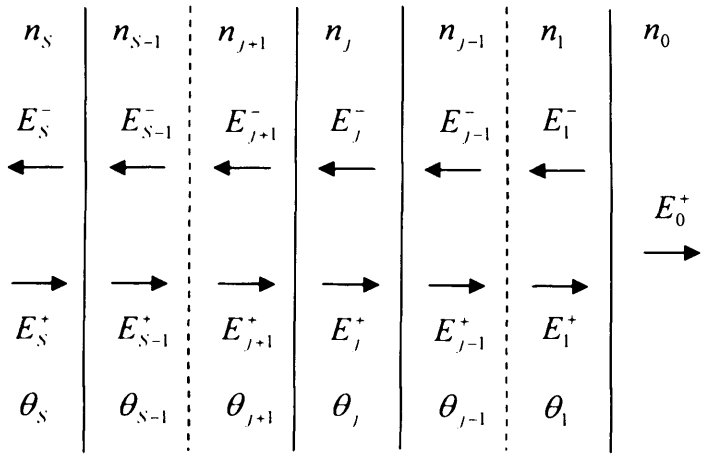

Figure 8.1 – Schematic illustration of a multiple layer dielectric stack. Incident and reflected beams are assumed to be normal. Incident waves are shown travelling from left to right and are given positive superscripts. Reflected waves are shown travelling from right to left and are given negative superscripts.

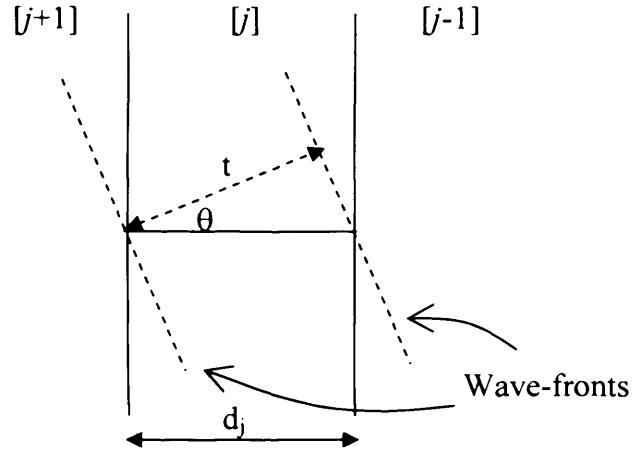

Figure 8.2 – Schematic illustration of the optical path of light travelling through the stack showing the distance between wave-fronts, t.

Waves crossing from layer j to layer (j-1) undergo a phase shift, δ. The optical path length in layer j is given by the distance between the dashed wave-fronts shown in Figure 8.2 (being of equal phase) multiplied by n_j. The optical path length is therefore given by

$$n_j x = n_j d_j \cos\theta_j$$

Equation 8.3

And the phase thickness is given by

$$\delta_j = k n_j d_j \cos\theta_j$$

Equation 8.4

However, for the purposes of this model it is adequate to assume that all waves are propagating normal to the interfaces. Consequently the phase thickness is simply given by

$$\delta_j = kn_j d_j$$

Equation 8.5

The boundary conditions are that the components of E and H parallel to the interface must be continuous across the interface. The convention that the phases of the waves in the j^{th} layer are zero at the interface with layer (j-1) is used. Therefore at the (j+1)/j interface the electric field is given by

$$E_{j+1} = E_{j+1}^{+} + E_{j+1}^{-} = E_j^{+} \exp(i\delta_j) + E_j^{-} \exp(-i\delta_j)$$

Equation 8.6

and the magnetic field is given by

$$H_{j+1} = H_{j+1}^{+} + H_{j+1}^{-} = H_j^{+} \exp(i\delta_j) + H_j^{-} \exp(-i\delta_j).$$

Equation 8.7

Using $H_j^{\pm} = \pm N_j E_j^{\pm}$ we obtain expressions for E_j^{+} and E_j^{-}.

$$E_j^{+} = \frac{1}{2}\left(E_j + \frac{H_j}{N_j}\right)$$

Equation 8.8

$$E_j^{-} = \frac{1}{2}\left(E_j - \frac{H_j}{N_j}\right)$$

Equation 8.9

And similarly for the magnetic fields

$$H_j^{+} = \frac{1}{2}(N_j E_j + H_j)$$

Equation 8.10

$$H_j^{-} = \frac{1}{2}(N_j E_j - H_j)$$

Equation 8.11

Substituting these expressions into Equation 8.6 and Equation 8.7 and rearranging gives

$$E_{j+1} = E_j \cos(\delta_j) + i\frac{H_j}{N_j}\sin(\delta_j)$$

Equation 8.12

$$H_{j+1} = iN_j E_j \sin(\delta_j) + H_j \cos(\delta_j)$$

Equation 8.13

which can be written in matrix form as

$$\begin{bmatrix} E_{j+1} \\ H_{j+1} \end{bmatrix} = \begin{bmatrix} \cos(\delta_j) & (i/N_j)\sin(\delta_j) \\ iN_j \sin(\delta_j) & \cos(\delta_j) \end{bmatrix} \begin{bmatrix} E_j \\ H_j \end{bmatrix}$$

Equation 8.14

or

$$\begin{bmatrix} E_{j+1} \\ H_{j+1} \end{bmatrix} = M_{j+1} \begin{bmatrix} E_j \\ H_j \end{bmatrix}$$

Equation 8.15

where M_{j+1} is the transfer matrix. If the model is extended to 3 layers we get

$$\begin{bmatrix} E_j \\ H_j \end{bmatrix} = M_j \begin{bmatrix} E_{j-1} \\ H_{j-1} \end{bmatrix}$$

Equation 8.16

relating the fields at the boundary between layers j and j-1. Multiplying both sides of Equation 8.16 by M_{j+1} we get

$$M_{j+1} \begin{bmatrix} E_j \\ H_j \end{bmatrix} = M_{j+1} M_j \begin{bmatrix} E_{j-1} \\ H_{j-1} \end{bmatrix} = \begin{bmatrix} E_{j+1} \\ H_{j+1} \end{bmatrix}.$$

Equation 8.17

In fact in a multilayer system the fields in the first and last layers are related by the products of the transfer matrices of the intermediate layer boundaries so that in general

$$\begin{bmatrix} E_S \\ H_S \end{bmatrix} = M_{q-1} M_{q-2} \ldots M_2 M_1 \begin{bmatrix} E_0 \\ H_0 \end{bmatrix}.$$

Equation 8.18

Reflection and transmission coefficients for a single layer are given by the relative intensities of the reflected and transmitted rays to the incident ray.

$$r = \frac{E_S^-}{E_S^+}$$

Equation 8.19

and

$$t = \frac{E_0}{E_S^+}$$

Equation 8.20

We can re-write Equation 8.14 in terms of the boundary conditions and assuming an infinite final layer such that $E_0^- = 0$.

$$\begin{bmatrix} E_S^+ + E_S^- \\ N_S\left(E_S^+ - E_S^-\right) \end{bmatrix} = \begin{bmatrix} m_{11} & m_{12} \\ m_{21} & m_{22} \end{bmatrix} \begin{bmatrix} E_0 \\ E_0 N_0 \end{bmatrix}$$

Equation 8.21

Multiplying out the matrix gives

$$E_S^+ + E_S^- = m_{11}E_0 + m_{12}E_0N_0$$

Equation 8.22

and

$$\left(E_S^+ - E_S^-\right)N_S = m_{21}E_0 + m_{22}E_0N_0$$

Equation 8.23

Dividing both equations by E_S^+ gives

$$1 + r + m_{11}t + m_{12}N_0t$$

Equation 8.24

and

$$1 - r = \frac{m_{21}t + m_{22}N_0t}{N_S}$$

Equation 8.25

Solving these simultaneous equations by addition yields

$$t = \frac{2N_S}{m_{11}N_S + m_{12}N_0N_S + m_{21} + m_{12}N_0}$$

Equation 8.26

Solving by subtraction and substituting t from above yields

$$r = \frac{m_{11}N_S + m_{12}N_0N_S - m_{21} - m_{22}N_0}{m_{11}N_S + m_{12}N_0N_S + m_{21} + m_{22}N_0}$$

Equation 8.27

r and t represent the amplitude reflection and transmission coefficients. The intensity reflection coefficients (reflectance) is given by

$$R = |r|^2$$

Equation 8.28

9. Appendix II - Measuring grating reflectance with a segmented contact device

Several methods have been used to assess the reflectance of deep etched gratings in semiconductor material. Some techniques use laser device measurements to ascertain the reflectance values [22,23]. These measurements will of course only give the value of reflectance at the lasing wavelength. Other techniques involve passing light through waveguides with and without a grating and making a comparison to infer what the transmission properties [83,84,85]. This has inherent difficulties in ensuring the collection of light is the same for the two measurements. In order to avoid some of the alignment/collection difficulties associated with other techniques for measuring in-plane reflectance of photonic microstructures I derived a technique for measuring the reflectance spectrum within one device using light generated from within the waveguide of a laser structure based device. A theoretical description of a technique used to measure reflectance spectra of gratings will be described and the experimental setup to carry out these measurements along with a discussion of the associated challenges will be discussed. The technique described allows the measurement of the reflectance spectra of a photonic structure to be measured using a single device over the same spectral range as the amplified spontaneous emission of that device.

9.1. Theoretical consideration of segmented contact method for measuring grating reflectance

The following is a derivation of a segmented contact method for measuring the reflectance spectra of photonic structures. It is based on the technique used for determining gain and absorption described by Thomson et al. [86]. Consider a device consisting of three identical sections with a grating with transmittance, T, in between the 2^{nd} and 3^{rd} sections. Each of the sections can be pumped independently or in combination. The intensity of light measured with section x, y and z pumped is I_{xyz}.

So we can write expressions for the light intensity as a function of the modal gain, internal scattering loss and cavity length.

First we consider the case where the device is operated in a gain only regime. That is light from rear sections only passes through front sections that are electrically driven.

$$I_1 = \frac{I_{sp}}{(G-\alpha_i)}[\exp(G-\alpha_i)L-1]$$

Equation 9.1

$$I_{12} = \frac{I_{sp}}{(G-\alpha_i)}[\exp(G-\alpha_i)2L-1]$$

Equation 9.2

$$I_{123} = \frac{I_{sp}}{(G-\alpha_i)}[\exp(G-\alpha_i)L-1]T.\exp(G-\alpha_i)2L + \frac{I_{sp}}{(G-\alpha_i)}[\exp(G-\alpha_i)2L-1]$$

Equation 9.3

Where T is the transmittance of the grating; the fraction of light emitted from section 3 in the positive x-axis that passes into section 2.

Rearranging gives

$$T = \frac{I_{123} - \frac{I_{sp}}{(G-\alpha_i)}[\exp(G-\alpha_i)2L-1]}{\frac{I_{sp}}{(G-\alpha_i)}[\exp(G-\alpha_i)L-1][\exp(G-\alpha_i)2L]}$$

Equation 9.4

Since $(G-\alpha_i) = \frac{1}{L}\ln\left(\frac{I_{12}}{I_1}\right)$,

Equation 9.5

$$\exp(G-\alpha_i)L = \left(\frac{I_{12}}{I_1}\right)$$

Equation 9.6

$$\therefore T = \frac{I_{123}-I_{12}}{I_1\left(\frac{I_{12}}{I_1}\right)^2} = \frac{I_1}{I_{12}}\left(\frac{I_{123}}{I_{12}}-1\right)$$

Equation 9.7

or

$$R = 1 - \frac{I_1}{I_{12}}\left(\frac{I_{123}}{I_{12}} - 1\right)$$

Equation 9.8

These values of R rely on the assumption that all light that isn't transmitted is reflected and couples back into the cavity. In reality

$$R = 1 - \left(T + \alpha_{grating}\right)$$

Equation 9.9

Where $\alpha_{grating}$, the total additional optical loss in the grating consists of light absorbed in the semiconductor portions of the grating, light scattered from the etched surfaces and diffraction losses. It is important that the reduction in α_m that a grating provides is not outweighed by the increase in $\alpha_{grating}$.

9.2. Modified segmented-contact device structure

All segmented contact devices described in this thesis were also based on oxide isolated stripe geometry with a stripe width of 50 μm and the length of each section fixed at 300 μm. Figure 9.1 shows the basic device configuration which is based on the device structure described by Thomson et al. [86] for single-pass measurements of modal gain and loss and which has been expanded upon by Lewis et al. [87] and Blood et al. [88]. It is fabricated in a similar way to the oxide isolated stripe lasers with some additional steps to break the metal electrical contact and the underlying GaAs cap layer (which is highly conducting) in segments of equal length.

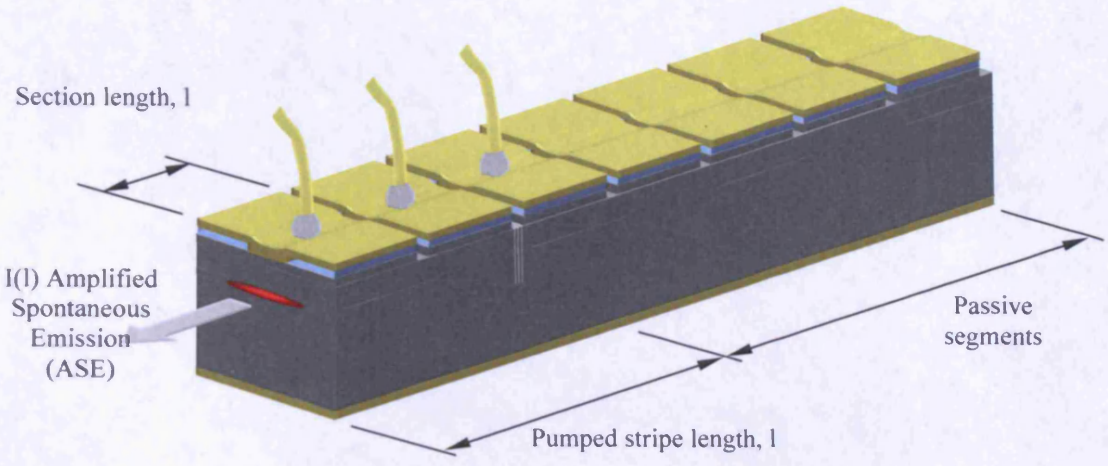

Figure 9.1 – Schematic illustration of the segmented contact device used to measure grating reflectance

The technique, described in Section 9.1 requires 3 sections that can be driven independently or together with the grating to be studied situated between sections 2 and 3. The single-pass amplified spontaneous emission (ASE) is measured using the device to obtain reflectance spectrum of the grating. However, there are several other theoretical requirements that affect the device design. The theory is only valid if there is no round-trip amplification; otherwise it is unfair to make comparisons between sections as the light emitted has been amplified along different lengths of the gain medium. To ensure a single pass, the wafer is processed off the (100) direction and processed such that the stripe is perpendicular to a cleaved facet that is 10° off vertical. This will significantly reduce the amount of light coupled back into the waveguide to participate in amplification.

In a standard segmented contact device it is common to include a long absorbing section at the rear of the device to prevent round trip amplification. However, inserting a reflector between sections 2 and 3 prevents much of the rearward travelling light emitted in sections 1 and 2 from reaching the absorber. Consequently, the 10° off facet is relied upon solely to reduce round trip gain in sections 1 and 2. An absorber section is still included at the rear of the device to absorb light emitted rearward from section 3.

The inter-contact resistance has to be sufficiently high that lateral movement of charge carriers (between sections) is much smaller than the thickness of the cap and upper waveguide epitaxial layers. This is to ensure that electrical pumping is confined to the

desired section and the section lengths are well defined (an important measure when calculating current density).

9.3. Consideration of spectral range

The spectral measurement technique described relies upon light sources that have a spectral range that is less than the stop band expected for typical air-semiconductor Bragg reflectors. To overcome this shortcoming a simple technique is used whereby a range of periods are used and the relatively narrow transmission spectra are plotted as a function of $u=a/\lambda$. This then allows the different spectra to be 'stitched' together to form a continuous broad-band transmission/reflection spectrum.

10. References

[1] P.M. Smowton and P. Blood, Visible Emitting (AlGa)InP Laser Diodes, in: Manasreh MO(Ed.), Strained-layer Quantum Wells and their Applications, Gordon and Breach, 1997, pp 431-487.

[2] T.M. Squires and S.R. Quake, Microfluidics: Fluid physics at the nanoliter scale, Review of Modern Physics, 77, pp977-1026, 2005 .

[3] C. Hansen, K. Leung and P. Mousavi, Chipping in to microfluidics, Physics World, 20 (9), pp24-29, 2007.

[4] A.Y. Fu, C. Spence, A. Scherer, F.H. Arnold and S.R. Quake, A microfabricated fluorescence-activated cell sorter, Nature Biotechnology, 17, pp 1109-1111, 1999.

[5] A. Wolff, I. R. Perch-Nielsen, U. D. Larsen, P. Friis, G. Goranovic, C. R. Poulsen, J. P. Kutter and P. Telleman, Integrating advanced functionality in a microfabricated high-throughput fluorescent-activated cell sorter, Lab on a Chip, 3, pp 22-27, 2003.

[6] Ph. Lalanne and H. Bensity, Out-of-plane losses of two-dimensional photonic crystals waveguides: Electromagnetic analysis, Journal of Applied Physics, 89(2), p1512, 2001.

[7] L.A. Coldren and S.W. Corzine, Diode Lasers and Photonic Integrated Circuits, Wiley Series in Microwave and Optical Engineering

[8] D. Sands, Diode Lasers, Institute of Physics Publishing, Bristol, 2005.

[9] Casey and PanishHeterostructure Lasers Part A: Fundamental Principles, Academic Press, 1978.

[10] Agrawal and Dutta, Semiconductor Lasers, Springer, 1993.

[11] P. Blood, Heterostructures in semiconductor lasers, Chapter 7 in Physics and technology of Heterojunction devices, Edited by D.V. Morgan and R.H.Williams, Peter Perigrinas, 1991.

[12] E. Yablonovitch, Inhibited Spontaneous Emission in Solid-State Physics and Electronics Physical Review Letters, 58, 2059 (1987)

[13] J.D. Joannopoulos, R.D. Meade and J.N. Winn, Photonic Crystals, Molding the Flow of Light, Princeton University Press, New Jersey (1995)

[14] T.E. Sale, Vertical Cavity Surface Emitting Lasers, Wiley, 1995.

[15] R. Jambunathan and J. Singh, Design studies for distributed Bragg reflectors for short-cavity edge-emitting lasers, IEEE Journal of Quantum Electronics, 33(7), p1180, 1997.

[16] E. Hecht, Optics, Addison Wesley Longman, 1998.

[17] M.A. Afromowitz, Refractive Index of $Ga_{1-x}Al_xAs$, Solid State Communications, 15(1) p59 1974.

[18] T. Baba, M. Hamasaki, N. Watanabe, P. Kaewplung, A. Matsutani, T. Mukaihara, F. Koyama and K. Iga, A novel short-cavity laser with deep-grating distributed Bragg reflectors, Japanese Journal of Applied Physics, 35 p1390 1996.

[19] S. Thomas III and S.W. Pang, Dry etching of horizontal distributed Bragg reflector mirrors for waveguide lasers, Journal of Vacuum Science and Technology B, 14(6), p.4119, 1996.

[20] Y. Yuan, T. Brock, P. Bhattacharya, C. Caneau and R. Bhat, Edge-emitting lasers with short-period semiconductor/air distributed Bragg reflectors, IEEE Photonics Technology Letters, 9(7), p 881 1997.

[21] E. Höfling, R. Werner, F. Schäfer, J.P. Reithmaier and A. Forchel, Short-cavity edge-emitting lasers with deeply etched distributed Bragg mirrors, Electronics Letters, 35(2), p154, 1999.

[22] E. Höfling, F. Schafer J.P. Reithmaier and A. Forchel, Edge-emitting GaInAs-AlGaAs microlasers, IEEE Photonics Technology Letters, 11(8), p943, 1999.

[23] T.F. Krauss, O. Painter, A. Scherer, J.S. Roberts and R.M. De La Rue, Optical Engineering 37(4) p1143 1998.

[24] L. Raffaele, R.M. De La Rue, J. Roberts and T.F. Krauss, IEEE Photonics Technology Letters, 13(3) p176 2001.

[25] S. Rennon, F. Klopf, J.P. Reithmaier and A. Forchel, 12μm long edge-emitting quantum-dot laser, Electronics Letters, 37(11), p690, 2001.

[26] J. Moosburger, M. Kamp, F. Klopf, J.P. Reithmaier and A. Forchel, Semiconductor lasers with 2-D-photonic crystal mirrors based on a wet-oxidized Al_2O_3-mask, IEEE Photonics Technology Letters, 15(5), p406, 2001.

[27] T.D. Happ, M. Kamp, F. Klopf, J.P. Reithmaier and A. Forchel, Two-dimesional photonic crystal laser mirrors, Semiconductor Science and Technology. 16 p227 2002.

[28] T.D. Happ, M. Kamp, F. Klopf, J.P. Reithmaier and A. Forchel, Bent laser cavity based on 2D photonic crystal waveguide, Electronics Letters, 36(4) p324, 2000.

[29] M. Korn, T. Körfer and A. Forchel, Fabrication and optical characterisation of first order DFB GaInP/AlGaInP laser structures at 639 nm, Electronics Letters, 26(9), p614,1990.

[30] H.-P. Gauggel, C. Geng, H. Schweizer, F. Barth, J. Hommel, R. Winterhoff and F. Scholz, Fabrication and operation of first-order GaInP/AlGaInP DFB lasers at room temperature, Electronics Letters, 31(5), p367, 1995.

[31] H.-P. Gauggel, H. Artmann, C. Geng, F. Scholz and H. Schweizer, Wide-range tenability of GaInP-AlGaInP DFB lasers with superstructure gratings, IEEE Photonics Tehcnolgy Letters, 9(1), p14, 1997.

[32] H.-P. Gauggel, J. Kuhn, C. Jerichow, C. Geng, F. Scholz and H. Schweizer, Low threshold CW operation of GaInP/AlGaInP DFB lasers at 680 nm, Electronics Letters, 33(16), p1385, 1997.

[33] B. Pezeshki, M. Zelinski, H. Zhao and V. Agrawal, 40-mW 650-nm distributed feedback lasers, IEEE Photonics Technology Letters, 10(1), p36, 1998.

[34] M. Hagberg, B. Pezeshki, S. Zou, M. Zelinski and E. Kolev, 90mW 660nm distributed feedback lasers, Electronics Letters, 35(12), p980, 1999.

[35] D.-H. Jang, Y. Kaneko and K. Kishino, Shortest wavelength (607 nm) operations of GaInP/AlInP distributed bragg reflector lasers, Electronics Letters, 28(4), p428, 1992

[36] B. Pezeshki, J.S. Osinski, H. Zhao, A. Mathur and T.L. Koch, GaInP/AlGaInP 670 nm singlemode DBR laser, Electronics Letters, 32(24), p2241, 1996.

[37] H.-P. Gauggel, R. Winterhoff, J. Kuhn, F. Scholz and H. Schweizer, Room temperature operation of singlemode DBR lasers at 635 nm, Electronics Letters, 33(17), p1466, 1997.

[38] A. Chen, S.J. Chua, B. Wang and E.A. Fitzgerald, Fabrication of two-dimensional photonic crystals in AlGaInP/GaInP membranes by inductively coupled plasma etching, unpublished see website:
https://dspace.mit.edu/bitstream/1721.1/29821/1/AMMNS007.pdf
A. Chen, S. J. Chua, C. Xing, W. Ji, X. H. Zhang, J. R. Dong, L. K. Jian, and E.A. Fitzgerald, Two-dimensional AlGaInP/GaInP photonic crystal membrane lasers operating in the visible regime at room temperature, Applied Physics Letters, 90, 2007.

[39] S.C. McNevin, Chemical etching of GaAs and InP by chlorine: The thermodynamically predicted dependence on Cl_2 pressure and temperature, Journal of Vacuum Science and Technology B, 4, p 1216 1986.

[40] M. Vernon, T.R. Hayes and V.M. Donnelly, Intrinsic mechanism of smooth and rough morphology in etching of InP by Cl_2 determined by infrared laser interferometry, Journal of Vacuum Science and Technology A, 10 (6) p3499 1992.

[41] S. Thomas III, K.K. Ko and S.W. Pang, Monitoring InP and GaAs etched in Cl_2/Ar using optical emission spectroscopy and mass spectrometry, Journal of Vacuum Science and Technology A, 13 (3) 894 1995

[42] J. Hong, J.W. Lee, C.J. Santana, C.R. Abernathy, E.S. Lambers, S.J. Pearton, W.S. Hobson and F. Ren, Comparison of dry etching techniques for InGaP, AlInP and AlGaP, Solid-State Electronics, 39 (7) p1109 1996

[43] J. Hong, J.W. Lee, C.J. Santana, C.R. Abernathy, S.J. Pearton, W.S. Hobson and F. Ren, Plasma etching of InGaP, AlInP and AlGaP in BCl_3 environments, Materials Science and Engineering B, 41 p247 1996

[44] J. Hong, J.W. Lee, E.S. Lambers, C.R. Abernathy, C.J. Santana, S.J. Pearton, W.S. Hobson and F. Ren, Dry etching of InGaAlP alloys in Cl_2/Ar high ion density plasmas, Journal of Electronic Materials, 25 (9) p1428 1996

[45] J. Hong, J.W. Lee, C.J. Santana, C.R. Abernathy, S.J. Pearton, W.S. Hobson and F. Ren, Comparison of BCl_3/Ar and BCl_3/N_2 plasma chemistries for dry etching of InGaAlP alloys, Semiconductor Science and Technology, 11 p1218 1996

[46] J. Hong, E.S. Lambers, C.R. Abernathy, S.J. Pearton, R.J. Shul and W.S. Hobson, Inductively coupled plasma etching of InGaP, AlInP and AlGaP in Cl_2 and BCl_3 chemistries, Journal of Electronic Materials, 27 (3) p132 1998

[47] G.J. van Gurp, P. Jacobs, J. Binsma and L. Tiemeijer, InGaAsP/InP lasers with two reactive-ion-etched mirror facets, Japanese Journal of Applied Physics, 28 L1236

[48] C. Constantine, C. Barratt, S.J. Pearton, F. Ren and J.R. Lothian, Smooth, low-bias plasma etching of InP in microwave $Cl_2/CH_4/H_2$ mixtures, Applied Physics Letters, 61 p2899 1992

[49] D. L. Flamm and G. K. Herb, "Plasma Etching Technology – An Overview" in Plasma Etching, D.M. Manos and D.L. Flamm, ed., p14, Academic Press, San Diego, 1989

[50] D. L. Flamm and G. K. Herb, "Plasma Etching Technology – An Overview" in Plasma Etching, D.M. Manos and D.L. Flamm, ed., p28, Academic Press, San Diego, 1989

[51] R.H. Bruce, Anisotropy Control in Dry Etching, Solid State Technology, pp64-68, 1981

[52] J.W. Coburn and H.F. Winters, Plasma etching – A discussion of Mechanisms, Journal of Vacuum Science and Technology, 16(2), p391, 1979

[53] C.J. Mogab, "Dry Etching" in VLSI Technology, S.M. Sze, ed., pp303-345, McGraw Hill, New York, 1983

[54] J.L. Vossen, The preparation of substrates for film deposition using glow discharge techniques, Journal of Physics E: Scientific Instrumentation, 12, pp159-167, 1979

[55] K.P. Giapis, G.R. Scheller, R.A. Gottscho, W.S. Hobson and Y.H. Lee, Microscopic and macroscopic uniformity control in plasma etching, Applied Physics Letters, 57, p983, 1990

[56] R.A. Gottscho, C.W. Jurgensen and D.J. Vitkavage, Microscopic uniformity in plasma etching, Journal of Vacuum Science and Technology B, 10(5) p2133 1992

[57] D. Chin, S.H. Dhong and G.J. Long, Structural effects on a submicron trench process, Journal of the Electrochemical Society, 132, p1705, 1986

[58] H.C. Jones, R. Bennett and J. Singh, Size dependant etching of small shapes, Proceedings 8th Symposium on Plasma Processing, 90-2, p45, 1990

[59] C. Hedlund, H.-O. Blom and S. Berg, Microloading effect in reactive ion etching, Journal of Vacuum Science and Technology A, 12(4) p1962 1994

[60] C.J. Mogab, The loading effect in plasma etching, Journal of the Electrochemical Society, 124, p1262 1977

[61] M.A. Lieberman and A.J. Lichtenberg, Principles of Plasma Discharges and Materials Processing, p19, Wiley-Interscience, New York, 1994

[62] G. Franz, High-rate etching of GaAs using chlorine atmospheres doped with a Lewis acid, Journal of Vacuum Science and Technology A, 16(3) p1542 1998

[63] G. Franz, Sidewall passivation of GaAs in BCl_3-containing atmospheres, W. Hösler and R. Treichler, Journal of Vacuum Science and Technology B, 19(2) p415 2000

[64] D.W. Hess, Plasma etching of aluminium, Solid State Technology, 24(4), 189 1981

[65] K. Tokunaga and D.W. Hess, Aluminum etching in carbon tetrachloride plasmas, Journal of the Electrochemical Society, 127, p928 1980

[66] K. Tokunaga, F.C. Redecker, D.A. Danner and D.W. Hess, Comparison of aluminium etch rates in carbon tetrachloride and boron trichloride plasmas, Journal of the Electrochemical Society, 128 p851 1981

[67] G.W.C. Kaye and T.H. Laby, Tables of Physical and Chemical Constants, p62, Longman, New York (1985)

[68] T.R. Hayes, P.A. Heimann, V.M. Donnelly and K.E. Strege, Maskless laser interferometric monitoring of InP/InGaAsP heterostructure reactive ion etching, Applied Physics Letters, 57(26) p2817 1990

[69] D.L. Flamm and G.K. Herb, "Plasma Etching Technology – An Overview" in Plasma Etching, D.M. Manos and D.L. Flamm, ed., p80, Academic Press, San Diego (1989)

[70] Epitaxial Products International Ltd., Fabrication report for wafer EPIQ9500287 #F3.

[71] Operating Manual, Oxford Instruments Plasma Technology Plasmalab System 100 with ICP 380

[72] R.J. Shul, G.B. McClellan, R.D. Briggs, D.J. Rieger, S.J. Pearton, C.R. Abernathy, J.W. Lee, C. Constantine and C. Barratt, High-density plasma etching of compound semiconductors, Journal of Vacuum Science and Technology A, 15(3), 1997, pp633-637

[73] Y.H. Lee, H.S. Kim, G.Y. Yeom, J.W. Lee, M.C. Yoo and T.I. Kim, Etch characteristics of GaN using inductively coupled Cl_2/Ar and Cl_2/BCl_3 plasmas, Journal of Vacuum Science and Technology A, 16(3), 1998, pp1478-1482

[74] K. Remeashan, S.J. Chua, A. Ramam, S. Prakash and W. Liu, Inductively coupled plasma etching of GaN using BCl_3/Cl_2 shemistry and photoluminescence studies of the etched samples, Semiconductor Science and Technology, 15, 2000, pp386-389

[75] Avary K, Rennon S, Klopf F, Reithmaier JP, Forchel A, Reactive ion etching of deeply etched DBR-structures with reduced air-gaps for highly reflective monolithically integrated laser mirrors, 2001, Microelectroic Engineering, 57-58 pp593-598

[76] EL Hu, RE Howard 1980, Reactive-Ion Etching of GaAs and InP Using CCl2F2/Ar/O2, Applied Physics Letters, 37(11) p1022

[77] Pearton SJ, Chakrabarti UK, Hobson WS, Kinsella AP 1990, Reactive ion etching of GaAs, AlGaAs, and GaSb in Cl [sub 2] and SiCl [sub 4], Journal of Vacuum Science and Technology B 8(4) p607

[78] Coburn J.W. and Winters H.F., Conductance considerations in the reactive ion etching of high aspect ratio features, Applied Physics Letters, 55(26), 1989, pp2730-2732

[79] H.D. Summers, Strained layer $(Al_yGa_{1-y})_xIn_{1-x}P$ quantum well lasers, PhD Thesis, UWCC, 1993

[80] K. Griffiths, Automated laser diode measurement, M.Phil. Thesis, UWCC, 1992

[81] P.L. Gourley and R.K. Naviaux, 'Optical phenotyping of human mitochondria in a biocavity laser', IEEE J. Quantum Electron., vol. 11, pp 818-826 (2005)

[82] Course Notes, Course D: Thin Film Optics, Applied Optics Summer School, Imperial College of Science, Technology and Medicine

[83] T.F. Krauss and R.M. De La Rue, Optical Characterization of waveguide based photonic microstructures, Applied Physics Letters, 68(12), p1613, 1996.

[84] T.F. Krauss, B. Vögele, C.R. Stanley, R.M. De La Rue, Waveguide microcavity based on photonic microstructures, IEEE Photonics Technology Letters, 9(2)m p176, 1997.

[85] D. Labilloy, H. Bensity, C. Weisbuch, T.F. Krauss, R.M. Del La Rue, V. Bardinal, R. Houdré, U. Oesterle, D. Cassagne and C. Jouanin, Quantitative measurement of transmission, relfection and diffraction of two-dimensional photonic band gap structures at near-infrared wavelengths, Physical Review Letters, 79 (21) 1997.

[86] J.D. Thomson, H.D. Summers, P.J. Hulyer, P.M. Smowton and P. Blood, Determination of Single-Pass Optical Gain and Internal Loss Using a Multisection Device, Applied Physics Letters, 75, p.2527, 1999

[87] G.M. Lewis, P.M. Smowton, J.D. Thomson, H.D. Summers and P. Blood, Measurement of true spontaneous emission spectra from the facet of diode laser structures, Applied Physics Letters, 2002 80(1) pp.1-3

[88] P. Blood, G. M. Lewis, P. M. Smowton, H.D. Summers, J.D. Thomson and J. Lutti, Characterisation of Semiconductor Laser gain Media by the Segmented Contact Method, IEEE Journal of Selected Topics in Quantum Electronics, 2003, Vol.9, No.5, pp.1275-1282